CHARACTERIZATION OF ALGORITHMS AND PERFORMANCE OF A FINE-RESOLUTION ACTIVE INTERROGATION SYSTEM

A Dissertation
Presented to
The Academic Faculty

By

Luke J. Maloney

In Partial Fulfillment
of the Requirements for the Degree
Doctor of Philosophy in the
School of Mechanical Engineering
Department of Nuclear and Radiological Engineering and Medical Physics

Georgia Institute of Technology

August 2020

CHARACTERIZATION OF ALGORITHMS AND PERFORMANCE OF A FINE-RESOLUTION ACTIVE INTERROGATION SYSTEM

Thesis committee:

Dr. Anna Erickson, Advisor
Nuclear and Radiological Engineering and Medical Physics
Georgia Institute of Technology

Dr. C-K Chris Wang
Nuclear and Radiological Engineering and Medical Physics
Georgia Institute of Technology

Dr. Nolan Hertel
Nuclear and Radiological Engineering and Medical Physics
Georgia Institute of Technology

Dr. Rongxiao Zhang
Department of Medicine
Dartmouth-Hitchcock Medical Center

Dr. Steven Biegalski
Nuclear and Radiological Engineering and Medical Physics
Georgia Institute of Technology

Dr. Paul B. Rose
R&D Staff Scientist
Oak Ridge National Laboratory

Date approved: June 26, 2020

ACKNOWLEDGMENTS

I gratefully acknowledge the contributions of all of the members of my advisory committee, whose dedication to education and mentoring has been invaluable in the preparation of this work, and the members of the Office of Radiological Safety at Georgia Tech, for their help in facilitating experiments. I also acknowledge the willing aid and understanding of Nikolay Pavlov, who is owed a major debt of gratitude.

Special thanks are due to the members of the LANNS detectors group: Joe Harms, Arith Rajapakse, and Wesley Gillis, for their friendship and assistance which was always given without reservation. There are many others who have been there for me in exactly the way I needed them to be, at one time or another – they may find their names below:

Jackson Hortenstine	Lana Remniakova	Zachary Fursmidt	Serdar Charyyev
Dashia Wathen	Emily Williams	Steven Kirsch	Sarah Palm
Jake Maloney	Eric Miller	Alex Ruff	Patrick Croce
Jason Ray	Miguel Hinojosa	Austin Winner	Dustin Ballentine
Kevin Adams	Jackie Ellison	Gregory Szalkowski	Meredith Coyle
Mike Maloney	Brad Mannone	John Stooksbury	Tallulah Maloney
Nick Whitworth	Morgan Winn	Andrew Johnson	

This work was supported by the United States Department of Homeland Security, under grant award numbers 2014-DN-077-ARI079-02 and 2015-DN-077-ARI096. Any views and conclusions contained herein are those of the author, and do not necessarily represent the official policies, express or implied, of the United States Department of Homeland Security.

TABLE OF CONTENTS

LIST OF TABLES

LIST OF FIGURES

LIST OF ACRONYMS

ADC analog-to-digital converter

AmBe americium-beryllium

ANSI American National Standards Institute

ASIC application-specific integrated circuit

AWG American wire gauge

BGO bismuth germanate

CCD charge-coupled device

CoMPASS CAEN Multi-PArameter Spectroscopy Software

DAQ data acquisition

DCR dark count rate

FEU forty-foot equivalent unit

FOV field of view

FWHM full width at half-maximum

G-M Geiger-Müller

LDPE low-density polyethylene

LYSO lutetium-yttrium oxyorthosilicate

MU monitor unit

NaI(Tl) thallium-doped sodium iodide

NII non-intrusive inspection

NIM nuclear instrumentation module

NIST National Institute of Standards and Technology

PCB printed circuit board

PDE photon detection efficiency

PMT photomultiplier tube

PTFE polytetrafluoroethylene

RMSE root mean square error

SID source-to-imager distance

SiPM silicon photomultiplier

SNM special nuclear material

SNR signal-to-noise ratio

SOD source-to-object distance

SPAD single-photon avalanche diode

TEU twenty-foot equivalent unit

UV ultraviolet

SUMMARY

Dense scintillators are typically used in cargo radiography applications, due to their high efficiency for detecting gamma and x-rays. In this work, measurements validating a modeled system implementing quartz Cerenkov radiators and LYSO scintillator crystals are presented and discussed. The system implements silicon photomultipliers for light collection and has a uniquely engineered design which minimizes crosstalk between imaging elements. These design parameters necessitate an approach to image reconstruction algorithm design incorporating the geometric parameters, radiation energy information, raw count intensity, and object staging available from the system. Image metrics including spatial resolution and signal-to-noise ratio are discussed, and image-domain postprocessing is used as a knowledge-based technique for data regularization.

CHAPTER 1
INTRODUCTION AND BACKGROUND

Cargo containers are used to transport a significant portion of the world's goods – in 2012 there were as many as 20.5 million intermodal cargo containers in use around the world [1]. The United States, which consistently imports more cargo than any other country [2], has recognized as a national security risk the amount of cargo transiting across its own borders, particularly when considering the risk of special nuclear material (SNM) being acquired and transported by malicious state or independent actors. A standing law enacted in 2007 requires that all maritime cargo entering the US be scanned by "nonintrusive imaging and radiation detection equipment," [3] as opening each container to verify manifests is impractical for safety, throughput, and logistical reasons. As such, non-intrusive inspection (NII) methods include a wide variety of inspection modalities.

Amounts of cargo are usually discussed in terms of twenty-foot equivalent units (TEUs), that is, the amount of cargo equivalent to that which could be shipped in twenty-foot long intermodal containers. This is not an exact unit, as height of containers varies, as does loading, and a forty-foot equivalent unit (FEU) may not be precisely two TEUs [4]. Ports in the United States handled over 33 million TEUs of cargo in 2018 [5], up by 27% from 2011. Figure 1.1 shows the amount of containerized cargo exported by several countries, in TEUs - the United States imports more container cargo than any other country, and ranks second in exports by volume.

1.1 Cargo Interrogation for Threat Detection

The two basic categories of NII methods are active interrogation and passive scanning. Passive cargo scanning techniques employ radiation detectors and associated computational techniques in order to categorize and classify emissions from containers. Radiation portal

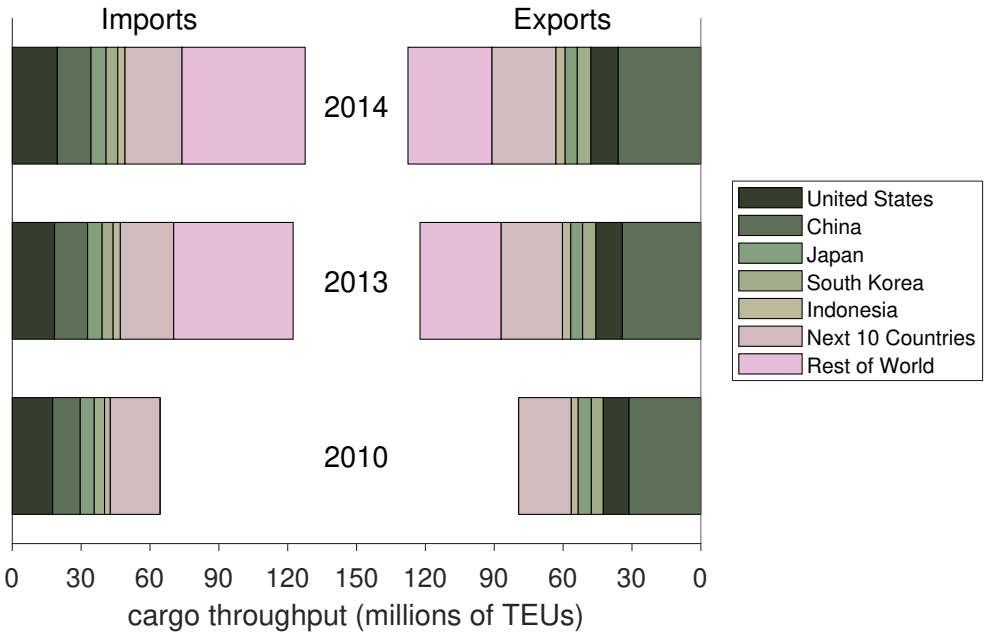

Figure 1.1: Imports and exports of containerized cargo in 2010, 2013, and 2014. Data is shown for 15 largest exporters and the remainder of the world, where available. Data from [2].

monitors at cargo ship and railyards are passive scanners which in short scans check for the presence of radioactive emissions. More sophisticated techniques may give spatial or imaging information about the distribution of radiation in the interrogated object. In passive scans, it is typically implicitly assumed that the particle to be detected originates in the container, so passive methods are well-suited to confirming presence or non-presence of radioactive sources, with a few caveats. Specifically, the signal-to-noise ratio (SNR) must be high enough to confidently indicate detection of a source, which implies a need for at least one of a high-activity source or a detector sufficiently sensitive to low activity – the first is beyond the control of the interrogator. The latter implies cost issues, geometric concerns (to mitigate inverse-square falloff of source strength), and technical challenges (for instance, what are the limits of sensitivity of a given detector material?). Consequently, shielded sources, wherein the particles to be detected are absorbed before they can be counted, represent a major roadblock to confidence in application of passive techniques. There exist methods for increasing the sensitivity and detection power of passive scanning systems,

such as coded aperture imaging techniques [6] and cosmic muon interrogation [7], but the bulk of this work will focus on active modes of interrogation.

Active interrogation techniques use external radiation sources, which bombard the object to be inspected. Typically, the interrogating particles will be either neutrons, photons (gamma rays from atomic sources or electronically generated x-rays), or a combination thereof. A distinction can be made between those particles which are detected by such a system which were emitted in, transmitted through, and scattered by the inspected object. Particles emitted from cargo, particularly gamma rays characteristic of specific nuclear states and sufficiently energetic x-rays of characteristic atomic states, can give particular insight to the composition of material in objects which is susceptible to neutron capture. These emissions may have the additional advantage of being anisotropic, implying that their radial distribution can inform material identification. Scattered particles are well-known to lead to a reduction in image quality when a transmission image is created – for the case of transmitted particles, active interrogation may take the form of radiography, wherein photons or neutrons are employed as the interrogating particle, and a transmission image is formed by the detector in a manner similar to that employed in medical x-ray imaging. In particular, dense and high-Z materials are effective absorbers of photons, In order to ensure that the system is inexpensive, a linear detector array may be used, and the cargo scanned as it transits across the field of view (FOV) of the system. A scanning-geometry active interrogation system is shown in Figure 1.2.

The widespread adoption of active cargo interrogation systems has been stymied by several factors. First, there is a limit on the amount of radiation dose that can be delivered in a single container scan, as high amounts of dose carry both adverse deterministic and stochastic effects. Second, cargo throughput is a major fiscal and economic concern. The Congressional Budget Office estimated that the goal of 100% scanning and imaging would cost up to $22 billion (in 2015) over the course of 10 years, using new procedures and if containers were scanned overseas, and the per-container cost might be as high as $220 [8].

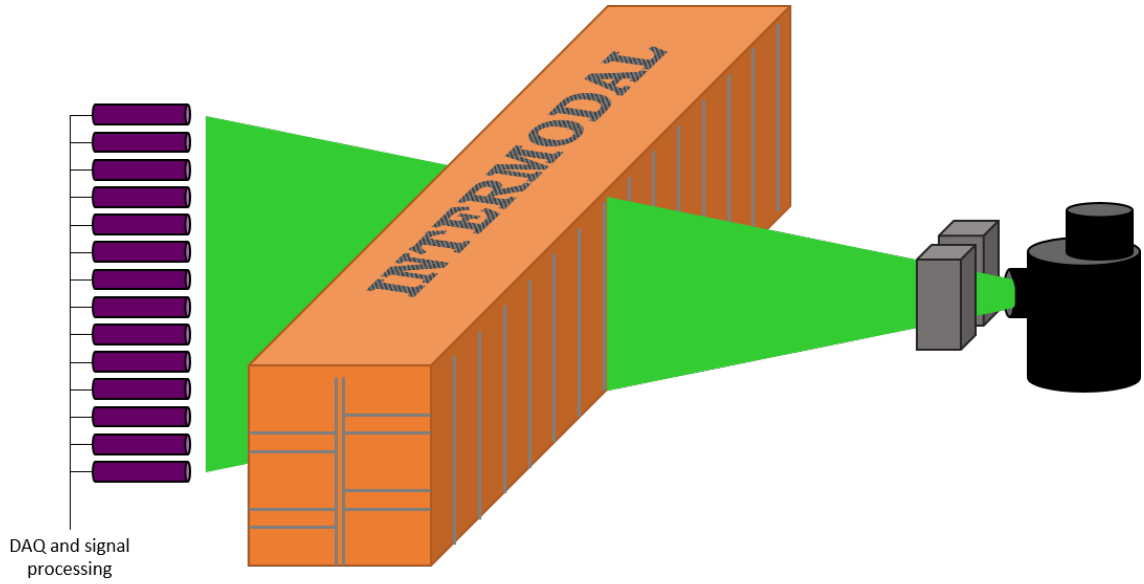

Figure 1.2: Scanning-geometry active interrogation system. Source of interrogating particles (i.e. γ, neutron) is shown in black, and interrogating beam in green.

Contributing to these costs are training operators and upkeep of systems, but the interrogation systems themselves are very expensive, and reducing the up-front investment would have significant impact on the estimated monetary burden.

The vast majority of currently implemented active interrogation radiography systems utilize scintillator detectors in combination with high-energy bremsstrahlung x-ray sources from 4 MeV to 9 MeV endpoints to produce cargo images. In bremsstrahlung generation of x-rays, electrons are accelerated through a high voltage and collide with a high-atomic number metallic target (usually tungsten). As electrons slow down and eventually stop inside the target, their kinetic energy is converted through near-collisions with atomic nuclei to radiated photon energy. Though this is an energy-inefficient method for production of x-rays, as only 0.5% to 5% of electron kinetic energy is directly converted to photon energy – the rest is lost to "soft" collisions which occur far from atomic nuclei – it provides a source which is tuneable in energy. The accelerating potential can be altered, in turn increasing or decreasing the average energy of the x-ray spectrum which is emitted from the target.

In previous work, it has been shown that Cerenkov detectors are a low-cost alterna-

tive to more conventional dense scintillators as a high-energy photon interaction medium which can also be employed for spatial imaging [9]. Further, Cerenkov detectors provide the opportunity for energy calibration (although crude), and thus are applicable in material-discriminating imaging [10]. High-light output scintillators, such as thallium-doped sodium iodide (NaI(Tl)) and bismuth germanate (BGO) are typically used in counting applications when pulse height discrimination is necessary, as the high number of optical photons emitted in the medium leads to higher system energy resolution. An imaging system for active photon interrogation has been designed as part of the MIND collaboration which employs both quartz Cerenkov radiators and lutetium-yttrium oxyorthosilicate (LYSO) scintillation crystals - in this way, the system leverages both low cost and usable energy resolution.

1.2 Objectives and Structure

The motivation of the project forming the bulk of this thesis is the reduction in cost – while maintaining fine spatial resolution and good image quality – of the detection system which might be used in a cargo container radiography application. There are several ways in which this could be accomplished, but this work will focus on a specific system developed at the Georgia Institute of Technology. This system uses LYSO scintillator crystals, which provide an efficient, high-energy resolution means of photon detection, in conjunction with cylindrical quartz elements as Cerenkov radiators, which provide a more inexpensive means of photon detection while simultaneously reducing both inter-detector crosstalk and the burden on system electronics. Light produced by the detector elements is collected by silicon photomultipliers (SiPMs), which are a more modern alternative to the conventional and historical photomultiplier tubes (PMTs). The SiPMs enable fine spatial resolution which is well-suited to detection of small amounts of SNM which might be concealed within cargo.

This work will rely on data collected using a smaller, prototyped version of the proposed

imaging array which has been fabricated specifically for the purposes of testing. Though a very similar system has been analyzed (in Monte Carlo simulation space) for use with both bremsstrahlung, monoenergetic, and low-energy nuclear reaction sources [11], this work will focus on experimental imaging results obtained via bremsstrahlung irradiation, due to availability of sources and the ongoing COVID-19 pandemic.

A significant portion of this work is focused on the design and implementation of the image reconstruction algorithm used with the proposed detector system. Because of the disparate types of detector used in the array, formation of a transmission image involves more computation than would be necessary with an array of uniform detector type. Further, the specific geometric configuration merits additional consideration (discussed in detail later). Performance evaluation of the algorithm will be done in conjunction with performance of the entire system. Standard imaging tests are outlined in ANSI standard N42.46-2008 [12], which will be used to develop metrics for efficacy of the array/algorithm tandem developed.

Due to the energy resolving power of LYSO detectors, material-discriminating imaging is possible with the proposed system. That is, ordinary radiography methods produce only a spatial map of the line integrals of the total attenuation coefficient-path length product. While this is informative to have, it does not necessarily give specific information on the composition of the intervening material – thick objects of low density may appear identical to thin objects of high density, and objects may be superposed with respect to the beamline, occluding those behind. A more robust method for imaging is material-discriminating imaging, i.e. that which produces at least a partial spatial map of the type of material present in the image. With a detector of sufficient energy resolution, this may be readily accomplished by analysis of the absorption profile in varying energy regimes, since attenuation coefficient depends on both Z and E. Thus, an image which informs on "effective Z", or Z_{eff} can be produced.

The specific research questions this work sets out to answer are as follows:

1. What methods and processing techniques in algorithm design maximize image qual-

ity, with respect to sensitivity, noise reduction, and SNR given pixel size? Since material-discriminating imaging is a goal, can it be achieved under conventional bremsstrahlung (rather than low-energy nuclear reaction) irradiation, using energy resolving power available from LYSO scintillators?

2. How well does the system perform on standard tests, specifically the ANSI N42.48-2008 spatial resolution and contrast sensitivity metrics? Can the goal of 5mm spatial resolution be met using the image processing algorithms? What is the per-material uncertainty for material-discriminating images?

3. In comparing cost to performance, what amount of marginal gain or reduction is experienced in using Cerenkov detectors vs alternatives – for example, LYSO? In digitization and associated electronic components on per channel basis? What is the aggregate expected cost of a full-scale system with the proposed characteristics? How does the cost compare to that of existing cadmium tungstate systems?

Answers to these questions will inform an understanding of the proposed system and its capabilities for cargo container radiography, though on a smaller scale. The outline of the dissertation follows – its layout is intended to provide the reader first with an understanding of radiation detectors and photodetectors, as well as relevant performance parameters and characterization of the proposed system, then lead into a discussion of implementation of the system, the associated reconstruction techniques, capabilities, and cost analysis of a full-scale aggregated system.

- Various scintillator detectors and current industry standards are discussed. A physical description is given of the proposed detector array, with relevant performance parameters of individual elements (i.e. crystals, SiPMs, analog-to-digital converter (ADC)). A detailed description of the radiography algorithm for this use case is given and discussed.

- Acquired image datasets are shown, and the effects of corrections applied are analyzed. The ANSI N42.46-2008 image tests are described and results are presented with discussion of quality on various metrics. In particular, spatial resolution and material discrimination accuracy are evaluated, wire detection capability is assessed. Image postprocessing techniques are discussed.

- Cost analysis is presented for the proposed system, and is compared to that of existing systems available on the market. The workings of several types of readout systems are discussed, as well as their advantages and disadvantages. Overall system cost for a full-scale cargo system is estimated, including all fabricated and "off-the-shelf" components.

CHAPTER 2
DETECTION SYSTEM INSTRUMENTATION

The components of any system for noninvasive assay based on radiation-based interrogation methods will invariably consist of three basic components: the source of the radiation, the object itself, and the mode of detection of the radiation. In passive systems, the source is typically assumed to be within the object, and detection of emitted particles informs the user of the contained source, as in positron emission tomography (PET) and radiation contamination monitors. In active systems, the source is external to the object and usually self-contained. Choice of the detector types and readout electronic components for data acquisition (DAQ) is important – the system must be sensitive to the radiation of choice and operate within the parameters dictated by the source and object constraints.

2.1 Radiation Detectors for Active Interrogation

Radiation detectors take a number of forms – perhaps the most recognizable is the Geiger-Müller (G-M) tube, which forms the detection element of the Geiger counter, and the characteristic "tick" it gives when radiation is detected, and which offers little more information than this in the way of characterizing the radiation present. These detectors function by causing incident ionizing radiation to initiate very large electrical pulses called Townsend avalanches, which are generated when liberated electrons are accelerated by a strong electric field in a gas. A single free electron becomes energetic enough to ionize several other atoms, which in turn gain energy in the field, and the effect "snowballs" until a sustained avalanche of electrons reaches the central anode wire in the gas-filled tube, which forms the output pulse. The pulse may become self-sustaining via multiple pulsing if the fill gas of the tube has a sufficiently high ionization energy [13], so Geiger tubes are *quenched*, either internally or externally, via some method which prevents multiple avalanches from

occurring for a single detected particle.

In a G-M counter, there is no proportionality between output pulse height and energy of incident radiation. When energy information is required for some application such as isotope identification, other methods of detection are employed, among the most common being scintillator detectors. Inorganics are particularly useful, because they tend to be dense and have correspondingly high macroscopic cross-sections for interaction and are easy to manufacture. Inorganic scintillators also have low energy resolution – that is, the ratio of the full width at half-maximum (FWHM) to the ordinate of the center of a Gaussian corresponding to a single spectral line is low, corresponding to a "sharper" peak at each line, whereas a spectrometer with poor (i.e. high) energy resolution will produce peaks which are wider with respect to their heights.

Whether organic or inorganic, scintillators used in radiation detection employ the same principle: some ionizing radiation enters the material volume and interacts via a noncoherent method (such as Compton scatter), and the energy absorbed may cause an electron to be promoted to the conduction band of the crystal. Typically the band gap energy is high enough in inorganics that electrons relaxing from this state to the valence band release photons with short wavelengths (ultraviolet or smaller), so impurities are introduced in order to lower the band gap at the dopant sites. Thus, optical photons are released in the de-excitation phenomenon, in numbers proportional to the number of charge carriers in each band, which is in turn proportional to the amount of energy deposited by the incident radiation. Transitively, the amount of optical light is proportional to the energy of the incident radiation, though the number of photons produced is still low even in high light output scintillators.

One of the most popular scintillators, thallium-doped sodium iodide (NaI(Tl)), produces 3.8×10^4 optical photons per MeV of deposited energy with a time constant of $0.250\,\mu s$ on interaction with ionizing radiation [14] – for comparison, $1\,cm^2$ of area in full sunlight is irradiated by roughly $3 \times 10^{11}\,\gamma/\mu s$. Because the number of optical pho-

tons emitted in scintillation events is so low, sensitive application-specific photodetectors are used to amplify these small signals to levels sufficiently high for analysis by readout electronics systems.

Those characteristics which make a scintillator suitable to a specific application vary, but there are several factors which are of concern in most cases:

- Perhaps the most important characteristic is **scintillation efficiency**, or **light yield**. A scintillator with high light yield (typically measured in photons per keV or MeV) converts the kinetic energy of interacting particles efficiently into optical photons. As the number of optical photons produced is a Poisson-distributed variable, the energy resolution of the scintillator is proportional to the square root of the light yield, and the relative error contribution from other factors in the detection system, like electronic/thermal noise, decreases as the light yield increases.

- Cross-section of interaction for the particle(s) of interest must be considered, and correspondingly **material density**, to which cross-section is directly proportional. High density implies more efficient particle detection, driving error on measurement lower during the same data acquisition time.

- **Decay time constant** is of major concern, especially in high-flux environments. Induction of luminescence is not instantaneous, and excited electrons relax to the scintillator valence band with a specified time constant. The signal pulse from an individual interaction event should be sufficiently short that it can be registered by the DAQ system as a separate event from those occurring before and after. If the time constant of light production is large, the "glow" of the scintillator may last long enough that pulse pile-up occurs in the electronics system.

- The **refractive index** of the scintillator should well match the refractive index of the optical photodetector to which it is coupled to minimize loss of photons at the interface.

- For those detectors which must be deployed in rugged environments, **hygroscopicity** is a major concern, as some inorganic materials readily uptake atmospheric water vapor into their structure, damaging scintillators as a result of altering their scintillation properties.

- **Energy linearity** is a desirable, but not absolutely necessary detector characteristic. A material which linearly converts input particle energy into output photon energy over most of its dynamic range is preferred because the uncertainty in the ADC calibration can be very low if this is the case.

A number of commonly used inorganic scintillators are compared on the metrics described above in Table 2.1.

Table 2.1: Performance characteristics of several inorganic scintillators.

scintillator	**light yield** (γ/MeV)	**density** (g/cm^2)	**decay time constant** (ns)	**refractive index**	**hygroscopic**	**ref**
NaI(Tl)	38000	3.67	250	1.85	yes	[14]
LYSO	27 600-33 200	7.1	36-45	1.81	non	[15]
$CdWO_4$	12 000-15 000	7.9	14 000	2.2-2.3	non	[16]
BGO[1]	8000	7.13	300	2.15	non	[17, 18]
GSO[2]	8000-10 000	6.71	30-60	1.85	non	[19, 20]
YAP[3]	18 000-25 000	5.37	25-28	1.95	non	[21, 22]
$LaBr_3$	63000	5.08	16	1.9	yes	[23]

[1]Bismuth germanate ($Bi_4Ge_3O_{12}$), [2]Gadolinium orthosilicate (Gd_2SiO_5:Ce),
[3]Yttrium aluminum perovskite ($YAlO_3$:Ce)

In this work, the inorganic scintillator lutetium-yttrium oxyorthosilicate (LYSO) was selected for use as a photoconverter, due to its high light yield and density, fast light output, and lower refractive index compared with other scintillators. Monolithic crystals were sourced from Scintitech (Shirley, MA, USA) in a 6 mm $\times$ 6 mm $\times$ 50 mm rectangular

prism form factor, in order to match the window size of the light readout devices, which are discussed later.

One of the original goals in the design of the linear imaging array described here was material-discriminating imaging, while maintaining low system cost. While scintillators are well-suited and used extensively in this application space due to their energy-resolving capabilities [24, 25], Cerenkov radiators were investigated as a low-cost alternative to scintillators for light conversion. It has been shown that Cerenkov detectors are suitable in active interrogation, both for spatial imaging [9] and material-discriminating imaging [10], though the system described here has different geometry than those described previously. The quartz rods in this array are 6 mm in diameter and 50 mm in length, and are sourced from Technical Glass Products (Painesville, OH, USA) – their characterization is discussed in detail in chapter 3.

Cerenkov radiation will not occur in the quartz volume unless the speed of a liberated electron exceeds the phase velocity of light in the medium, which in turn depends on the material's index of refraction, n:

$$n = \frac{c}{v},$$

where is c the phase velocity of light in a vacuum and v the phase velocity of light in the medium of interest. From kinematics, we obtain the kinetic energy of a Compton scattered electron [26]:

$$T_e = E_\gamma \left(1 - \frac{1}{1 + \frac{E_\gamma}{m_0 c^2} (1 - \cos\theta)} \right),$$

where T_e is the electron's (relativistic) kinetic energy, E_γ the energy of the incident gamma, m_0 the electron rest mass, and θ is the angle through which the *photon* is scattered.

From relativity, we have

$$T_e = m_0 c^2 \left(\gamma - 1\right)$$

$$\gamma = \frac{1}{\sqrt{1 - \frac{v_e^2}{c^2}}},$$

where v_e is the electron's relativistic velocity. From the above equations, the minimum energy of an electron which generates Cerenkov radiation, T_e^{min}, and the resulting minimum gamma energy to generate Cerenkov radiation via Compton scatter, E_γ^{min}, are uniquely determinable. Taking θ to be $180°$ - that is, for a backscattered photon transferring the maximum energy in a Compton collision:

$$T_e^{min} = m_0 c^2 \left(\frac{1}{\sqrt{1 - \frac{1}{n^2}}} - 1 \right) \tag{2.1}$$

$$E_\gamma^{min} = \frac{1}{2} \left(T_e^{min} + \sqrt{2 \left(T_e^{min}\right) m_0 c^2 + \left(T_e^{min}\right)^2} \right). \tag{2.2}$$

In fused quartz, for which $n = 1.46$ (from [27]), the Cerenkov threshold for Compton interaction is $E_\gamma^{min} = 0.3354\,\mathrm{MeV}$.

It should be noted that the above equations are valid only for the case of photons maximally transferring energy to electrons via Compton interactions – photoelectric interactions also give rise to energetic electrons, but above the photoelectric Cerenkov threshold of quartz ($T_e^{min} = 0.190\,\mathrm{MeV}$) are orders of magnitude less likely than Compton interactions (see Figure 2.1).

The spectral intensity of Cerenkov photons resulting from energetic electrons is given by the well-known Frank-Tamm formula:

$$\frac{d^2 N}{dx\, d\lambda} = \frac{2\pi\alpha}{\lambda^2} \left(1 - \frac{1}{\beta^2 n^2} \right), \tag{2.3}$$

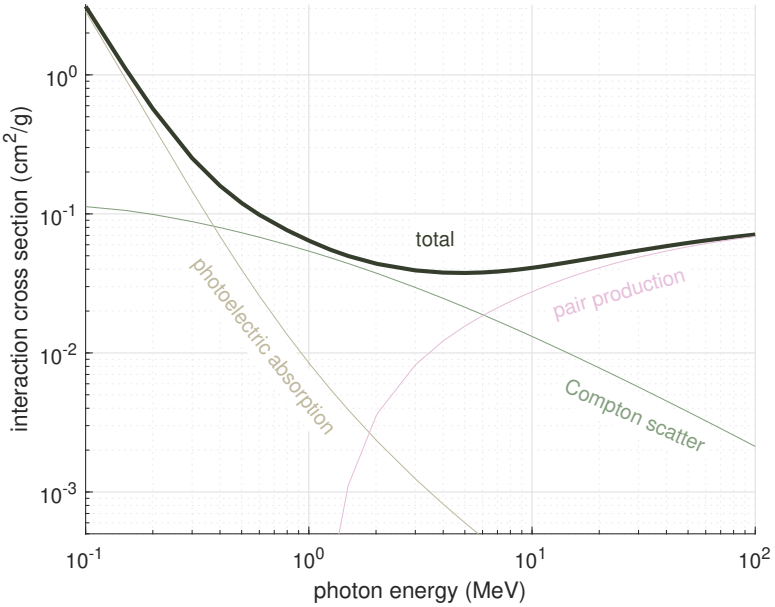

(a) LYSO cross sections.

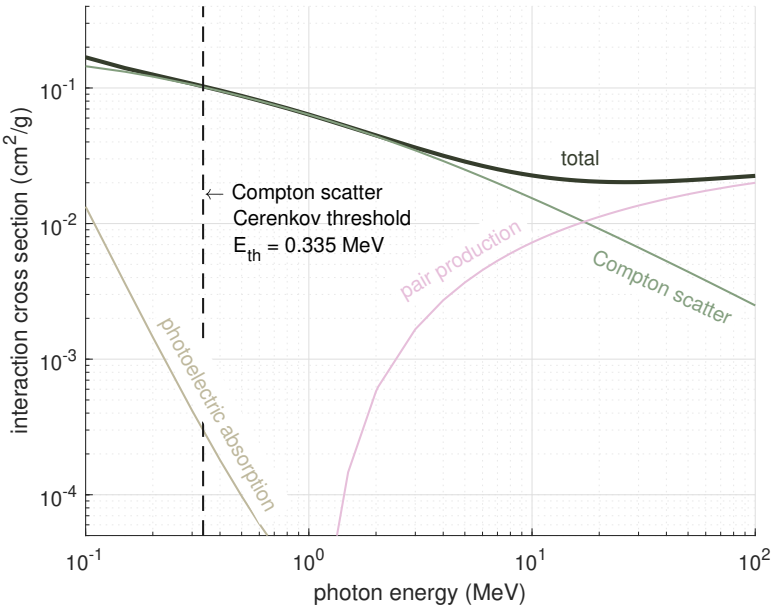

(b) Quartz cross sections.

Figure 2.1: Photon interaction cross sections for materials used in the detector array: quartz and LYSO. Data from [28].

where α is the fine structure constant, n is a function of λ, the photon wavelength, and assuming a medium permeability equivalent to the vacuum permeability of μ_0. This expression is only valid when $v \geq c/n(\lambda)$, that is, when electron velocity exceeds the speed of light in the medium. The dependence on the medium refractive index explains peaking of Cerenkov light spectra in the ultraviolet (UV) regime – $n(\lambda)$ increases sharply at successively shorter wavelengths, such that the n dependence dominates over the λ dependence of Equation 2.3 beyond a point, typically by the microwave energy region.

A plot illustrative of Cerenkov light emission in quartz is given in Figure 2.2 – the strong falloff of light emission for decreasing electron energy is immediately evident.

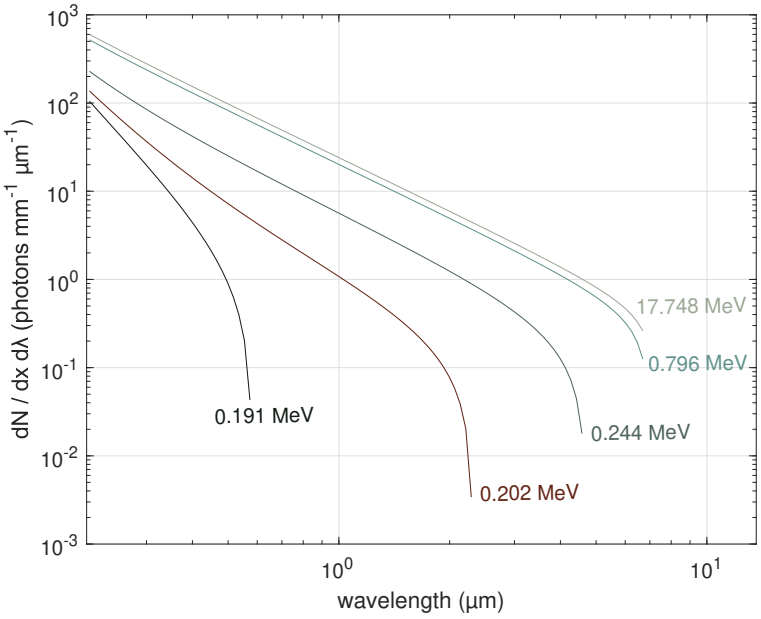

Figure 2.2: Cerenkov spectra in quartz. These curves correspond to electrons in material following backscatters from photons of 0.336 MeV, 0.350 MeV, 0.4 MeV, 1 MeV and 18 MeV. Plot covers wavelength-dependent refractive index range in data from [29, 30].

Further, the characteristically poor energy resolution of Cerenkov detectors can be inferred by integration over all λ in Equation 2.3, which yields the linear light conversion rate. The vast majority of electron energy loss in dense media is due to collisive interactions, not Cerenkov radiation. Thus, the particle traversing the detector will only deposit energy along a path length determined by its range, $\mathfrak{R}_{CSDA}$. By including the mass stop-

ping power $(dT/\rho dx)$ in Equation 2.3 and integrating again, a scintillator-equivalent light output can be determined, for direct comparison. The light yield per unit kinetic energy is thus given by

$$LY\left(T_0\right) = \frac{1}{\rho\, T_0} \int_0^{T_0} \int_\lambda \left(\frac{d^2N}{dx\, d\lambda}\right) \left(\frac{dT}{\rho dx}\right)^{-1} d\lambda\, dT\,, \tag{2.4}$$

where T_0 is the electron kinetic energy at generation. This light yield has a maximum of 260 γ/MeV at 6.66 MeV – the full plot is shown in Figure 2.3.

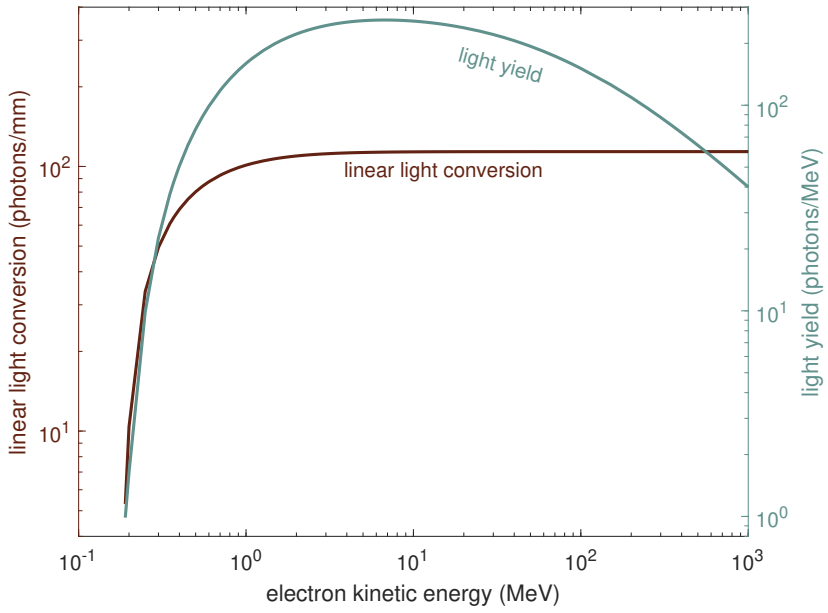

Figure 2.3: Linear light output and total per-MeV light yield in quartz as a function of electron kinetic energy. The peak near 6 MeV-7 MeV is due to the minimum in the stopping power near this region [31]. NIST values for plate glass were used in place of quartz.

Comparing the values in Figure 2.3 to those in Table 2.1, the quartz Cerenkov radiator significantly underperforms even the lowest light yield scintillator by a wide margin. Because there are so few information carriers available to be converted, the associated statistical uncertainty is very high, which readily explains the lack of energy resolution of these detectors. Further, the actual yield may be even lower depending on the geometry of the detector element – electrons can escape from the volume if the path lengths of their trajectories within the detector are less than their ranges, in which case fewer photons than

suggested by Equation 2.4 will be generated.

An additional cause of resolution loss is incomplete light collection, which can be mitigated by choosing a radiator which is transparent to the photons generated within it, and by encapsulating the radiator in material which allows it to approach total internal reflection. Further, the photon detection efficiency (PDE) of the photodetector (e.g. a PMT or SiPM) is nonuniform with respect to wavelength, and indeed likely does not have a peak PDE coincident with maximum light emission intensity. This is especially true in the case of Cerenkov light, which peaks in the ultraviolet. In order to maximize light transport to photodetectors (discussed in section 2.2), each detector element was wrapped in polytetrafluoroethylene (PTFE) tape, and then in aluminum foil.

With the goals of both material discrimination and low cost in mind, the system was designed to use both quartz as a Cerenkov radiator and LYSO as a scintillator, in a 2:1 number ratio. Photos of each detector element type are shown in Figure 2.4. Figure 2.5 shows a conceptual image of the full-size array, for which the system in this work serves as a model.

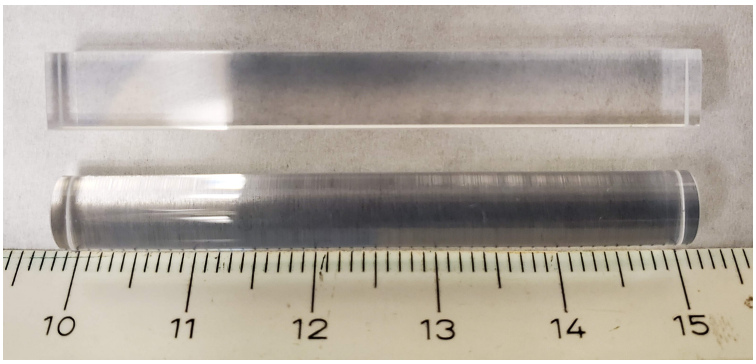

(a) Top: LYSO detector volume element; Bottom: quartz volume element.

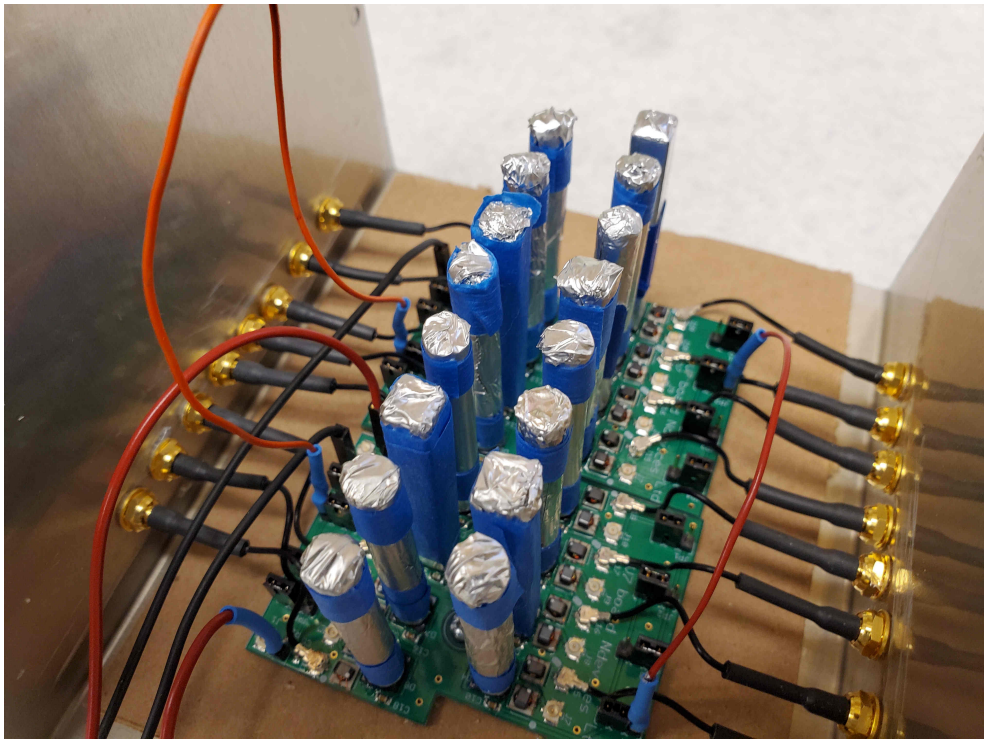

(b) Assembled array, with top of lightproof enclosure removed. Orange and red cables daisy chain the bias voltage between boards. The inner portion of the MCX bulkheads is visible. Detector elements are wrapped in PTFE tape and aluminum foil to maximize internal reflection.

Figure 2.4: Images of detector elements in the array

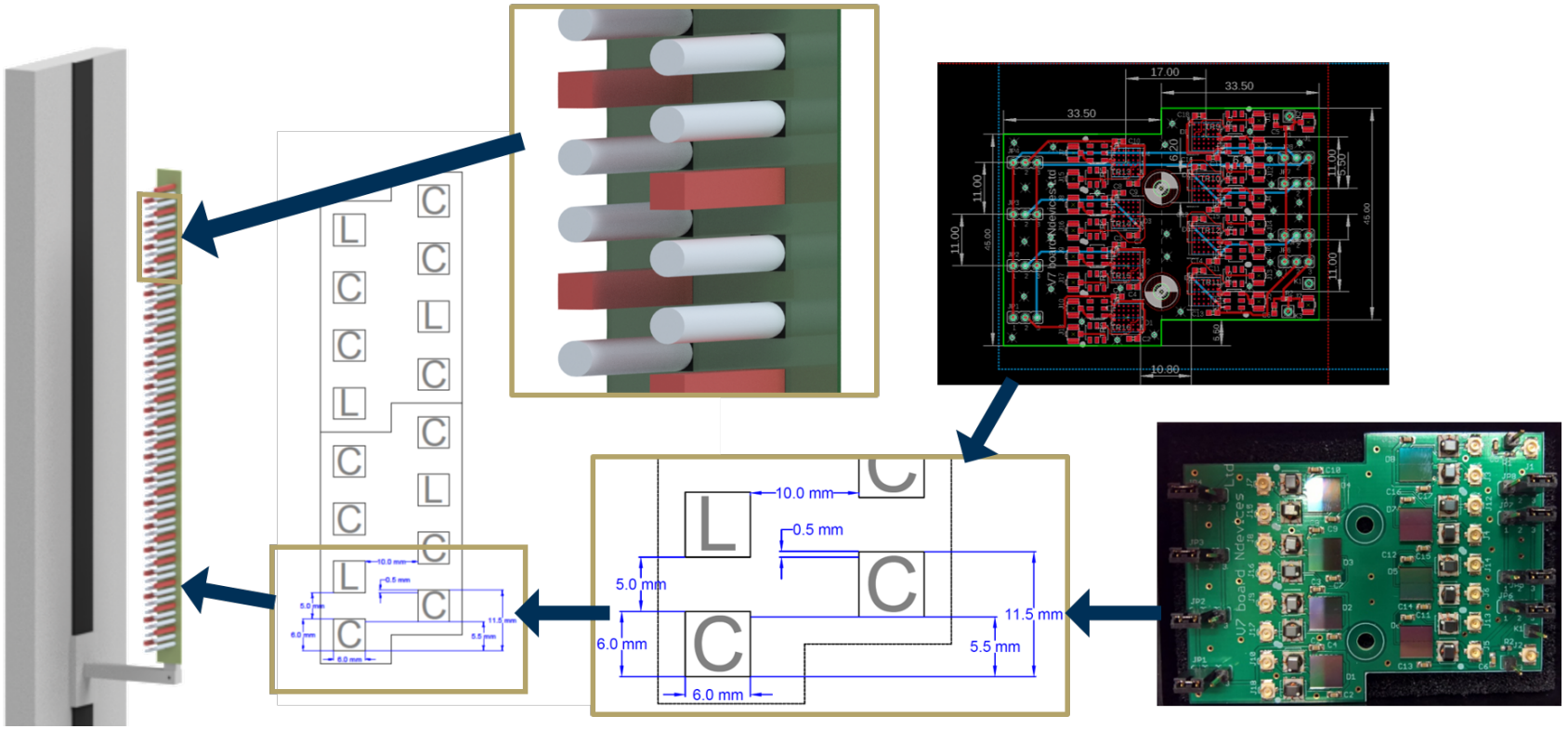

Figure 2.5: From left to right, top to bottom: Digital mockup of entire detector array mounted on motion system; schematic showing locations of LYSO (L) and quartz (C) crystals in frontal view; detail view of LYSO (red) and quartz (white) crystals mounted on backing PCB; detailed schematic showing dimensions of array; single two-layer printed circuit board (PCB) footprint; single PCB with all components mounted (except detector crystals). Digital renderings courtesy of Paul Rose.

Because Cerenkov light is so strongly emitted at low wavelengths, choice of coupling medium between the photodetector and the radiator is important – the medium should be as transparent as achievable to all emitted photons, and with a well-matched index of refraction. For this application, RX-22P optical silicone coupling compound [32] is chosen, as its refractive index of 1.4346 at 425 nm is close to the index of refraction of quartz, and it forms a soft adhesive for securing the quartz elements in place on the SiPM windows.

Transmission of the optical compound was measured using an Ocean Optics QE Pro optical spectrometer. Monochromatic light sources[1] of wavelengths 290 nm, 365 nm, 405 nm and 455 nm were measured independently, and transmission for each was recorded above the intensity threshold shown in Figure 2.6. Cuvettes in use with the spectrometer have 1 cm path length.

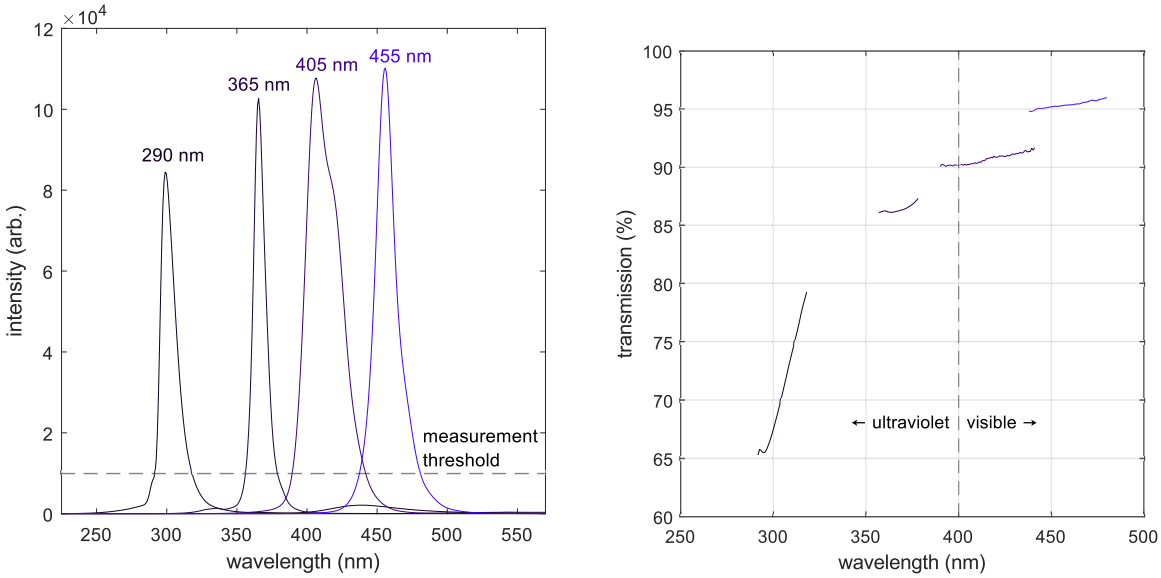

(a) Monochromatic light peaks.

(b) Relative transmission measurements.

Figure 2.6: Optical characterization of coupling medium RX-22P.

[1] A deuterium-halogen lamp was the preferred light source, but it was nonfunctioning and a replacement could not be found in time for this writing.

2.2 Electronics for Data Processing

Historically, PMTs have been the devices used in radiation detection systems for light read-out, because they enable detection systems to be sensitive to single-photon events. PMTs suffer from a number of drawbacks, however. First, they rely on transport of electrons through a vacuum tube, and strong magnetic fields deflect particle trajectories, so the devices are ineffective at signal amplification in magnetic fields. Second, the voltage at each of the dynodes in the vacuum tube must be high in order to successively multiply the electron number, so PMTs require high-voltage power supplies for biasing (600 V to 1500 V). Third, PMTs are challenging to manufacture to a small size, which makes creating array imagers of small spatial resolution difficult without additional engineering – for example, light piping via fiber optic cable from scintillator(s) to a PMT array.

In recent years, an attractive alternative has begun to enter use in the SiPM, which offers a number of advantages over PMTs. SiPMs are based on single-photon avalanche diodes (SPADs), which exploit the high electric field created in a p-n semiconductor junction which is reverse-biased at a voltage above its breakdown voltage to initiate an electron avalanche during single-photon photoelectric events at the junction. Thus, they are also capable of the single-photon sensitivity useful in radiation counting applications – a major difference in operation between them and PMTs is the loss of proportionality between photon energy and output current in a SPAD. By analogy, SiPMs operate in a manner similar to Geiger counters, wherein output pulse height is constant, and must be quenched between events. Output signal intensity is based on photon counting, rather than pulse height of an electrical signal [33, 34].

A significant advantage of SiPMs is that they can be manufactured to very small sizes. While there exist small form factor PMTs, those devices have an active area which is significantly smaller than the package size, and as such are not directly tileable. Further, SiPMs have significantly lower operating voltages than PMTs, on the order of tens of volts for

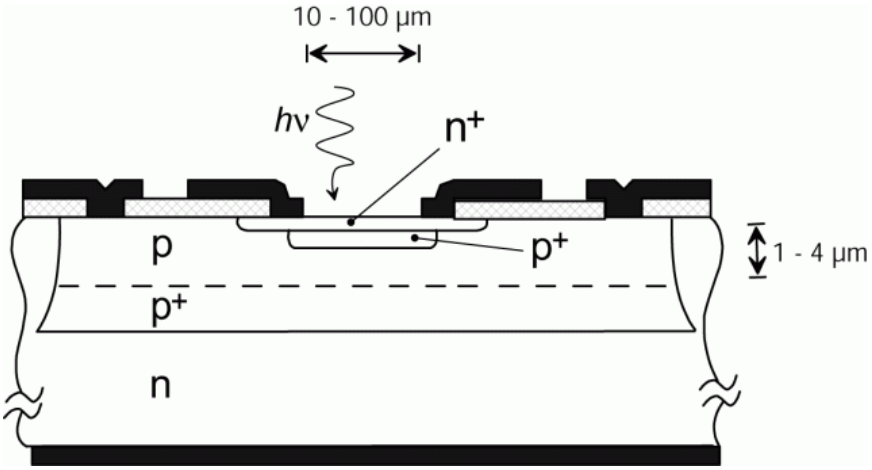

Figure 2.7: Cross-section of a thin-junction SPAD. The depletion layer where electron avalanches are generated is between the device surface and the dotted line.

thin-junction SPADs rather than hundreds or thousands[2]. Uniform performance of SiPMs has been demonstrated in magnetic fields up to 7 T in strength [35].

[2]Thin-junction SPADs have p-n junctions with depletion layers typically of 1 µm, while thick-junction devices may have a depletion layer of 20 µm to 150 µm, and operate at up to 500 V [33].

Table 2.2: Performance characteristics of several silicon photomultipliers (SiPMs).

manufacturer	**model**	**size** (mm)	**operating voltage** (V)	**peak sensitive wavelength** (nm)	**DCR** (kHz/mm^2)	**cover refr. index**	**gain** ($\times 10^6$)	**PDE** (%)	**output capac.** (pF)	**recovery time constant** (ns)	**ref**
ON Semiconductor	MICROFJ-60035	6×6^a	25.2-30.7	420	50	1.53	2.9	38	160 (fast) 4140 (anode)	15	[36]
	MICROFC-30020	3×3^a	25.2-29.7	420	33	1.59	1	24	20 (fast) 770 (anode)	23	[37]
Ketek GmbH	PM1125-WB	1×1	25.5-30.5	430	50	1.52	0.87	31	125	$28 - 33$	[38]
	PM3315-WB	3×3	28-33	430	50	1.52	0.35	22	800	$13 - 47$	[39]
Hamamatsu	S14520-6050VS	6×6^a	41	450	67	1.57	2.8	49	2000		[40]
	S14160-3010PS	3×3^a	43	460	78	1.57	0.18	18	530	b	[41]
	S13360-6025PE	6×6^a	58	450	44	1.55	0.70	25	1280		[42]
	S14420-3025MG	$3\,\varnothing^a$	47	600	57	1.49	0.9	30	350		[43]
First Sensor AG	SiPM-RGB4S	4×4^a	$29 - 33$	550	< 100	1.51	2.7	32.5	840	50	[44]
	SiPM-NUV4S	4×4^a	$30 - 34$	420	< 50	1.51	3.6	43	840	70	[45]

[a] Available in other sizes for different part number.
[b] Values not listed by manufacturer.
Data are from manufacturer specification documents, where available, and as such may be taken under differing test conditions, including temperature and operating voltage. PDE is given at the wavelength of peak sensitivity unless otherwise noted. Some values are estimated – for example, First Sensor provides capacitance values per microcell, so these values were multiplied by the number of microcells to obtain the values in the table.

Silicon photomultiplier (SiPM) devices in the proposed detector system are 6 mm $\times$ 6 mm devices manufactured by the sensL division of ON Semiconductor (Cork, Ireland). The SiPMs' covers are directly optically coupled to the detector elements, either LYSO or quartz. The SiPMs are directly mounted via a ball-grid array surface mount to the PCB on which the remaining components associated with signal readout are mounted. A dual-layer PCB is used, the simplified circuit diagram for which is shown in Figure 2.8.

Because the array includes disparate detector types, it is necessary to be able to select the bias voltage for the SiPM channels individually – this is done by a parallel set of voltage-selecting pin jumpers from the respective bias rail to ground. Bias voltages may be provided by pin connector or by Hirose U.FL surface mount connectors. The bias voltage is high-pass filtered (cutoff frequency = 1.13×10^5 Hz) to minimize the effect of line noise on variation in overvoltage.

Each SiPM has both a fast and slow output, with different pulse shapes. The standard pulse output shape is used in this work. Before readout, each SiPM signal is DC-filtered by a transformer. The readout interface for each channel is a U.FL surface mount connector. The signal is passed from the PCB via coaxial cable to a custom MCX bulkhead, and from the bulkhead to the readout electronics.

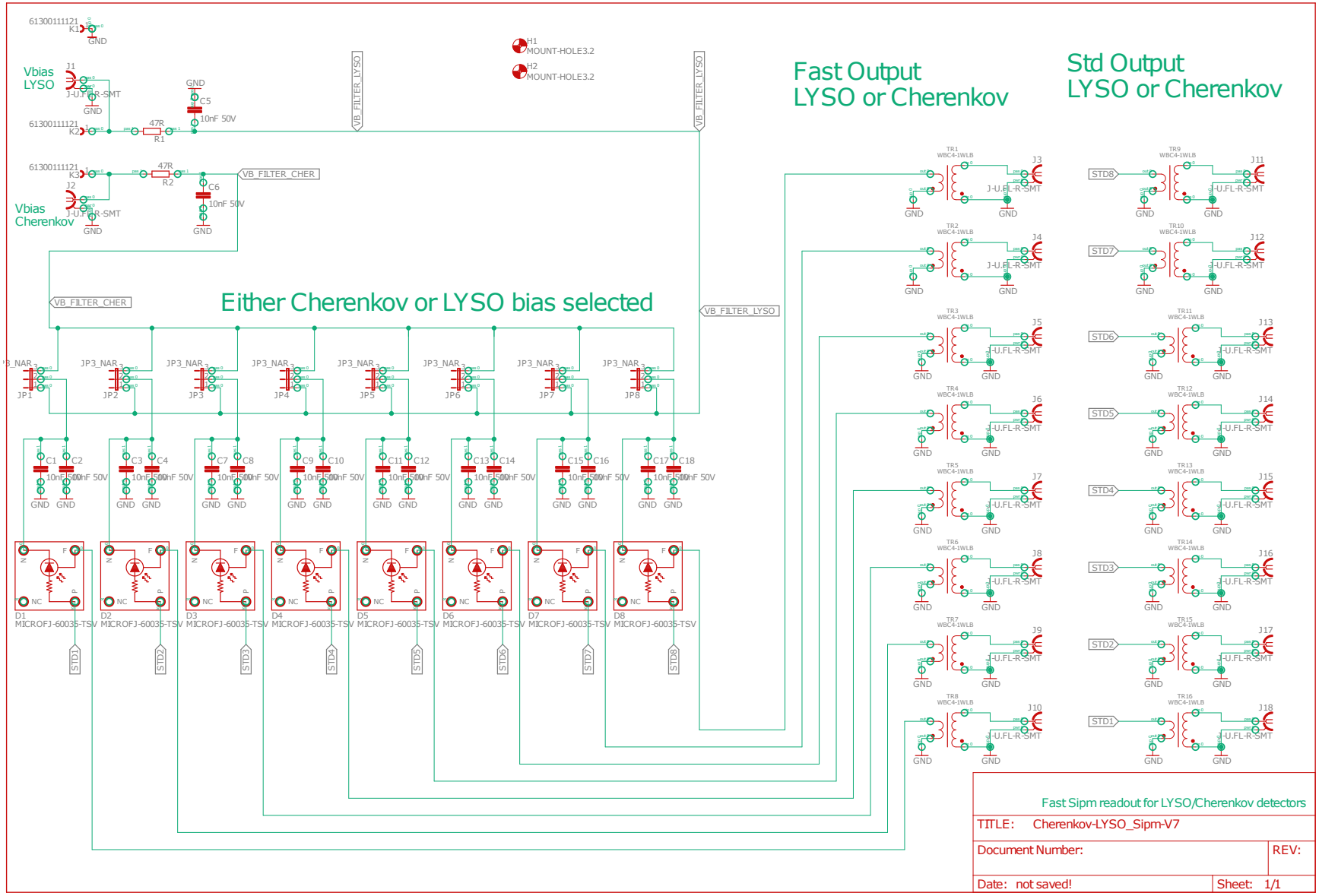

Figure 2.8: Schematic drawing of PCB used for detector array. Separate bias rails are included for Cerenkov and LYSO channels, selectable by jumpers (JP). Diode-type devices are SiPMs, which have both a fast and standard output, as described in [36], each with its own output connector. Schematic and design by Nikolay Pavlov[a].

[a] https://www.researchgate.net/profile/Nikolay_Pavlov

Each PCB handles 8 detector channels, in two rows pitched by 16 mm laterally. The dimensions of the board layout are shown in Figure 2.9. The dimensions were chosen such that inter-detector cross talk among the Cerenkov and LYSO elements is minimized (as simulated and benchmarked in [46]), while maintaining capability for 5 mm spatial resolution. The relationship of the specific packing ratio, which is greater than 1 given the acquisition geometry, to system spatial resolution, is discussed in detail later.

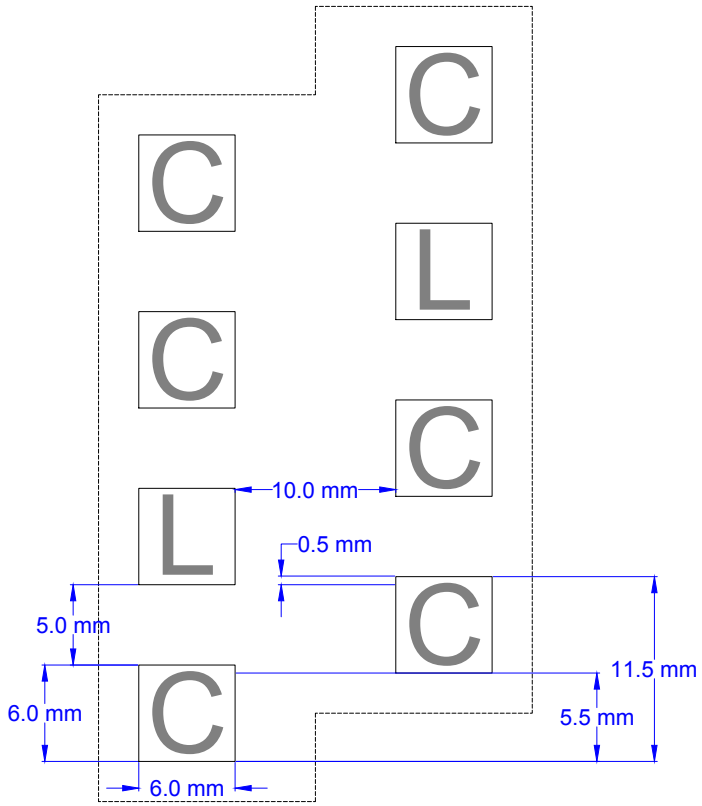

Figure 2.9: Dimensional drawing of arrangement of detector elements on array PCB. The letter "C" represents a quartz (Cerenkov) detector, while "L" represents a LYSO channel. Note that these dimensions are valid for the SiPMs themselves, but not necessarily for the detector elements, for which the LYSO are parallelepipeds (6x6x50mm), while the quartz elements are cylinders (6 mm diam x 50 mm).

The recent advent of entirely digital pulse processing in nuclear instrumentation has simplified readout system design over the historical nuclear instrumentation module (NIM)

bin slottable components, which required large, heavy powered crates and externalized coaxial connections to pass signals between the various processing modules. In this work, all-digital pulse processing is achieved through use of "off-the-shelf" digitizers made by CAEN SpA (Viareggio (LU), Italy).

Almost all of the data acquisition completed in this work was accomplished using the DT5730 family of digitizer [47] running CAEN's proprietary DPP-PSD firmware. These are 8-channel, desktop form factor digitizers with 14-bit (16384 channel) analog-to-digital conversion and a 500 MHz sampling rate. The single-end inputs are 50 Ω MCX female connectors, while software interfacing is via USB interface. The DT5730 supports multiple triggering modes, though self-triggering based on signal threshold level was used in this work. The data acquisition software used here is the CAEN Multi-PArameter Spectroscopy Software (CoMPASS), which allows selection of various parameters related to signal processing, as well as list-mode acquisition of data for postprocessing.

2.3 Operating parameters of SiPMs

Selection of operating parameters for the detectors of interest is typically a straightforward matter, particularly when many spectrometers shipped by manufacturers are prepackaged with a PMT, base, and preamplifier. The most important parameter for these is the operating voltage, which sets the dynode multiplication factor and therefore signal gain. In the case of SiPM-based detectors, operating voltage affects several performance metrics, and is therefore of even greater concern.

For SiPMs, which are semiconductor devices, operating voltage is usually discussed in terms of the overvoltage, which is the voltage above the breakdown voltage, the minimum bias at which the diode exhibits appreciable electron multiplication. The manufacturing processes producing the devices have narrow (but nonzero) tolerance, and the breakdown voltage may vary.

Device gain for SiPMs is typically on the order of 1×10^6. For the J-Series model from

ON Semiconductor, in use in this work, the gain is a nearly-linear function of overvoltage, ranging from about 1.3×10^6 at the manufacturer-recommended minimum overvoltage of +1 V to 7.4×10^6 at the maximum of +6 V.

The effect of overvoltage on gain is therefore an effect on ADC calibration. Due to selection of LYSO as the scintillation material, the self-count radiation was used to analyze aggregate effect of operating voltage on the entire photocouple output. The rare earth lutetium consists of 2.6% mole fraction lutetium-176, which decays by beta and prompt gamma emission [48, 15]. As shown in Figure 2.10, these gamma lines may be used to aid in ADC calibration at the low end of the dynamic range of the detector.

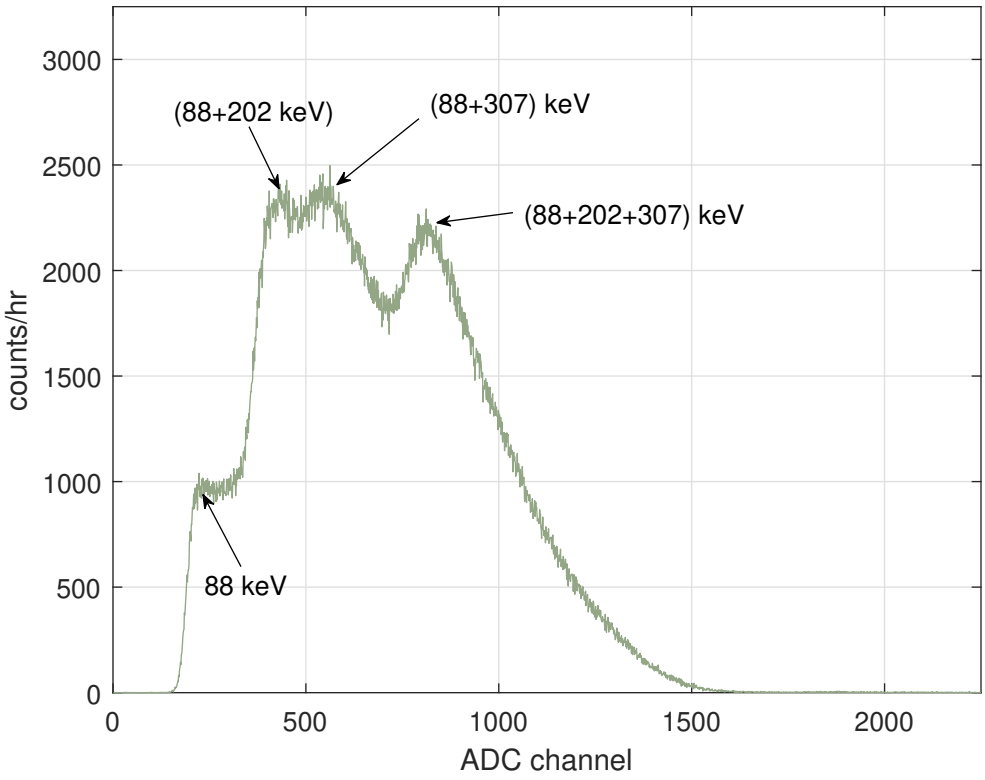

Figure 2.10: LYSO self-count at +26.5 V operating voltage, for a single element on the detector array, at 40 fC/LSB gain, showing lutetium-176 decay peaks. This data is specific to the crystal size used in this work, that is, a 6 mm × 6 mm × 50 mm parallelepiped – the spectrum will change with geometry (see [15].)

The self-count from the natural radiation in LYSO is nontrivially intense: in the rec-

ommended operating voltage range there several thousand counts per ADC channel at the low-energy end of the spectrum. This is not a concern provided that a sufficiently intense source is available, and as long as the relationship between the self-count intensity and operating voltage is understood. In order to evaluate this parameter, one-hour self-count measurements were taken at 0.25 V increments across most of the device operable range. The results are given in Figure 2.11.

In Figure 2.11, a number of features are immediately apparent. First, there is a distinct lack of energy resolution in the operating voltage range from 25.25 V to 25.75 V. These are very close to the manufacturer-recommended overvoltage floor of +1 V, with breakdown at 24.2 V. Though gain is ostensibly linear, dark current, dark count rate (DCR), crosstalk, and afterpulsing may not be, and the specification sheets for these devices include only measurements for these performance parameters at overvoltages of +2.5 V and +6 V – signal output is here considered empirically, as analytic investigation of diode-type semiconductor device performance is beyond the scope of this work.

Additionally evident in the self-counting curves is the spread of the aggregate number of counts – note that in the ordinate the scale is not identical between plots. The gain across the operating voltages up to about 27 V affects the signal in the expected manner, wherein the differential distribution of counts is spread across a greater number of bins while the number of counts per bin decreases, such that the area under the curve is constant (or nearly so). For operating voltages exceeding 27 V (or, overvoltage of +2.8 V), however, the integral number of counts increases as well. This is a disadvantageous effect, as high background count levels may saturate microcells in the SiPM, paralyzing them while coincident scintillation photons from external radiation events are not counted, until quenching occurs. An integrated self-counting curve is shown in Figure 2.12, which elucidates the sharp "takeoff" in the aggregate count numbers, and the counting plateau between 26 V and 27 V.

From these data, an operating voltage of 26 V was selected for the LYSO detector el-

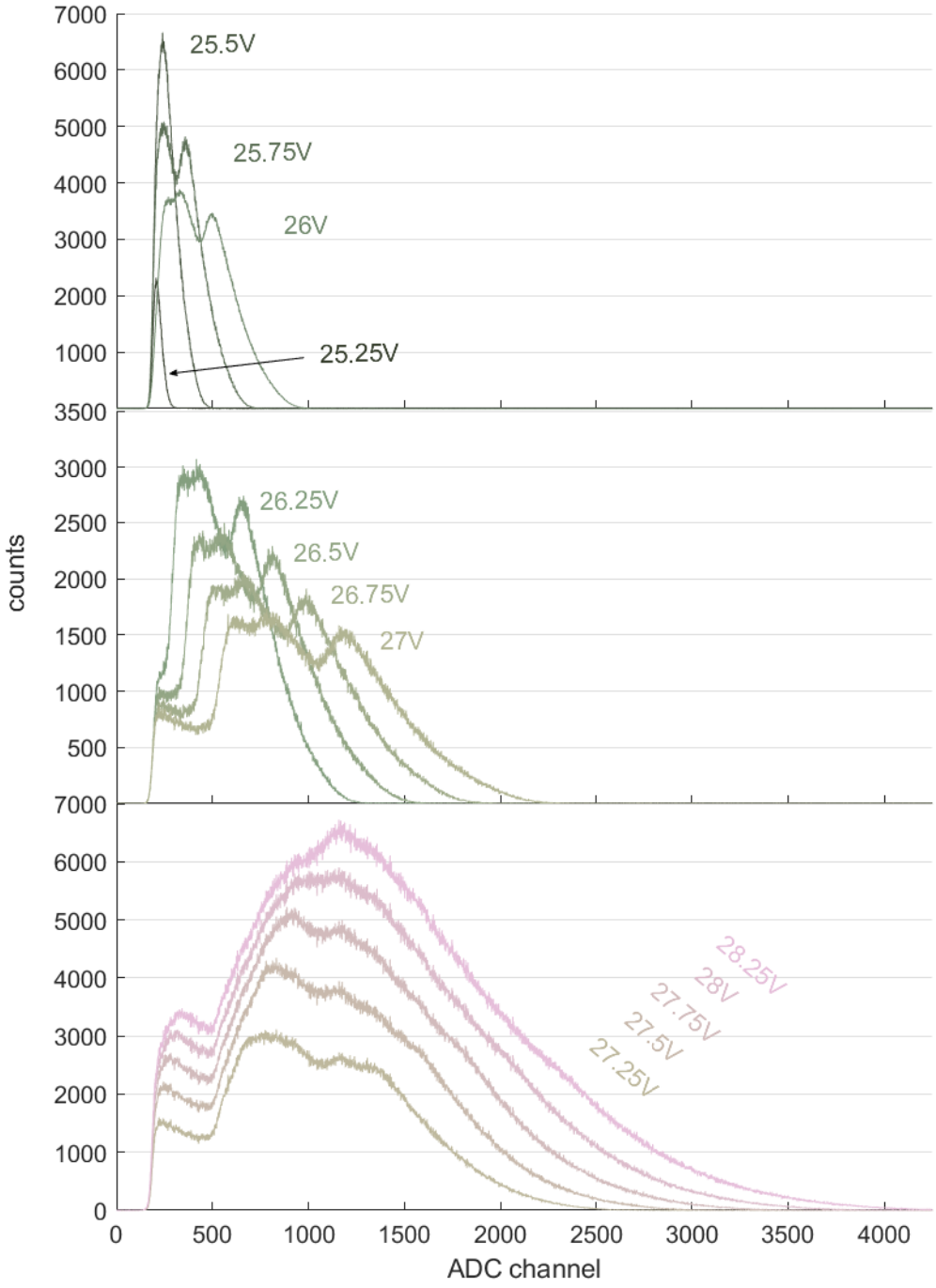

Figure 2.11: Self-LYSO counts for varying operating voltages of the SiPM, using the same photocouple and gain as in Figure 2.10. These spectra are dominated by the lutetium-176 decay, but also include typical background contributions. Count numbers are per hour.

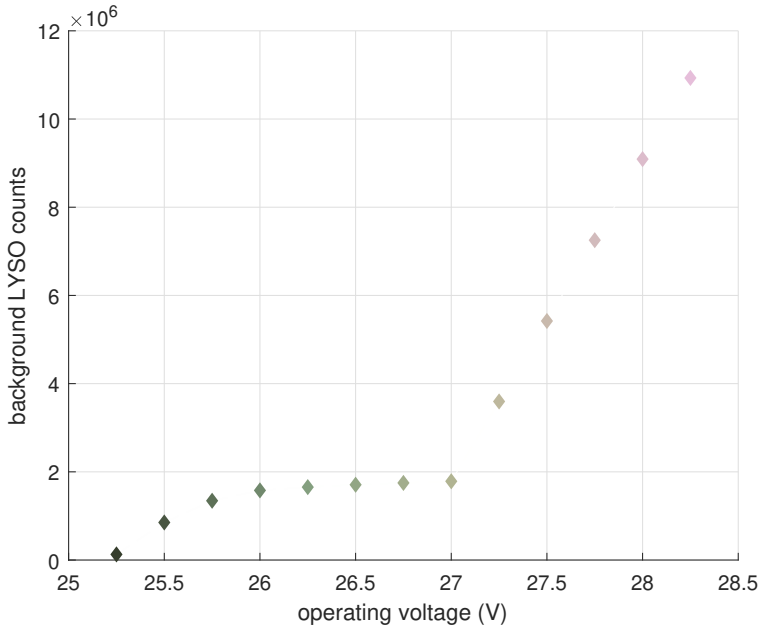

Figure 2.12: Integrated background (or self-) counts per hour for LYSO elements, from integration of curves in Figure 2.11. "Counting plateau" is clearly distinguishable, and count level beyond this region is nearly linear with respect to voltage.

ements, in order to ensure that background contribution was minimal while maintaining usable energy resolution across the entire dynamic range of the detector. The analogous background counting comparison for the quartz elements of the array is less interesting: during a 24-hour count, maximum integral background events recorded on a single channel was 18. Consequently, bias for Cerenkov channels was set at 29 V, such that the bias could be set collectively for all elements while ensuring that count numbers would be as high as possible to compensate for the inefficiency of geometry and radiation interaction. A higher bias was not selected for the practical concern of ensuring that variation in breakdown voltage due to manufacturing variance would not cause any devices to be operated outside of their recommended range.

Device calibration was conducted using several check sources: cobalt-60 and cesium-137 for the intermediate energy range between that of the internal radiation and the mega-electronvolt region. A sealed americium-beryllium (AmBe) source, one of several α-Be sources, was used in lieu of higher-energy MeV discrete lines, such as would be available

from an accelerator, due to availability. The AmBe source has a strong gamma emission probability at the 4.44 MeV line. Due to the thin geometry of the LYSO crystals, the prominent peaks just below 4.44 MeV in energy (the "escape peaks") are also used for calibration. All peaks chosen for calibration are given in Table 2.3.

Table 2.3: Decay counting peaks and corresponding ADC peaks used to create LYSO calibration curve

source	peak energy (MeV)	ADC channel	FWHM (ADC)
Cs-137 (backscatter)	0.184	147	29
Cs-137 (Ba-137m)	0.662	503	54
Co-60 (Ni-60*)	1.17	905	62
Co-60 (Ni-60*)	1.33	1026	75
AmBe (double escape)	3.42	2355	235
AmBe (single escape)	3.93	2650	272
AmBe (C-12*)	4.44	2925	150

The spectra recorded for a single LYSO channel of the cobalt-60 and cesium-137 check sources are shown in Figure 2.13. Both a weak (about 1 μCi) and a strong (about 1.6 Ci) cobalt-60 source were measured. A 24-hour background count including self counts was subtracted from each of the spectra. For the weak cobalt-60 source, this subtraction caused negative count data across a range of a few hundred ADC channels. This minor effect is most likely due to temperature fluctuations in the measurement environment – all SiPMs have temperature-dependent breakdown voltage. In J-Series devices, this dependence is 21.5 mV/°C [36], thus calibration in and around the counting plateau shown in Figure 2.12 will be mostly unaffected, but left-right shifts in counts per bin may lead to effects like that shown in Figure 2.13[3]. This effect is not seen in the cesium or strong cobalt spectra because the marginal differences between these and their corresponding background spectra was large.

In the spectra, the cesium-137 peak is easily distinguishable, as is the backscatter peak for the 0.662 MeV gamma ray. The normalized cobalt-60 spectrum is significantly less

[3]Assuming gain is a linear function of overvoltage, the temperature-dependent gain change is about 2.1×10^4/°C.

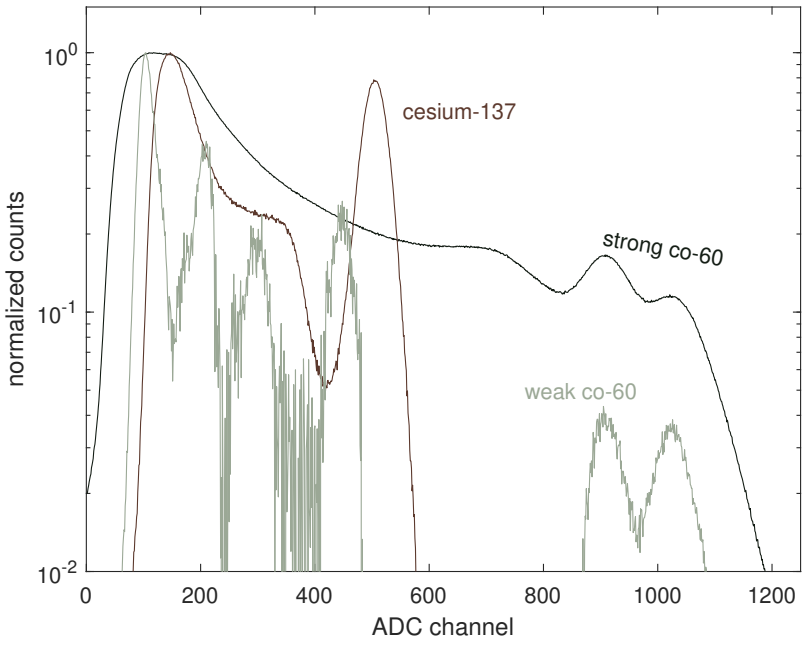

Figure 2.13: Uncalibrated cobalt-60 and cesium-137 spectra, measured on a LYSO detector element, at +26 V bias, 40 fC/LSB gain. Data normalized such that maximum count intensities are unity.

pronounced, reflecting the much lower probability of absorption of the 1.17 MeV and 1.33 MeV cobalt-60 gammas. The backscatter peaks are not actually distinguishable for either cobalt source, due to Gaussian blurring and ambient x-ray fluorescence contributions.

In the AmBe source spectrum, background subtraction again yields negative bin data, while several x-ray fluorescence lines are evident at low energies. The 4.44 MeV photopeak is difficult to discern. The low intensity of this peak is attributable to two factors: first, the dominant interaction in LYSO at this energy is pair production (see Figure 2.1a), while photoelectric absorption is negligibly probable. Further, the thin geometry of the crystal at 6 mm $\times$ 6 mm implies that not only are the gammas created following β^+ annihilation highly likely to escape the volume, but the positrons themselves may escape the crystal before annihilating. Thus, the escape peaks are more prominent than the photopeak (as expected).

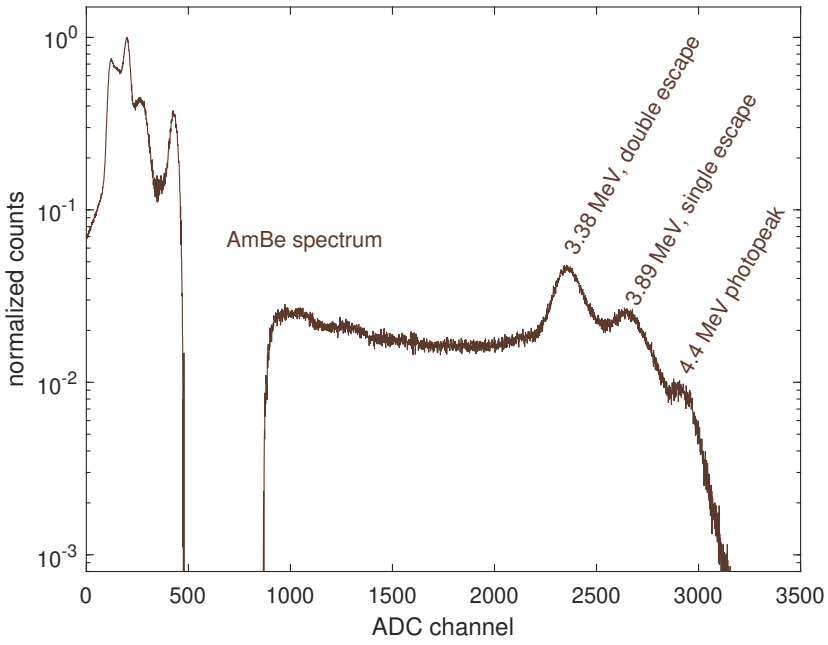

Figure 2.14: Uncalibrated AmBe spectrum, measured on a LYSO detector element, at +26 V bias, 40 fC/LSB gain. Data normalized such that maximum count intensities are unity.

Calibration of the LYSO-SiPM spectra for the analog-to-digital converter is performed by linear least-squares fitting of a quadratic curve to the experimental data. The calibration curve is very nearly linear and the associated fit carries a low residual, while energy resolution is between 8 and 12 percent up to the 4.44 MeV gamma of the AmBe source, suggesting that the overall suitability for spectroscopy applications is good, in conjunction with the results reported above (see Figure 2.15

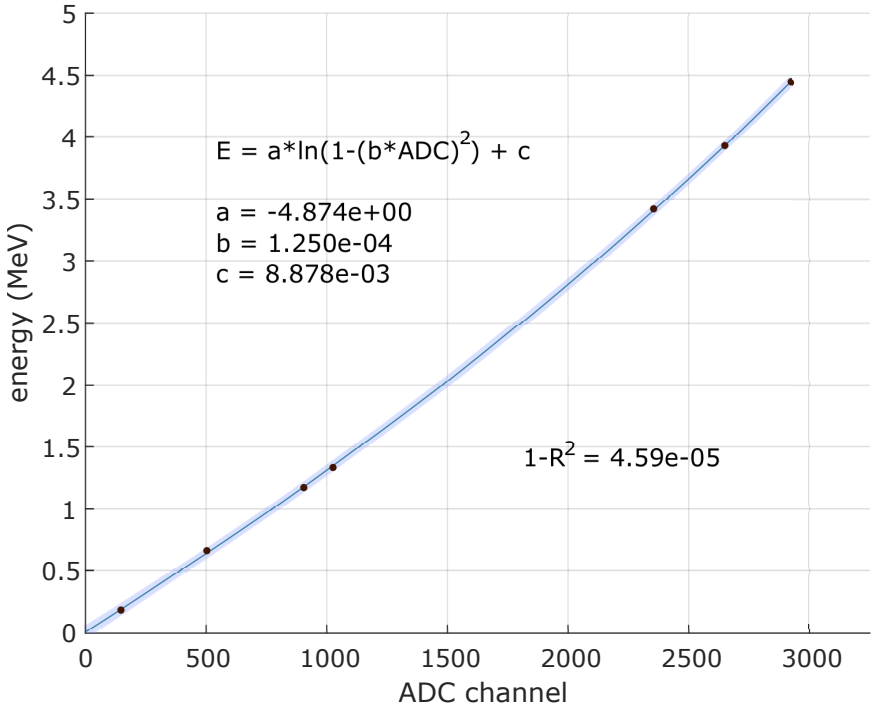

(a) ADC calibration curve. 95% confidence bounds are shown as a shaded region about the fit.

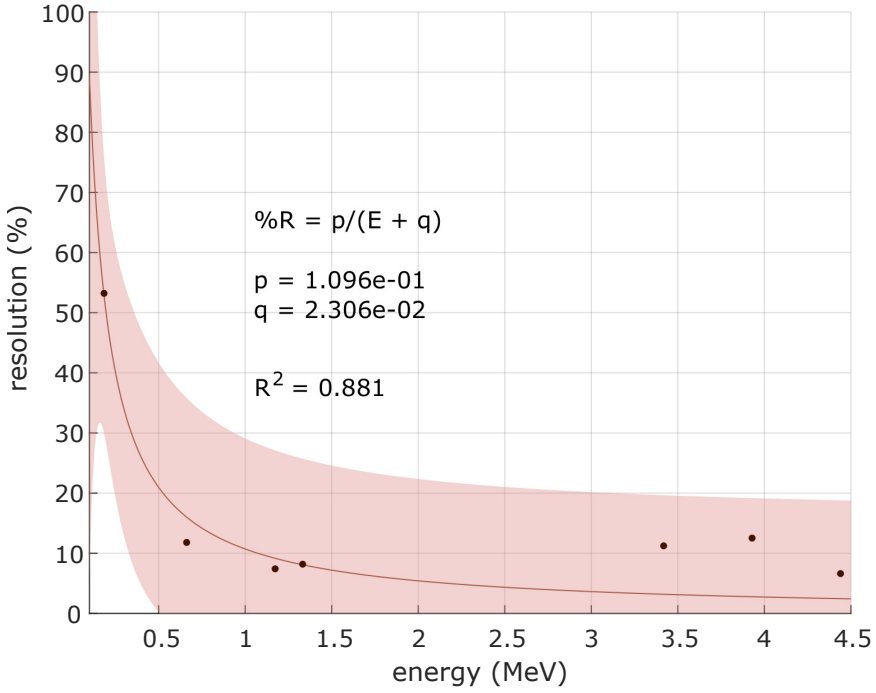

(b) Energy resolution curve. 95% confidence bounds are shown as a shaded region about the fit.

Figure 2.15: ADC calibration and energy resolution curves for LYSO-SiPM photocouple, at +26 V bias, 40 fC/LSB gain. Peak data is given in Table 2.3.

CHAPTER 3

IMAGING ALGORITHM

In order to understand the acquisition and reconstruction of images from the prototype array, data acquisitions were conducted with a Clinac-family megaelectronvolt-range linear accelerator (Varian Medical Systems, Palo Alto, CA). The particular linear accelerator (or, linac) used in this work is housed in the Radiological Science and Engineering Laboratory (RSEL) at the Georgia Institute of Technology. It can produce electron beams of 6 MeV to 22 MeV, and contains a bremsstrahlung target and filters for 6 MV and 18 MV-endpoint photon beams. To avoid neutron contamination and damage, most imaging work was completed with the 6 MV beam, at a dose rate of 600 monitor units per minute – beam output is noncontinuous, as the RF power is operated in a repeated pulse mode [49], such that electron bunches reach the bremsstrahlung target in millisecond-range intervals according to the set dose rate. Individual pulse magnitude is independent of flux rate in this system. The monitor unit (MU) is a contrived unit for medical accelerators which can be correlated to a dose rate given a conversion table at some depth in water. The Clinac at Georgia Tech is calibrated such that 1 MU of 6 MV bremsstrahlung photons yields a dose of 1 cGy at a depth of 1.6 cm in water, for a field collimated to 10 cm $\times$ 10 cm at a source-to-surface distance of 100 cm. An effective beam energy of 2 MeV is used where applicable [50].

A 100 mm linear translation stage from Thorlabs (Newton, NJ) was used to position objects and to move them across the field of view (FOV) during sliding window acquisitions. A Thorlabs BSC20x stepper motor controller was interfaced with the Kinesis software to control the positioning system. Acceleration was set to 1 mm/s^2 and velocity to 1 mm/s for all acquisitions, unless otherwise noted.

The CoMPASS software was used in combination with the desktop digitizers running

CAEN's DPP-PSD firmware, allowing list-mode writing of individual processed events to comma-separated output files per detector channel and per DAQ run. Events are time- and energy-flagged, and flagged for short- and long-gated energy, enabling pulse shape discrimination with appropriately chosen detection media. Acquisition settings are given in Table 3.1.

Table 3.1: Data acquisition parameters for CoMPASS software in image acquisitions

parameter	value
input dynamic range	2.0 Vpp
record length	992 ns
pulse polarity	positive
discrimination	leading edge
threshold	100 LSB
energy coarse gain	40 fC/LSB
DC offset	50%

Each data run was acquired by beginning x-ray emission from the linac, followed by simultaneous commencement of DAQ in CoMPASS and motion of the stepper motor. Since data acquisition began and ran concurrently with stepper motor driving, the time tags of list mode events could be directly converted to a spatial coordinate along the travel direction.

There are two basic methods of data acquisition using such a linear imaging array: "step-and-shoot" type and sliding window type acquisition. In step-and-shoot, the object is translated through the field of view and dwells at regular intervals along its length for some amount of time at each dwell position while exposed to the source and detectors are on. The data arrays corresponding to each set of acquisitions are then concatenated to form the image. In the sliding window scheme, the object is translated through the field of view, typically with some known constant velocity, and pixels of the image are "painted" in with counts as they arrive in detectors, according to time data of event arrival. Both acquisition types are valid, but it is usually mechanically simpler to implement the sliding window – this is the type under which imaging data was collected in this work.

The physical manner in which images is acquired is similar to the method employed

in flatbed document scanner. In the document scanner, the document is placed on the glass and a light source and detector array are translated across the length of the glass while acquiring data. The proposed cargo system acquires images in much the same way, except that the object being scanned is translated, rather than vice versa. These acquisition schema are isomorphic to a simple frame transformation, but differ in that the proposed array includes two rows of detectors instead of a single row, in order to reduce "cross-talk" between detector elements. Further, there is a standoff distance between the cargo detector array and the interrogated cargo, whereas in a document scanner the standoff distance can be made very close to zero. There are also disparate detector types used in the cargo array, a concern which merits special attention in image formation, and will be discussed in detail later.

3.1 Development of reconstruction model

A simple model for image reconstruction which was initially considered is a linear relationship between incident flux rate at the detectors and pixel intensity. A horizontal pixel size of 3 mm was selected such that per-pixel uncertainty in count number could be kept low while maintaining good horizontal spatial resolution in the direction of travel. Individual counts are apportioned or "binned" into pixels on a linear-interpolative basis. Because the object and *image* are located at the source-to-object distance (SOD) while the *detectors* are located at the source-to-imager distance (SID), the face of each detector is first backprojected by exploiting similar triangular geometry.

There is an intrinsic magnification which is apparent in any photonic imaging system not employing parallel beam trajectories, as in a pinhole camera or cone-beam x-ray radiography system. If the interrogating particles all originate from a point or point-like source, the magnification factor M in terms of the source-to-imager distance (SID) and source-to-object distance (SOD) is

$$M = \frac{SID}{SOD} = \frac{\text{image size}}{\text{object size}}.$$

An additional consequence of object magnification is the so-called "unsharpening," or geometric penumbra of the imaging system. The penumbra is a blurring which is evident at object edges, and appears due to the non-infinitesimal size of the focal spot from which interrogating particles originate. The magnitude of the geometric penumbra P is

$$P = f * \frac{SID - SOD}{SOD},$$

where f is the focal spot size (see [51]). From this, it is apparent that for a given f, edge blurring may approach zero if the object is placed as close as possible to the imager. Practically, this is difficult to achieve, given constraints under which scanners must be built, and thick objects have a depth-dependent penumbra. For all image acquisitions in this work, $SOD = 2.2\,\mathrm{m}$ and $SID = 4.6\,\mathrm{m}$, as in [11].

All detector faces are modeled as squares, for the sake of simplicity, and because optical photon scatter in the window and coupling silicone compound are possible and in fact likely processes. For the entire list of time tags of events, the position of the (virtual) row of pixels relative to the detector from which they will be binned is calculated: it depends only on the starting position, $v \cdot t_i$ (that is, the product of the velocity of translation and time tag), and whether the detector channel belongs to the first or second row.

The problem of correcting a time tag for whether the detector in which the event was recorded belongs to the first or second row merits additional discussion, as the two-row design of this array is unique, and complicates the simple geometric assumptions which could be made for a single-row linear detector array. The row number (either 0 or 1 in software) is simply multiplied by the horizontal detector pitch (see Figure 2.9), corrected for backprojection, and subtracted from the remaining terms. Note that this implicitly assumes that the geometry of the source-object-detector system is identical other than a positional offset for each detector row. If a point source is used for irradiation, as in this work, this "double parallel-beam" assumption is only nearly valid. However, the angular

offset θ_{off} between the "fan" components of the point imaging source at an imaging distance of 4.6 m for this array is only

$$\theta_{\text{off}} = 2 \cdot \arctan\left(\frac{\frac{1}{2}\,(\text{lat pitch})}{\text{SID}}\right) = 2 \cdot \arctan\frac{8\,\text{mm}}{4.6\,\text{m}} \approx 0.2^\circ\,.$$

Even at a distance of 1 m, the angular separation between detector elements is less than 1°, therefore no additional considerations for non-parallelity are included.

As the time tags are processed and the position of the virtual pixel row at the image plane is updated, counts are binned into pixels based on the magnitude of overlap between the backprojection of the detector face and the pixels themselves. Since pixels are assumed to be of unity detector height at the image plane, areal overlap need only be computed in the direction of translation. This may be accomplished by several methods: a fast method is a parametric 1D "ray-tracing" approach (as, for example, in [52]). In this work, it is actually accomplished via isomorphism of the system via a Galilean frame transformation to the case where the source and detector are translated simultaneously. Here, the left and right margins of the detector face are calculated at the time tag of interest, and composed in an ordered set with margins of the pixels which lie inside the margins of the detector:

$$d_{edges} = d_l \cup \{px_i \in px_{edges} \mid d_l < px_i < d_r\} \cup d_r\,, \tag{3.1}$$

where d_l and d_r are the left and right margins of the detector face and px_i is an individual element of the set of all pixel margins, px_{edges}.[1] The number of pixels the detector face overlaps is now given by $\text{N}[d_{edges}]-1$, where the operator $\text{N}[\cdot]$ gives the number of elements in an array or set. Thus, the overlap magnitudes are now determinable, given by subtraction of successive elements of d_{edges} from preceding elements of the same, as follows:

$$\Omega_{n-1} = d_{edges}(n) - d_{edges}(n-1) \quad \forall\ \{n \in \mathbb{N} \mid 2 \leq n \leq \text{N}[d_{edges}]\}\,, \tag{3.2}$$

[1] Definition of d_{edges} as a set containing unique elements ensures that coincident px_i with detector edges do not cause division by zero errors later in the algorithm.

where Ω_n is an overlap magnitude and $d_{edges}(i)$ represents the ith element of that set. The index i, which is the index of the pixel on the closed interval $[[1, \mathrm{N}[px_{edges}] - 1]$ overlapping the projection of the detector face at the time tag of interest, is then given by

$$i = 1 + \left\lfloor \left(\frac{1}{2}(d_{edges}(n-1) + d_{edges}(n)) - px_{edges}(1) \right) / w_p \right\rfloor , \tag{3.3}$$

where w_p represents the width of a pixel, *not* a detector, and $\lfloor \cdot \rfloor$ represents the floor operator, which maps its argument to the nearest integer less than or equal to the argument. There may be some cases where the pixel index is calculated outside the array – for example, if data acquisition runs too long, the velocity-time tag product will grow too large. In these cases, the Ω_n and i values may be discarded, provided that

$$\neg \left(0 < i < \mathrm{N}[px_{edges}]\right) \tag{3.4}$$

is true.

In the simple model where flux and pixel intensity are linearly proportional, the overlap magnitudes Ω_n are considered as weighting factors for the binary photon detection. That is, if an event is recorded, the overlap magnitude – or some function thereof – weights a value of 1, representing that an event was registered in the detector at a point in its "transit" when it overlapped one or more pixels at index (or indices) i. A fractional count of magnitude $\Omega_i \cdot 1$ is binned into each pixel i. A linear count weighting schema assumes that overlap magnitude is proportional to the probability that the count was detected in pixel i:

$$r_i = r_i + \frac{\Omega_i}{w_d} , \tag{3.5}$$

where i is the ith pixel in the current row, r, of pixels in the image, and overlap magnitude is normalized to the detector width w_d. Necessarily, $\sum \Omega_i = w_d$, so this operation ensures that weighted counts sum to unity, though overlap magnitude may be normalized arbitrarily,

as pixel magnitudes are normalized to flat- or bright-field acquisitions.

When the binning process has been completed for all detector channels, the image may be reconstructed in this model by simply "stacking" the pixel rows generated in a multi-dimensional array. Each row can then be background-corrected and flat-field normalized. In the flux-proportional model, background subtraction is done by subtraction of the background count rate in each pixel from the total count rate in that pixel, provided that each is normalized in the same way – say, to number of counts per second. Background data acquisitions should be long, as the background count rate is orders of magnitude below the image count rates. Flat-field normalization is carried out in a similar manner. The flat-field intensity I_0 is defined as the measured pixel intensity when no object is present under normal imaging conditions. The flat-field and image intensity with object present, I, are each background corrected. Their ratio is the normalized image value:

$$f = \frac{I - b}{I_0 - b}, \tag{3.6}$$

with background rate b, for all pixels in the image f. In an ideal sense, flat-field normalization removes the dependency of individual detector response on variations in light transport, material attenuation coefficient in the medium, and so on. In this way, f should be a reasonably close approximation to the ideal thin-beam attenuation ratio predicted by the 1D Beer-Lambert law:

$$\frac{I}{I_0} = e^{-\int \mu(x)dx}, \tag{3.7}$$

for spatially-varying total attenuation coefficient μ and spatial parameter x.

An initial image reconstructed using the approach described above is shown in Figure 3.2 – this is a reconstructed image of a 1 7/8" socket wrench attachment, of which reference photographs are shown in Figure 3.1.

A few features are immediately evident in the reconstructed image. First, the useful range of the LYSO photocouples is very low, though the signal level is high relative to

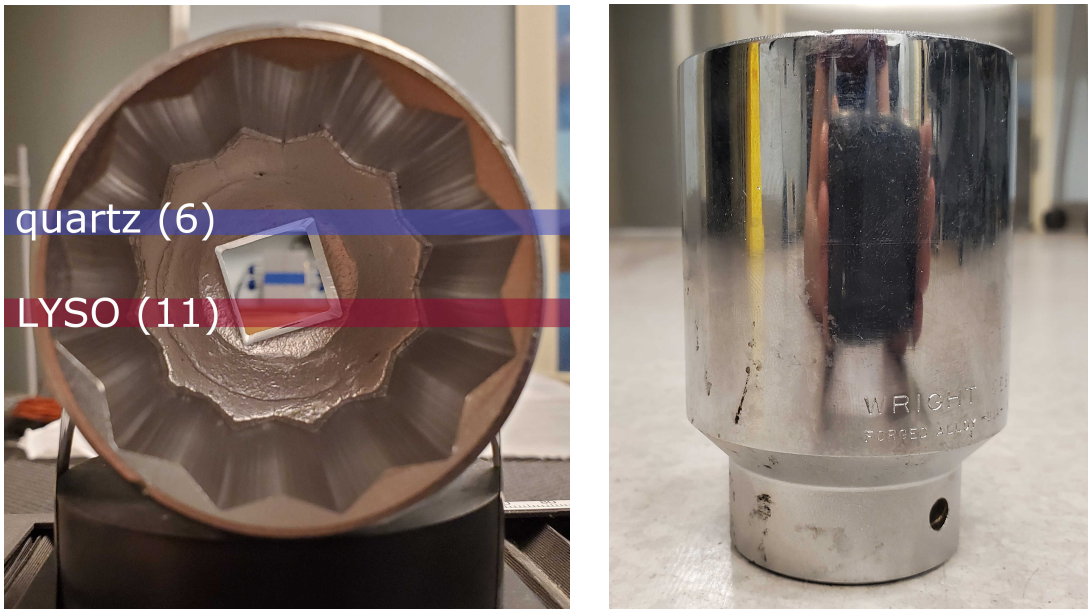

(a) Front view (b) Side view

Figure 3.1: Front (left) and side (right) views of 1 7/8” socket attachment used in imaging tests. The approximate locations of the backprojections of a single quartz and LYSO channel are highlighted on the front view – data from these channels is analyzed in several figures below.

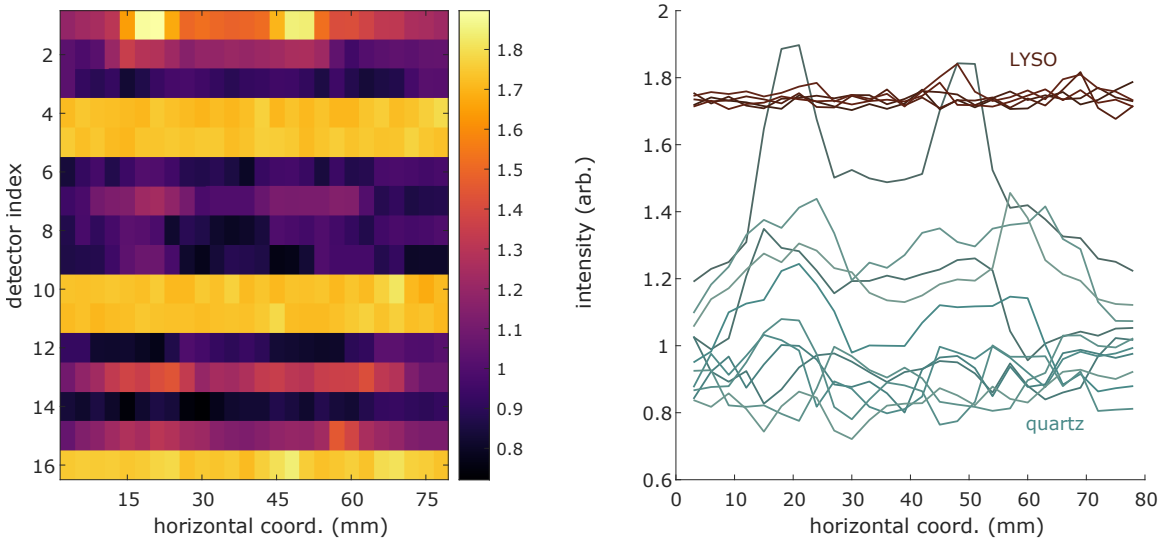

Figure 3.2: Image reconstructed by initial algorithm, without corrections, and corresponding line profiles horizontally across the image.

Cherenkov detector intensities. Further, it is difficult or impossible to discern image features – the difference in signal levels contributes to this, but distinct features in the data are either obfuscated or not present.

3.2 Refinement of imaging model: response weighting

A plot of count rate as a function of time is not particularly illustrative in this case – it may even lead to the conclusion that the LYSO channels are completely saturated and thus an ineffective choice of detection mode in such a high-flux environment. A bivariate histogram which bins all counts in the acquired listmode data on the basis of time tag and energy recorded in the event is more informative. Such histograms are shown in Figure 3.3, for both a quartz and a LYSO channel.

Qualitative analysis of the histogram features seen in Figure 3.3 informs the first refinement made to the image model. First, the maximum count intensities per bin are observed in ADC channels corresponding to low-energy counts – the ordinate is uncalibrated, but there is an obvious "splitting" of the count intensities into high-intensity and low-intensity bins. The regions of high and low intensity may be analyzed separately, using an appropriately chosen cutoff ADC channel, which may be determined on a per-detector basis by analysis of the count "forests" generated.

In the lower band for the Cerenkov radiator, there are notable depressions in the number of counts per bin near the upper end of the band, corresponding to shifts in aggregate count energy toward higher channel numbers in the upper band. Depressions in aggregate upper band energy from the baseline (that is, uninterrupted flux outside the margins of the imaged object) correspond to transitions of the lower count band to a wider distribution in ADC channels, as seen near the 21 mm and 77 mm travel distances in Figure 3.3. Note that due to the selection of system parameters, the abscissa in this and other plots may also be read as time in seconds since acquisition commencement – these parameters may be used interchangeably.

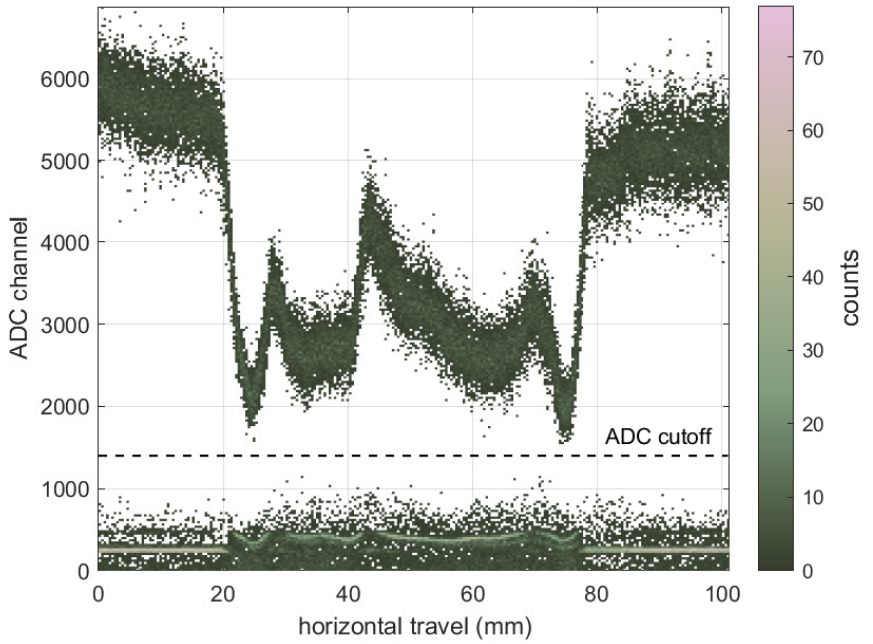

(a) Bivariate histogram of time tag vs. recorded energy for all events occurring in detector channel 6 (quartz) during acquisition on socket test object.

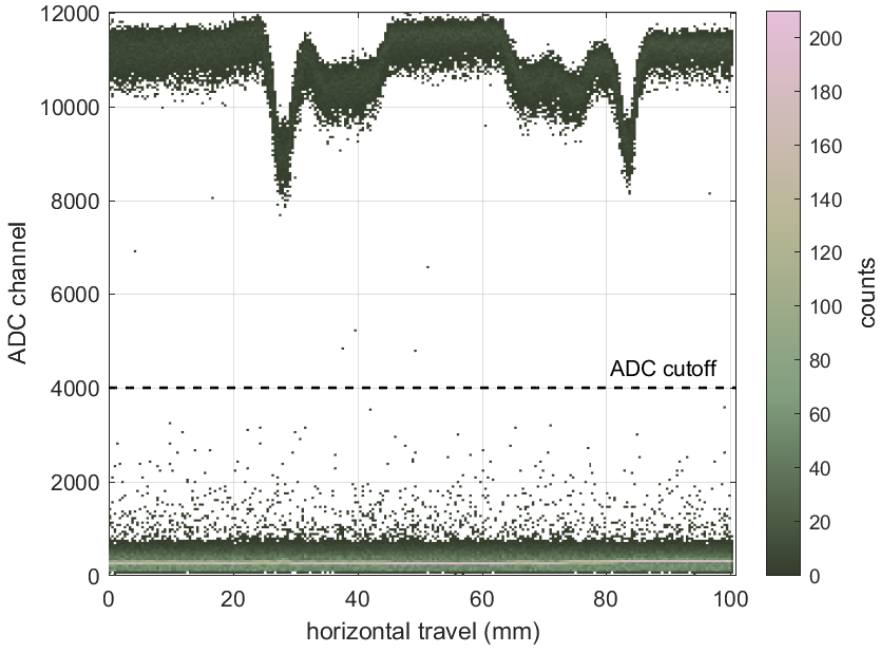

(b) Bivariate histogram of time tag vs. recorded energy for all events occurring in detector channel 11 (LYSO) during acquisition on socket test object.

Figure 3.3: "Light-splitting" effect observed in LYSO-SiPM photocouples, so termed because in the LYSO case, the lower band was originally thought to be exclusively due to self-counts from lutetium-176.

Analyzing the LYSO plot in Figure 3.3b, it should first be noted that it is necessary to choose a higher ADC cutoff, because the flat-field intensities in the upper band are centered near a much higher channel than in the quartz case (about 11 000 vs between 5000 and 6000 for quartz). Further, the lower count band is more heavily upper-skewed – that is, the median is above the mode for the LYSO. The correlation features, if present, are less obvious. A decrease in lower-band maximum bin counts is barely discernible near the 30 second acquisition point, corresponding to the drop in aggregate upper band energy.

Observation of Figure 3.3 and Figure 3.1 leads to the obvious conclusion that it is detector response and not binary count presence which should form the basis for image reconstruction in this particular application. Note that a frame transformation reversing the translation direction is assumed in these acquisitions, such that horizontal coordinates in the image shown in Figure 3.1a are mirrored in the bivariate histograms in Figure 3.3. Thus, the sharp peak near 45 mm in the quartz acquisition corresponds to the upper-right corner of the square cutout at the back of the object: the flux reaching the detector is nearly undisturbed at the corner, and quickly falls off after it is "seen" in the projection as more steel translates across the FOV. The sharp dips near 21 mm and 87 mm in the quartz case and 26 mm and 85 mm in the LYSO case are the points where the beam's path length through the steel is longest – about 63 mm, while the recorded aggregate detector response drops to the lowest point in each of the upper bands. The broad, flat region between 45 mm and 75 mm in the upper band of the LYSO acquisition clearly coincides with the path the open square traverses across the detector.

Of additional mention is that recourse to a simple count rate method would not suffice for reconstruction, even with ADC thresholding of counts on a response basis. In fact, as shown in Figure 3.4, splitting the apparent light output in each band and reconstructing the image profile from count rate yields a near-constant count rate in the high-light band, while the low-light band also has no apparent correspondence to the expected profile.

A possible assertion might be that the "low-light" counts as termed here do not con-

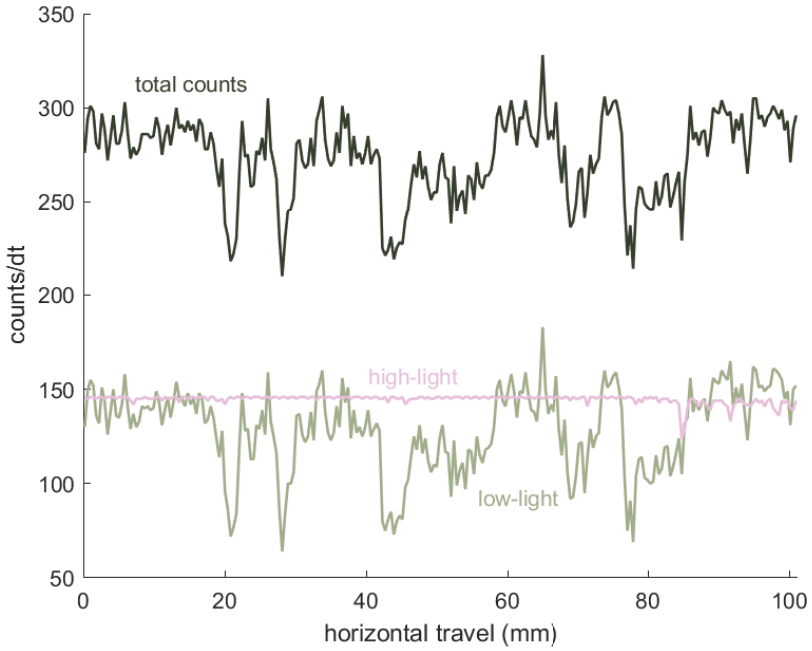

(a) Count profiles for quartz detector channel (index 6).

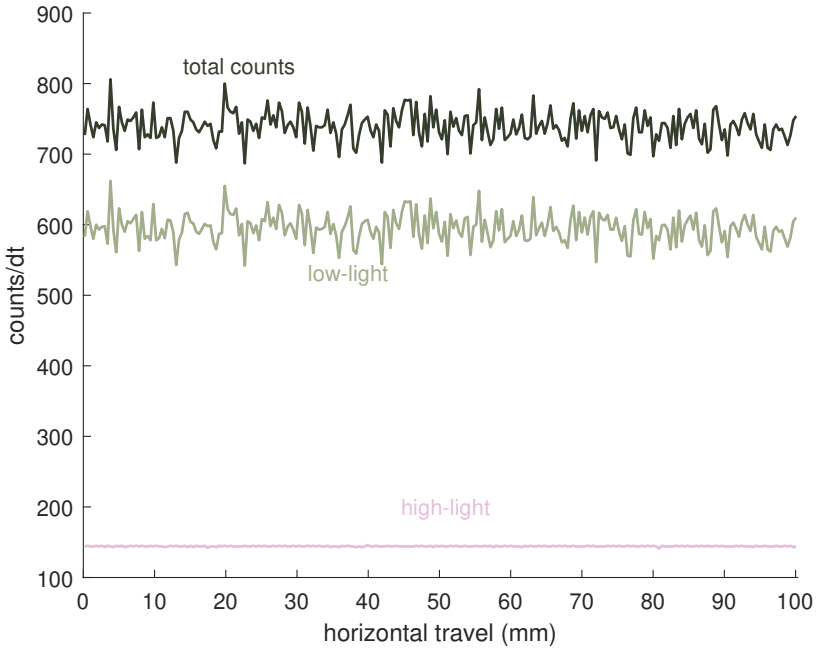

(b) Count profiles for LYSO detector channel (index 11).

Figure 3.4: Count profiles for a single quartz and LYSO photocouple (see Figure 3.1a) after reconstruction in a weighted-count sense based on linear flux model. Profiles are shown for reconstruction from high-windowed, low-windowed, and total-windowed count data, using the ADC cutoffs shown in Figure 3.3.

tribute to image quality – this bears some measure of justification, as a reconstruction algorithm cannot be confidently implemented unless the inputs to the system are well-understood and characterized. The timing distribution of imaging counts is of interest in order to investigate this, as this can inform rejection of correlated noise, such as intercell crosstalk and afterpulsing [53, 54]. Under light-emitting diode illumination of a photodiode, the light intensity may be known with precision and the emitter switched on and off. Correlated noise effects may be separated by inspection or algorithmically. For a scintillator or quartz photocouple which constantly produces light from background radiation as well as imaging irradiation, the process is more difficult.

Distributions of photocouple response as bivariate histograms versus the "intertime" for each event are shown in Figure 3.5 for the quartz detector and Figure 3.6 for the LYSO detector. In the quartz detector, the events are tightly grouped in the intertime range beyond 10 µs. Those events having intertimes below this value are shown in region and detail view A. Events in this "fast" region account for about 47% of histogram counts. Those in region B lie entirely in the Δt bin [2.75,2.79) ms, which is exactly as expected – these events correspond to linac pulses, as the repetition rate for pulses at the 600 MU per minute dose rate is 2.78 ms [55]. Given this repetition rate, 3.60×10^4 pulses are expected in a 100 s acquisition window. As 3.63×10^4 are recorded in region B and 0.006×10^4 in region C, those in the fast time region may be regarded as correlated noise. Further justification is derived from the very low background count level expected in the quartz photocouple, and which would if present be Poisson distributed, rather than tightly grouped. It is also apparent from this plot why count rate is a poor choice as a surrogate for image intensity: each pulse corresponds to a single count (or very nearly so). Though the pulse width is only about 3 µs [49], the output flux of the linear accelerator is sufficiently high as to render counts non-rare, and so many microcells are fired that ADC pulse integration occurs over a summed macro pulse combining the contributions from each microcell. Pulses in region C are likely the result of "dropped" pulses, wherein electron gun pulses were desynchronized

from microwave pulses, leading to a loss of acceleration. As a result, the next pulse in the train appears at twice the typical time interval.

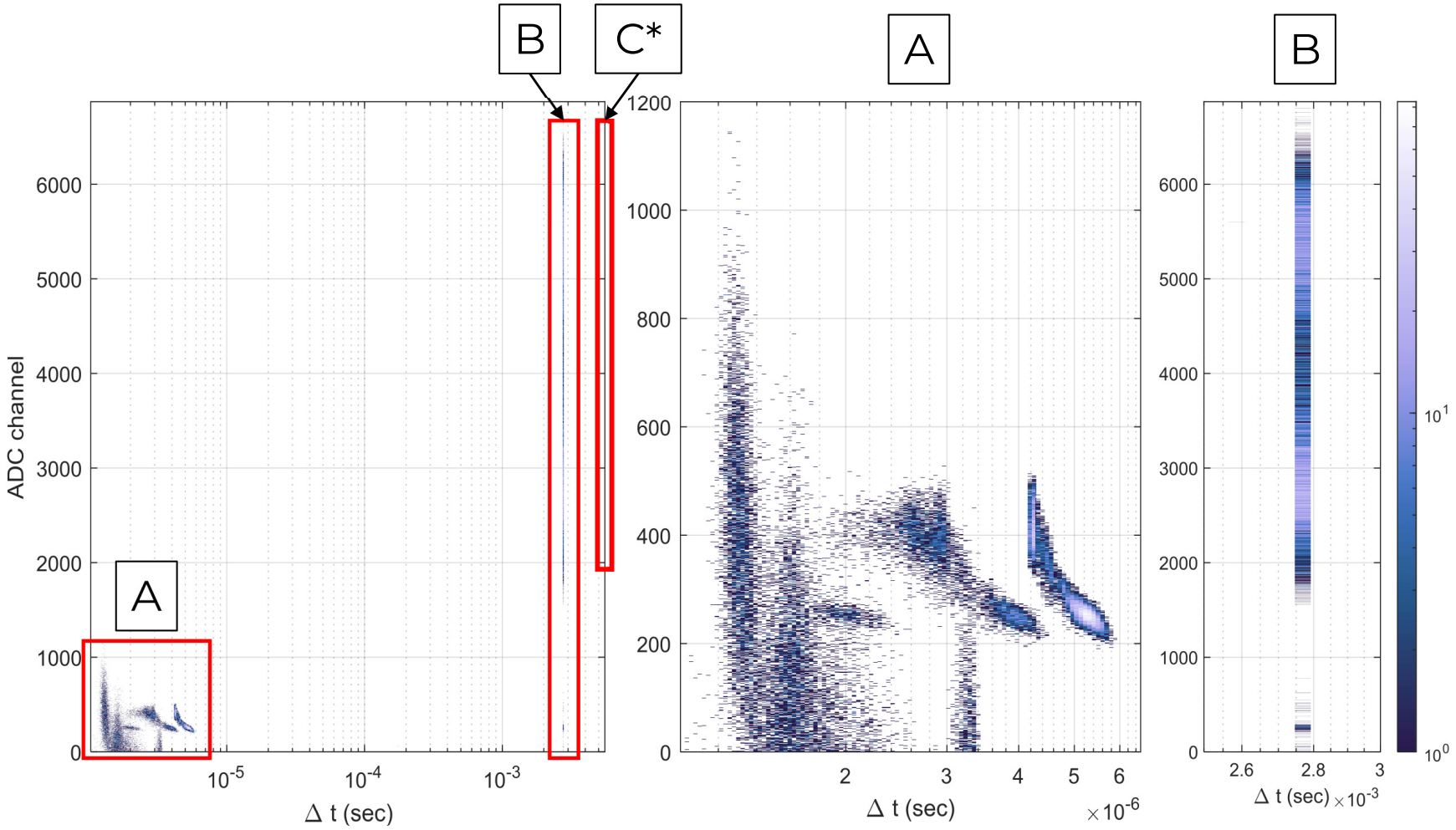

Figure 3.5: Correlated noise and signal counts in quartz detector, shown as a bivariate histogram of difference in time tag between successive events and recorded event signal, in ADC channels, for a single quartz photocouple (index 6). Bin edges are logarithmically spaced in Δt, and linearly in ADC (501 $\times$ 16 384 edges). Detail views are shown for regions A and B. Region C contains only 60 counts in the rightmost Δt bin, [5.5,5.6) ms.

The LYSO detector's intertime histogram, as shown in Figure 3.6, is more difficult to interpret. Events in the last intertime bins, with Δt in [2.73,2.78) ms account for under 5% of the expected 3.60×10^4 pulses. Events in the broad cloud extending between ADC channels 8000 and 12 000 and intertimes of 2×10^{-5} s to 2.78×10^{-3} s are not attributable to the lutetium-176 present in the background of the scintillator, as Figure 2.10 shows from the ADC range occupied by the background spectrum that it does not have this extent – internal radiation events are expected in the lower cloud band, inside of the 2000 channel response level. As the Poisson background is low in energy, a reasonable assumption is that channel-based (or, if calibrated, energy-based) thresholding is appropriate to select out signal events from noise events. Indeed, summing the events above the cutoff shown in Figure 3.3b reveals that the number of counts in this band (including those in region B) is within a single standard deviation of the number expected, $36\,000 \pm 190$. The upper-intertime truncation in the lower cloud of counts corresponding to the background spectrum is readily attributable to a single effect: that background radiation is present and not rare in LYSO. In fact, almost all events in the upper Poisson band directly follow events from the lower Poisson band, which can be shown by indexing the list of events and mapping the intertime histogram of preceding counts. Thus, background events occurring in the intertime window between 0 and 2.78 ms appear as expected, while almost all events in the upper ADC channels follow background events such that their intertime sums are 2.78 ms.

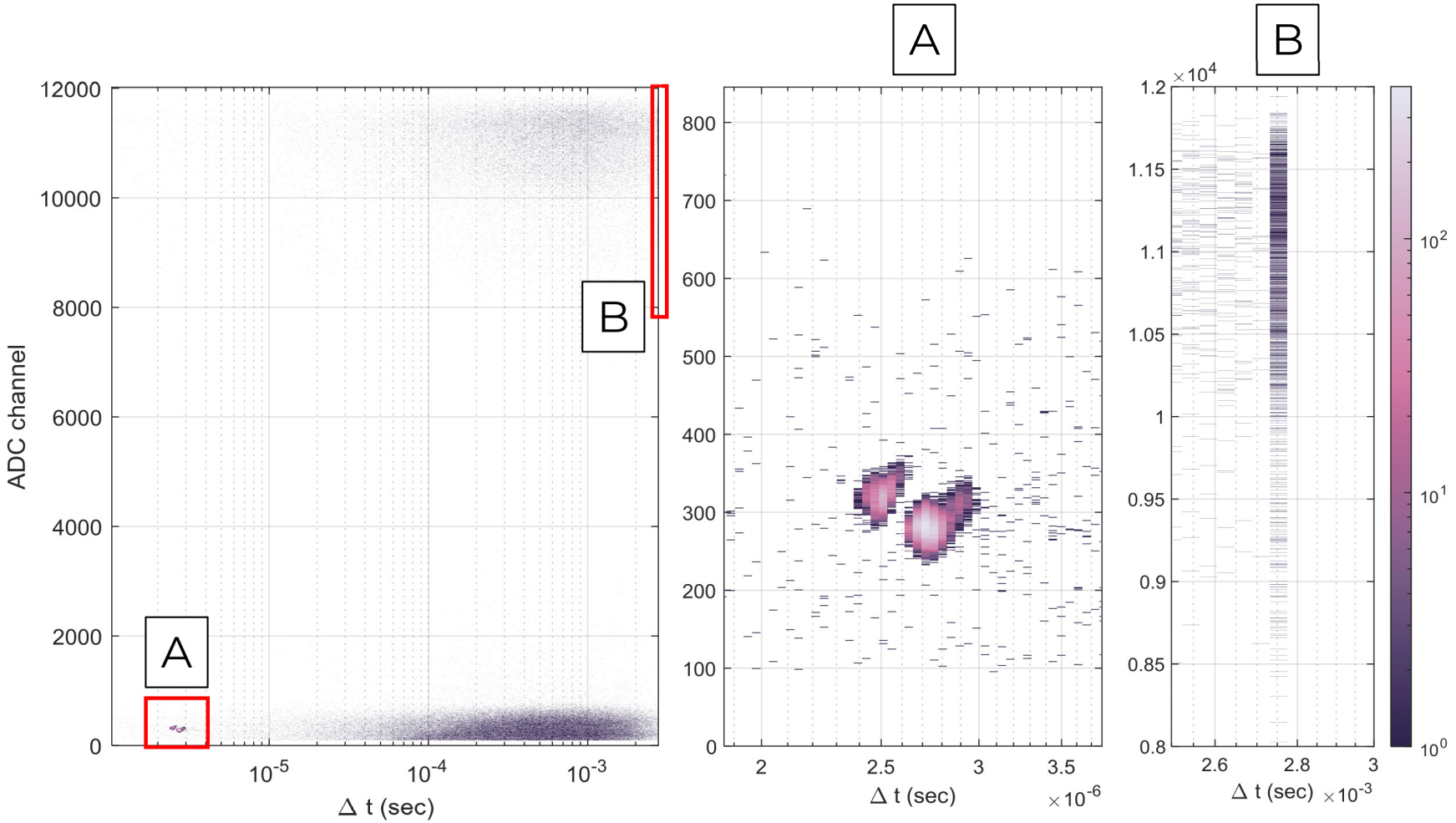

Figure 3.6: Correlated noise and signal counts in LYSO detector, shown as a bivariate histogram of difference in time tag between successive events and recorded event signal, in ADC channels, for a single LYSO photocouple (index 11). Bin edges are logarithmically spaced in Δt, and linearly in ADC ($501 \times 16\,384$ edges). Detail views are shown for regions A and B.

In selecting events which are used in reconstruction for each detector type, it seems that an intertime threshold is the most appropriate method for quartz, while an ADC threshold is appropriate for LYSO. In practice, the low-energy events in the rightmost intertime bin of the quartz detector are also separated into a low and high band – the low band events most likely correspond to prompt cross-talk, a type of correlated noise which negatively contributes to the image. As a result, ADC thresholding is implemented for both types of detector in this work.

The aptitude of quartz detectors as a choice for a photoconverter for this type of imaging application is nonetheless illustrated as a contrast between Figure 3.5 and the corresponding LYSO plot in Figure 3.6: background radiation triggers event in a Cerenkov radiator so rarely that it is not expected to occur during the acquisition window, and correlated noise events are so well-separated in intertime that additional filtration could be employed on this basis, if desired. The quartz imaging spectrum also covers a lower ADC dynamic range than the corresponding LYSO spectrum, due to a combination of efficiency and light output difference and nonlinearity of light response resulting from the nature of SiPM operation.

Two refinements may now be made to the reconstruction modality, response thresholding and response weighting. From the discussion above, it is evident that each pulse of the imaging source corresponds to a single count in the detector system. Thus the response level is ostensibly some function of the incident flux at the detector, as predicted from Figure 3.3. The response weighting method implemented here will weight each count into pixels first on the basis of backprojected overlap, and then scale those counts on the basis of their energy tag value. More precisely, the linear weighting schema of Equation 3.5 is updated as

$$r_i = r_i + \left(\frac{\Omega_i}{w_d}\right) \cdot E_t \,, \tag{3.8}$$

such that weighting by energy tag of the current event, E_t, matches the counting profile accurately to the intensity profile. To illustrate this method, and as further justification that the ADC channel thresholding method is reasonable, image intensity profiles using

this method are shown in Figure 3.7, which may be compared against the count forest plots in Figure 3.3 and the visible light image in Figure 3.1. The quartz case is an evident demonstration of the power of this method to both accurately predict the image profile and to improve contrast: including the correlated noise in the image, the profiles are nearly the same, while the high-windowed profile matches what would be predicted from the forest plot while covering a greater dynamic range. The contribution of the noise is so low because weighting by energy tag for those counts is much less significant than for signal events, which are in a higher energy band. Reconstruction of only the low-windowed events reveals no apparent correlation to the expected profile. The LYSO plot at first appears even more dramatic, but covers only a small dynamic intensity range. Low-windowing the scintillator plot implies image reconstruction from self-count radiation, with no useful data to be found. Thus, the ADC thresholding method appears to be justified, with the caveat that each detector covers a different range after normalization, due to aforementioned nonlinear response of SiPMs to various light levels.

3.3 Calibration for high-flux imaging applications

This nonlinear response of the silicon photomultipliers with respect to imaging flux is a critically important consideration in the described system. Since they are typically used to detect several-photon events, SiPMs are typically considered to be and operated as "photon counting" detectors, with the implicit model being that a single fired microcell is the result of a single-photon event and contributes additively to the output pulse height. In the case that multiple photons impinge on the SiPM surface within the quenching time of the microcells, there is a nonzero probability that two or more photons may strike the same microcell before it fully resets, leading to response nonlinearity – this is most evident when

$$N_{\text{photons}} > N_{\text{microcells}} ,$$

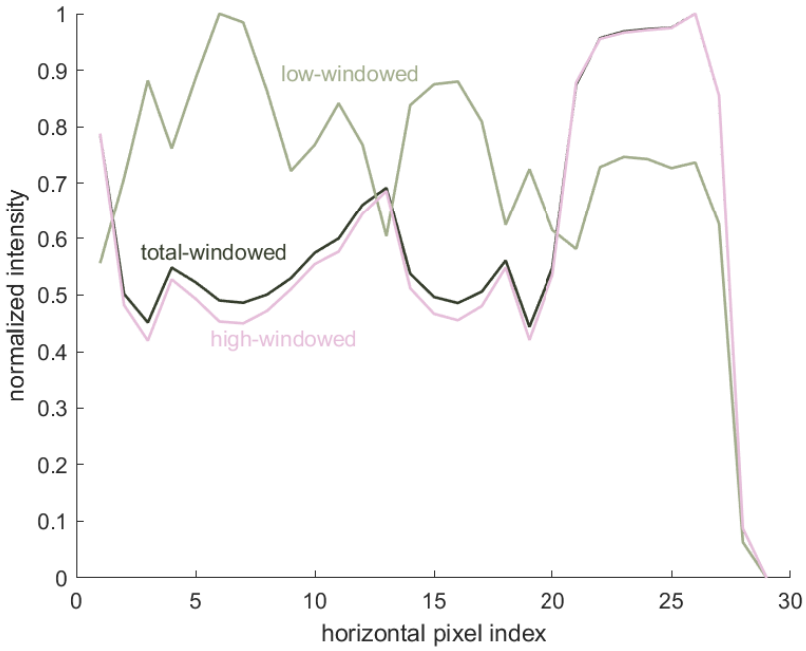

(a) Intensity profiles for quartz detector channel (index 6).

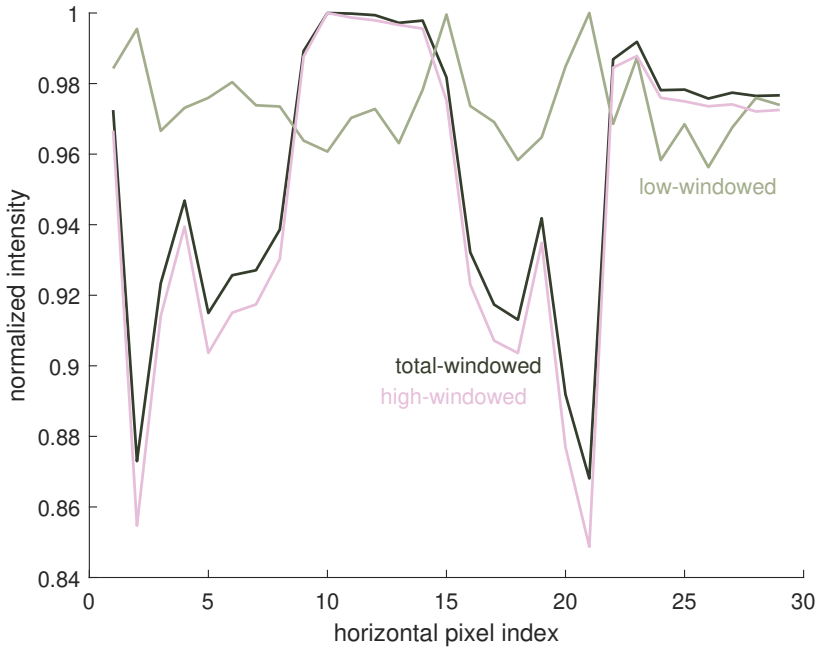

(b) Intensity profiles for LYSO detector channel (index 11).

Figure 3.7: Intensity profiles for a single quartz and LYSO photocouple (see Figure 3.1a) after reconstruction in a response-weighted sense based on linear flux model. Profiles are shown for reconstruction from high-windowed, low-windowed, and total-windowed count data, using the ADC cutoffs shown in Figure 3.3.

in which case at least one microcell must be saturated during a photon event, by the pigeonhole principle. In the worst case of all microcells firing within the reset time window of the electronics, the number of incident photons is indeterminate. The expected signal level, which *is* linear with respect to the number of microcells fired N_{fired}, therefore depends on both the number of available microcells and the number of incident optical photons N_γ. If each optical photon generated has an equal probability of hitting each microcell, then for a given number of optical photons, the probability of having U *unfired* microcells in a detector containing N_{cells} total microcells is

$$p(N_{\text{cells}}, N_\gamma) = \binom{N_{\text{cells}}}{U} \sum_{v=0}^{N_{\text{cells}}-U} (-1)^v \binom{N_{\text{cells}} - U}{v} \left(1 - \frac{U+v}{N_{\text{cells}}}\right)^{N_\gamma} , \tag{3.9}$$

by analogy to a special case of the "birthday problem" [56].

In practice, however, large binomial coefficients are costly to compute. Empirical data showing silicon photomultiplier response nonlinearity with respect to gamma energy has been characterized [53, 57], wherein the number of photons is proportional to the deposited gamma energy, and the microcell reset time is sufficiently fast to render contributions to nonlinearity from coincident multiple decay events negligible. The dependence on microcell number has been demonstrated [58], and it has been suggested [59, 60] that the number of microcells fired is an exponential in the number of incident photons:

$$N_{\text{fired}} = N_{\text{cells}} \cdot \left(1 - e^{-\frac{N_\gamma \cdot \text{PDE}}{N_{\text{cells}}}}\right) , \tag{3.10}$$

for devices containing up to a few hundred microcells. As expected, this exponential model is an approximation to the expectation values derived from a Poisson distribution of cell hit numbers. Its inverse,

$$N_\gamma = -\frac{N_{\text{cells}}}{\text{PDE}} \log\left(1 - \frac{N_{\text{fired}}}{N_{\text{cells}}}\right) , \tag{3.11}$$

gives the expected number of incident photons corresponding to a number of hit microcells, and will be useful in later discussion.

The probabilistic (binomial) and exponential models are compared in Figure 3.8 – the maximum percent difference in the model predictions is 1.1% for a 25-microcell SiPM, so the exponential model predicts saturation with high accuracy, assuming a random distribution of photons into hit microcells.

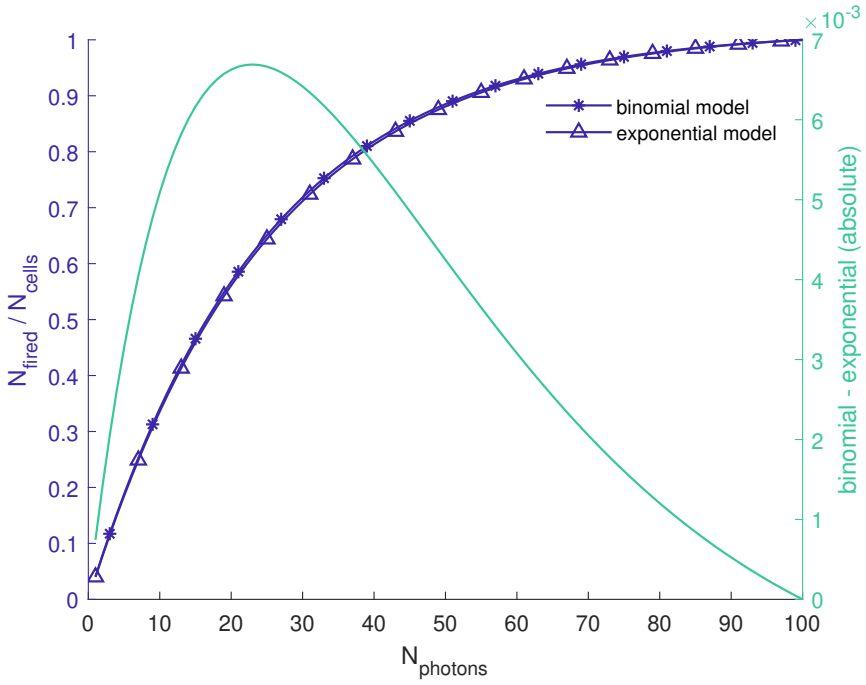

Figure 3.8: Comparison of binomial model (Equation 3.9) and exponential model (Equation 3.10) for fraction of fired microcells in a SiPM consisting of 25 microcells total.

Susceptibility of SiPMs to so-called "oversaturation" effects [60] may be a result of a number of causes, including septal multiplication in interstitial space between microcells, but is a much smaller concern in the newest generation of devices, as they may consist of many thousand microcells (see references in Table 2.2).

Saturation effects are immediately evident in naïvely reconstructed images from the proposed array, which here means images reconstructed in the manner described to this point, and without making corrections following reconstruction. Following from the preceding discussion, a reconstruction of the front view of the wrench attachment (from Fig-

ure 3.1) is shown in Figure 3.9.

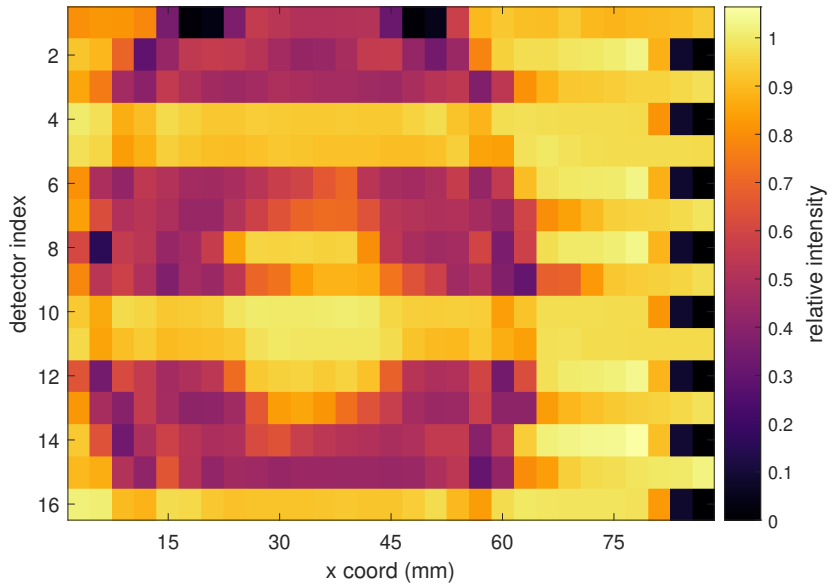

Figure 3.9: Front view of 1 7/8" socket wrench attachment. The difference in saturation between the LYSO channels at indices 4, 5, 10, 11, and 16 and the quartz channels at the remaining detector indices is clearly visible. The object features can be made out, but the contrast is significantly lower for near-saturated detectors. Even-channel pixels at right appear black because these channels belong to the second row of detectors, and so time tags associated with events which would be detected here are corrected such that the earliest events occur several mm from the image margin.

The object's features are clearly discernible in this image, though some are obfuscated by near-saturation of the scintillator detector channels. Because of the large efficiency difference between LYSO and quartz, as well as the intrinsic background which is absent in Cerenkov radiators, many more microcells are fired in the scintillator photocouple, and the differential device response for a step in number of incident photons is much smaller at higher photon numbers, as shown in Figure 3.8. Consequently, though the per-pixel uncertainty associated with the LYSO-measured horizontal object profiles is lower, the contrast between bright field and object regions in the image is also lowered.

In order to correct for this effect, a calibration method was developed to match the signal level detected in the quartz radiators to the signal level detected in the LYSO scintillators. To create a data basis for the calibration, several material blocks were placed in the beam

and reconstructed as described above. A list of materials, as well as relevant physical properties, is given in Table 3.2. These naïve reconstructions of material blocks were used to calibrate the response from each detector type to the expected signal level, given by the 1D Beer-Lambert law (Equation 3.7).

Table 3.2: Material blocks used in cross-calibration of array elements, and selected physical properties

material	thickness (mm)	μ/ρ (cm^2/g)	ρ (g/cm^3)
Fe	25.4	0.04265	7.874
Al	25.4	0.04324	2.70
LDPE	25.4	0.05064	0.940
Cu	25.4	0.04205	8.96
Pb	22	0.04607	11.34

The basis images for calibration are shown in Figure 3.10, with (as expected) saturation through each material block in the LYSO detector channels. The corresponding profiles across the horizontal direction of travel are shown in Figure 3.11. The calibration curve for each SiPM-photoconverter couple is determined individually, to include the difference in each due to manufacturing tolerance, light transport, and geometry (though the geometry effect is small).

The process for cross-calibration is as follows: first, the material block image is reconstructed without correction. A region of interest corresponding to the image region within the material block is selected, and the intensity profile is mapped. Regions of interest are selected for each of the materials on the basis of the horizontal profiles. The regions selected are common to all detectors, rather than being selected individually per channel, as perceptual mapping of the data to a user-readable image is the goal. The intensity values within each region are averaged and tabulated, along with the theoretical attenuation values from the Beer-Lambert law. The intensity values are fit iteratively by the nonlinear

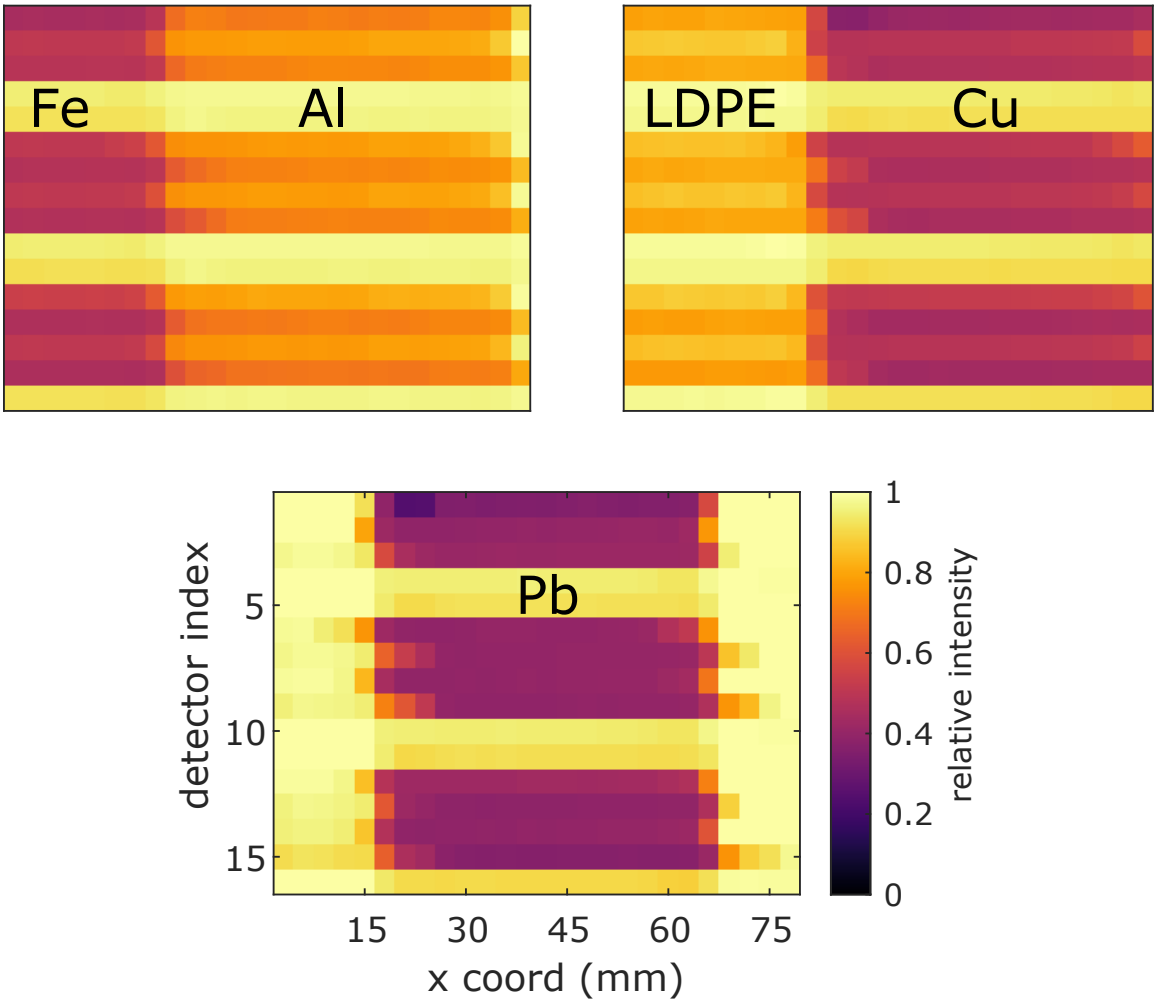

Figure 3.10: Material images forming basis for cross-calibration of array channel responses; Top left: iron and aluminum blocks abutting in a reconstructed image; Top right: LDPE and copper blocks abutting; Bottom: lead block centered on a bright field.

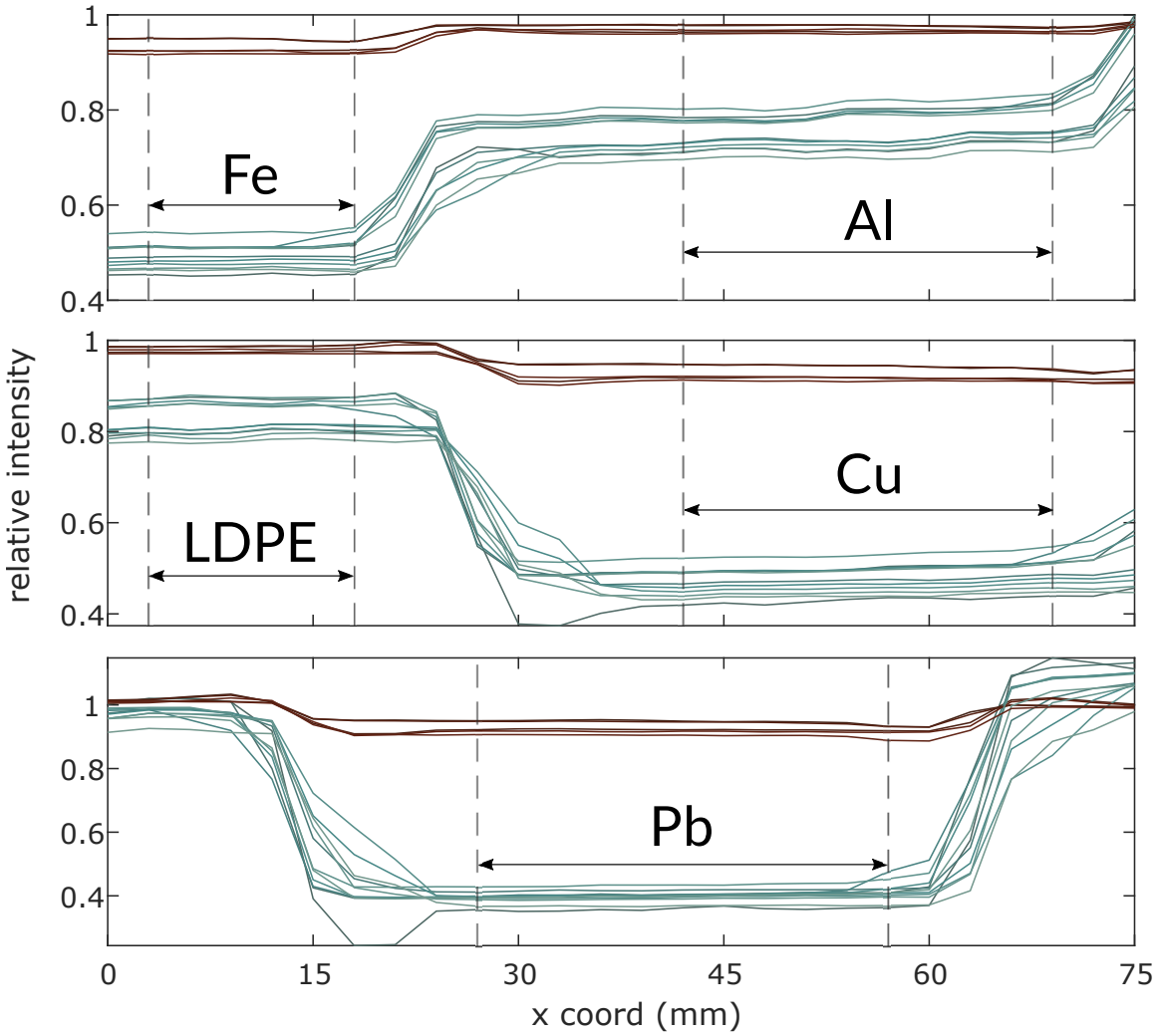

Figure 3.11: Profiles across material images as basis for response matching. Cerenkov channel profiles are shown in shades of blue, and form the lower band of 11 profiles, while the upper band of profiles with less contrast correspond to LYSO response. Regions of interest for each block are indicated.

least-squares method to the theoretical values, according to the fit equation

$$\left(\frac{I}{I_0}\right)_{\text{theoretical}} = a \cdot \log\left(\left(1 - b \cdot \left(\frac{I}{I_0}\right)_{\text{image}}\right)^2\right) + c\,, \tag{3.12}$$

by analogy to Equation 3.11. The argument of the natural logarithm is squared to ensure positivity. The fit parameters are a, b, and c. An upper bound of 0 is set for a, so that concavity is preserved, and an upper bound of 1 is set for b, to ensure that the asymptote corresponding to total saturation satisfies

$$\frac{1}{b} > \left(\left(\frac{I}{I_0}\right)_{\text{image}} = 1\right)\,,$$

and does not occur within the dynamic range of the image intensity. The free parameter c is included particularly to match nonzero channel background image intensities to the expected intensity of zero – thus, a properly calibrated background image will have zero intensity, rather than including (for example) the self-counts from the natural radiation of LYSO.

The cross-calibration curves for two of the detector channels are shown in Figure 3.13, from the materials in Table 3.2, with two additional calibration points: the flat-field intensity and background intensity. For all channels, the point (1,1) was included to match flat-field intensity, while the background calibration point $((I/I_0)_{\text{background}}, 0)$ was calculated per-channel. As a result, the background subtraction is removed from Equation 3.6. The fit coefficients and goodness-of-fit measures of adjusted R-squared R^2_{adj} and root mean square error (RMSE) are reported for all channels' calibration curves in Table 3.3. Fit residual distributions are shown in Figure 3.12.

Following calibration, reconstructed intensities are thresholded such that no pixel values are negative, a simple nonlinear operation, based on the knowledge that negative linear attenuation coefficients are not present in the physical object.

Table 3.3: Fit parameters, and goodness of fit

channel	type	a	b	c	R^2_{adj}	RMSE
1	C	-3.330	0.145	-0.008	0.9769	0.0538
2	C	-0.668	0.509	0.008	0.9718	0.0594
3	C	-0.755	0.498	-0.011	0.9876	0.0395
4	L	-0.091	0.998	-0.088	0.8916	0.1165
5	L	-0.108	0.995	-0.113	0.9372	0.0887
6	C	-0.727	0.476	-0.003	0.9671	0.0642
7	C	-0.698	0.516	-0.001	0.9915	0.0326
8	C	-0.619	0.536	0.007	0.9719	0.0593
9	C	-0.699	0.500	0.004	0.9764	0.0543
10	L	-0.092	0.998	-0.093	0.9119	0.1051
11	L	-0.109	0.995	-0.106	0.9420	0.0853
12	C	-0.477	0.632	0.006	0.9730	0.0581
13	C	-0.960	0.418	-0.009	0.9885	0.0380
14	C	-0.571	0.563	0.007	0.9735	0.0576
15	C	-0.706	0.511	0.000	0.9931	0.0293
16	L	-0.102	0.996	-0.091	0.9541	0.0758

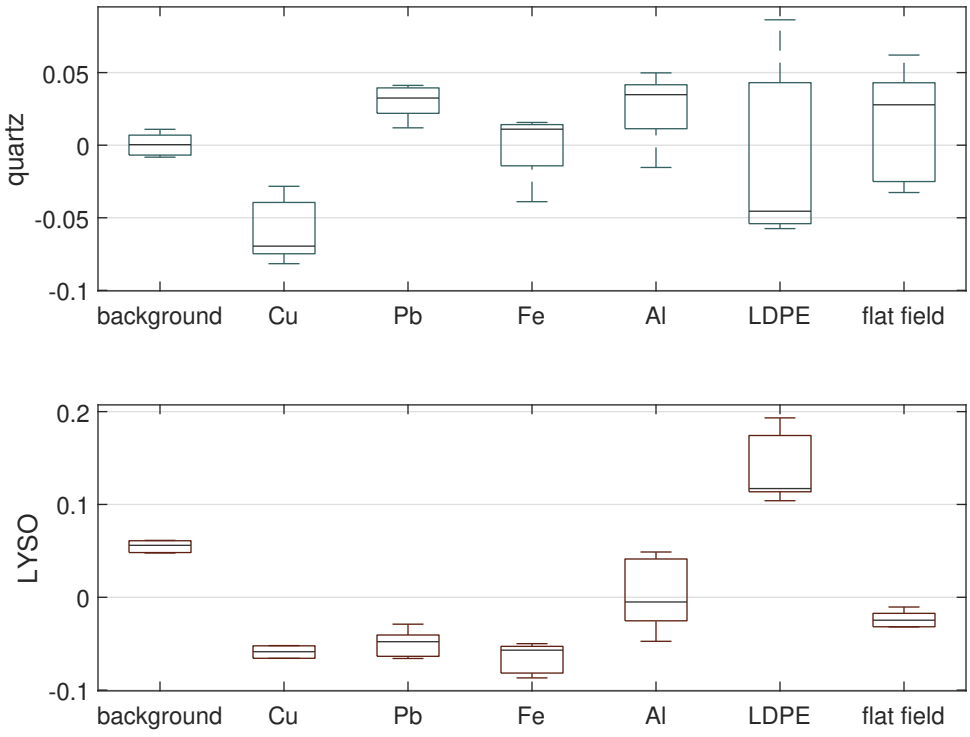

Figure 3.12: Box-and-whisker plot of residuals for calibration curve fits.

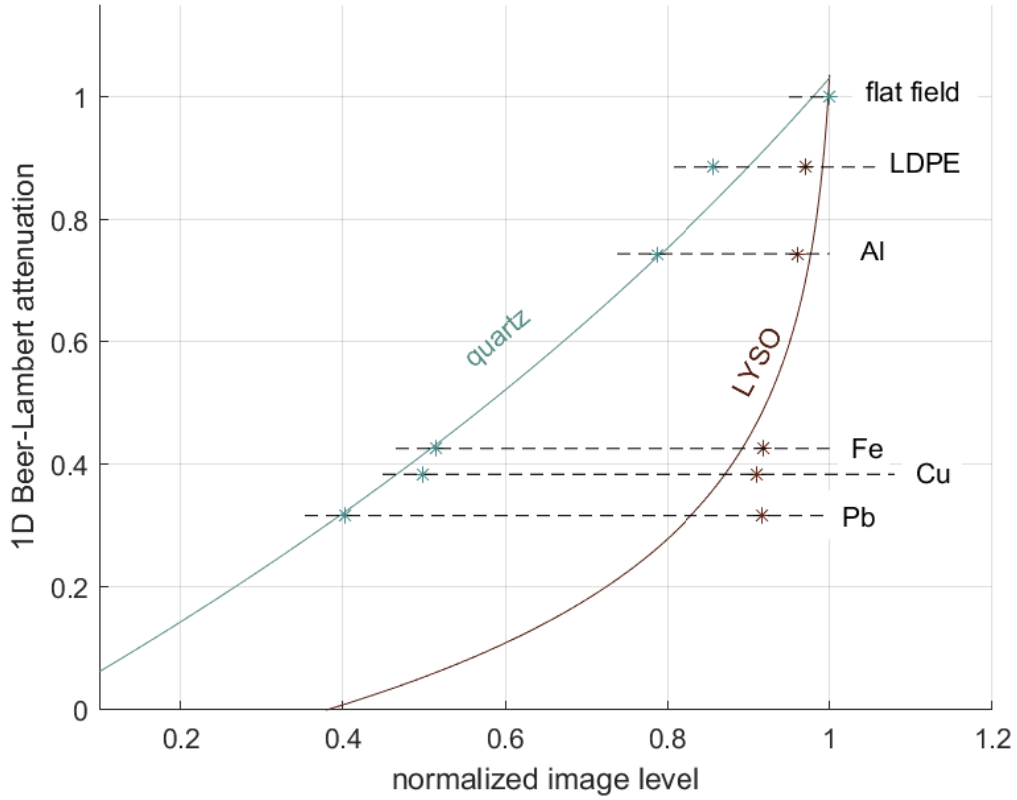

Figure 3.13: Calibration of detector channels 6 (quartz) and 11 (LYSO), via intensity matching to the Beer-Lambert predicted signal levels. Fit is of the form given in Equation 3.12.

3.4 Redundant sampling for resolution reduction

A final modification to the image before output is correction of image oversampling to improve resolution beyond the limit of the detector element size. In the application of interest, the spatial resolution in the vertical coordinate may be improved (that is, reduced), by the redundancy in sampling which is present due to the array design. One of the goals in design of this imaging system was enabling of imaging with resolution of 5 mm, thus the horizontal trajectories of each of the detector elements across a virtual pixel array of that vertical resolution have redundant covering by the 6 mm silicon photomultiplier *detector* elements. Except for the end detectors, each element's trajectory is covered in the vertical direction by a 0.5 mm extension of the trajectory of the detector below, as shown in Figure 2.9.

The effect of redundant sampling can be understood by analogy to the linear document scanner: suppose one was to be built with 1 µm resolution in the longitudinal axis, but that the smallest available charge-coupled device (CCD) elements are 4 µm in length. One method, then, for enabling the desired resolution is simply using a single CCD, and scanning a row latitudinally with a common centerline for the detector element and the pixel row, then stepping by 1 µm in the longitudinal direction and scanning latitudinally, until the entire image space is covered. Each row in the output image corresponds to a single horizontal scan.

However, a disadvantageous consequence of scanning this way is that each horizontal object row is oversampled, and may contribute to several horizontal rows in the image in linear combination. This leads to smearing in the vertical direction – Figure 3.15a shows an image, and Figure 3.15b shows the same image resampled as described above, with a 4:1 ratio between linear detector dimension and linear pixel dimension, wherein the blurring is evident.

For a single column scanned in this way, the "covering" matrix may be calculated, which describes the resampling, and will permit reconstruction of the blurred image. It is

assumed that the number of detector horizontal scans is equivalent to the number of horizontal pixel rows in the image, such that $m = n$ and $\mathbf{C}_{m,n}$ is square. The covering matrix $\mathbf{C}_{m,m}$ then contains the normalized fractional linear coverings of each object pixel in the column by each detector in the longitudinal direction, which is the direction of oversampling. Each of the matrix coefficients is given by

$$\mathbf{C}_{i,j} = \frac{l_d(i,j)}{h_{px} \cdot \sum_n l_d(i,j)}\,, \tag{3.13}$$

where $l_d(i,j)$ gives the total linear covering distance of detector i over pixel j, and h_{px} is the pixel dimension in the longitudinal direction (i.e. the height). $\mathbf{C}_{m,m}$ is defined such that the total weight of each of the object space samples contributing to a single pixel is unity, and that the element $\mathbf{C}_{i,j}$ is the relative response of the ith detector to the jth pixel contribution. This approach is valid for rectangular detectors and pixels, and is used as an approximation to the case of the proposed linear imaging array, as the same approximation is made in the horizontal count binning.

A simple algorithm for computing coefficients of the matrix $\mathbf{C}_{m,m}$ is given in Algorithm 1. It assumes that detector (position) 1 and pixel 1 have the same vertical centerline coordinate, as do detector 2 and pixel 2, and so on. Required inputs to the function are h_{px}, h_d, and N_{px}, which represent the pixel height, detector height at image plane, and number of pixels in the output image, respectively.

In Algorithm 1, the operator $A +\!\!+ B$ denotes concatenation of the arguments A and B, the operator rem$[A, B]$ returns the remainder of scalar division of A by B, N$[\cdot]$ returns the number of elements of its argument, $\mathbf{1}[A, B]$ returns an $A \times B$ matrix where all elements are 1, and $\mathbf{0}$ is similarly defined for zero matrices. The element of $\mathbf{C}_{m,m}$ in the ith row and jth column is given by $C_{i,j}$, as usual, while $\mathbf{C}_{i:p,j:q}$ returns the submatrix from rows i through p and columns j through q. As in Line 15, $\mathbf{C}_{i,:}$ returns the entire ith row of matrix $\mathbf{C}$, while similarly $\mathbf{C}_{:,j}$ returns the jth column.

Algorithm 1 Determine $\mathbf{C}_{m,m}$ matrix coefficients

Require: h_{px}, h_d, N_{px}

if $h_{px} < h_d$ **then**

quit : oversampling condition not satisfied

end if

$N_{UC} \Leftarrow 2 \cdot \lfloor (h_d - h_{px})/(2 \cdot h_{px}) \rfloor + 1$

$\alpha = \text{rem}[(h_d - h_{px})/2, h_{px}]$

$E_d = \langle \alpha \rangle +\!\!+ \mathbf{1}[N_{UC}, 1] +\!\!+ \langle \alpha \rangle$

$N_{pad} = \lfloor \mathbf{N}[E_d]/2 \rfloor$

$D_c = 2 \cdot N_{pad} + N_{px}$

$\mathbf{C} = \mathbf{0}[D_c, D_c]$

for all $\{i \in \mathbb{N} \mid 1 + N_{pad} \leq n \leq D_c - N_{pad}\}$ **do**

$\mathbf{C}_{i,(i-N_{pad}):(i+N_{pad})} \Leftarrow E_d$

end for

$\mathbf{C} \Leftarrow \mathbf{C}_{(1+N_{pad}):(D_c-N_{pad}),(1+N_{pad}):(D_c-N_{pad})}$

for all $\{i \in \mathbb{N} \mid 1 \leq i \leq m\}$ **do**

$\mathbf{C}_{i,:} \Leftarrow \mathbf{C}_{i,:}/(\sum_i \mathbf{C}_{i,:})$

end for

The resampled output, $f_{m,n}$, of an object $x_{m,n}$ is given by

$$\mathbf{C}_{m,m} \cdot x_{m,n} = f_{m,n}\,. \tag{3.14}$$

Recovery of x from f is therefore an inverse problem. Fortunately, $\mathbf{C}$ is full-rank for small detector:pixel ratios, as in the detector geometry in this work, and is even full-rank for some large ratios (see Figure 3.14). If the covering matrix is invertible, the reconstruction problem is solved by matrix inversion. If it is not, we seek the minimum-norm least squares solution to the system of equations in Equation 3.14, say, by QR decomposition [61]. An image and its reconstruction (via the minimum-norm least squares method) from its blurry resampled representation are shown in Figure 3.15.

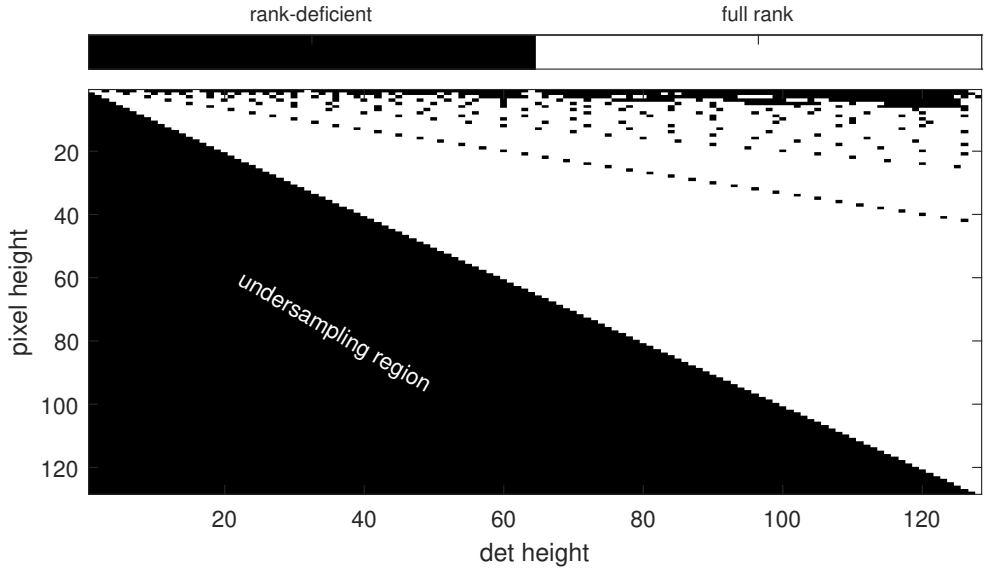

Figure 3.14: Rank of detector-column covering matrix $\mathbf{C}_{m,m}$, constructed for various integer detector and pixel heights according to Algorithm 1, at an image column height of 128 pixels.

Note that as long as this reconstruction is computed following the calibration correction, efficiency is already accounted for. The correction should be applied at the *image* plane rather than the *detector* plane. For the proposed array, oversampling with 6 mm detectors with 1 mm covering at the detector plane permits sampling of pixels 2.4 mm in height at

(a) Original (b) Resampled (c) Reconstructed

Figure 3.15: Reconstruction of oversampled image. Left: A 64×64 image; Center: The same image resampled by a 4×1 "detector"; Right: A reconstruction of the blurry center image, showing that min-norm least squares reconstruction from an oversampled image may be used to improve resolution beyond the detector limit.

the SOD:SID ratio of $2.2 : 4.6$.

Finally, the image is renormalized according to its maximum:

$$f = f/\max[f]\,. \tag{3.15}$$

A pair of calibrated images of the socket attachment test object are shown in Figure 3.16. The center image has the row weighting schema described above applied, while the top image is only calibrated.

Comparing the calibrated images in Figure 3.16 to the uncalibrated one shown in Figure 3.9, the relevant image features are more readily apparent: the bright striping across the image due to near-saturation of the LYSO channels is nearly absent. Some less obvious striping is visible in the scintillator rows on the right hand side of the images, a result of inaccurate calibration for the pixel values present there. This effect is most obvious at the object's center, in the bright patch, in which several very intense pixels are located – the large intensity values present here are due to the steep gradient of the calibration curve as measured flux ratios approach unity, causing small variations in the measured flux to have much higher relative effect on the image than that for smaller measured flux ratios.

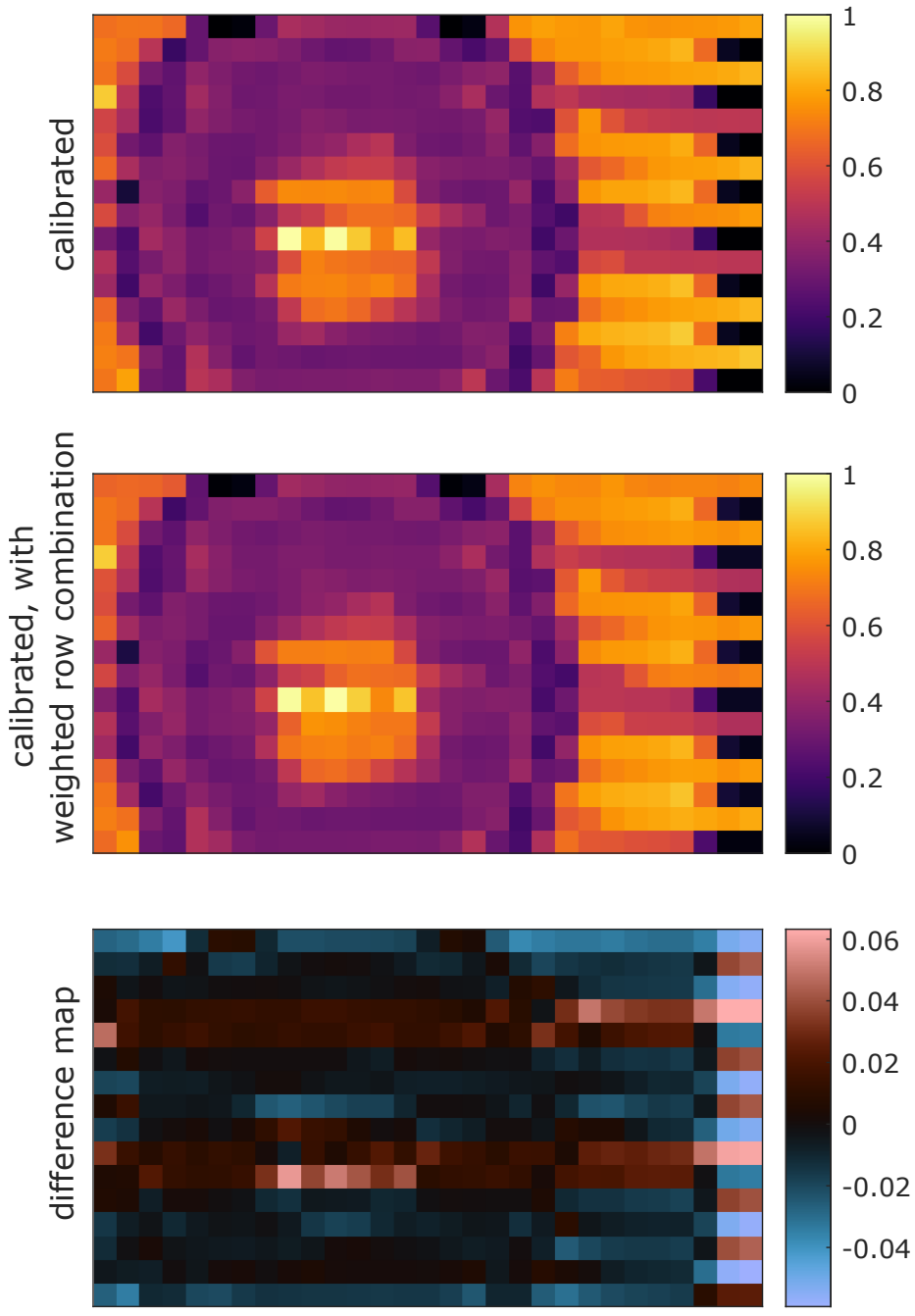

Figure 3.16: Effects of calibration and area-weighted row corrections. Top: object image with profiles corrected by calibration; Middle: calibrated image corrected by intersection area-weighted linear row combination; Bottom: difference map between images (middle minus top).

The calibrated image may appear perceptually very similar to the calibrated image corrected by linear combination of rows. The difference map between the images (displayed as middle minus top) reveals the actual effect of the correction. Most noticeable are the nearly all-positive bands for the center LYSO channels. Thus the linear combination of rows "softens" the particularly discontinuous portions of the image, after renormalization. The object edges are clearly visible in the difference image, as expected. The row-wise correction is implemented specifically to alleviate feature stacking, which distorts the object profile in the vertical direction. The object edge profile which is visible is present as the image edges are more accurately matched to the actual edge profile of the object.

3.5 Reconstruction pseudocode

With the above equations and considerations in mind, a pseudocode for the image reconstruction algorithm may be written down, and is given in Algorithm 2.

The operators $\lfloor \cdot \rfloor$ and $\lceil \cdot \rceil$ represent the floor and ceil functions, as before. $E[t]$ returns the energy of the event at time tag t. rownum$[\cdot]$ returns the detector row (either 0 or 1) of the argument, such that the time of acquisition is translated correctly. The matrix $\mathbf{C}$ may be obtained from Algorithm 1.

All images showcased in this work are outputs of the algorithm as coded in Matlab R2020a. The entire code takes about 0.88 s after data loading is complete to parse through a dataset containing 1.65×10^6 time-tagged counts, on an Intel i5-6500 desktop computer at 3.20 GHz. However, this pseudocode is platform-independent, and as such should not be implemented explicitly as stated. For instance, preallocation of memory for the image should be performed in almost all programming languages, such that its size does not change on each loop iteration, but the preallocation step is not written as a line in the pseudocode. Special care should be taken of data types – in Line 13, d_{edges} is defined as an ordered set, rather than a numeric array, as it is intended to consist of unique values, and in some implementations may need to be checked at generation for these. The statement

Algorithm 2 Build image from list mode radiation data

init: $T_c \Leftarrow t_1, t_2, \ldots, t_x$: list of time tags of events for detector channels c
init: $w_{px}, w_d, v, p, B_c, t_B, E_{bounds,c}$
  $n_{px} \Leftarrow \lceil (t_x \cdot v - (2w_d + p))/w_{px} \rceil$
  $\kappa \Leftarrow n_{px} * w_{px}/2$
  $px_{edges} \Leftarrow \{-\kappa, -\kappa + 1w_{px}, -\kappa + 2w_{px}, \ldots, \kappa - 2w_{px}, \kappa - 1w_{px}, \kappa\}$
for all $c \in$ detector channels **do**
  for all $t_i \in T_c$ **do**
    if $\neg(E[t_i] \in E_{bounds,c})$ **then**
      continue for
    end if
    $d_l \Leftarrow (t_x - t_i) \cdot v - p \cdot (1 - \text{rownum}[c])$
    $d_r \Leftarrow d_l + w_d$
    $d_{edges} \Leftarrow d_l \cup \{d_l < px_{edges} < d_r\} \cup d_r$
    for $n = 2$ to $\text{N}[d_{edges}]$ **do**
      $\gamma \Leftarrow d_{edges}(n) - d_{edges}(n-1)$
      $i \Leftarrow 1 + \left\lfloor (\frac{1}{2}(d_{edges}(n-1) + d_{edges}(n)) - px_{edges}(1))/w_p \right\rfloor$
      if $\neg(0 < i < \text{N}[px_{edges}])$ **then**
        continue for
      end if
      $f_{c,i} = f_{c,i} + (\gamma/w_d) \cdot E[t_i]$
    end for
  end for
  $f_{c,:} \Leftarrow$ apply calibration$[f_{c,:}/((w_{px}/v) \cdot (B_c/t_B))]$
  $\{f_{c,:} \mid f_{c,:} < 0\} \Leftarrow 0$
end for
$f \Leftarrow \text{solve}[\mathbf{C}x = f, x]$
$f \Leftarrow f/\max[f]$

"**continue for**" here means "immediately pass control to the next iteration of the **for** loop containing the continue statement."

The first value which must be provided to the algorithm is w_{px}, the width of a single pixel in the reconstructed image, which need not actually equal the backprojected width of a *detector* at the object plane (w_d), as long as the position of the object at some timestamp is known with according precision. For example, if the translation velocity is 4 mm/s, the timing resolution of the detector should be at most 1 s if horizontal spatial resolution of 4 mm is required. p as a standalone variable represents the detector pitch in the direction of motion.

The translation velocity v must also be provided, as it is assumed in this approach that the position of the object with respect to the detector array is directly proportional in time to this (constant) velocity, as implemented in Line 11 of Algorithm 2. If the margin of the detector is some other function of the event's time tag, or if it is known precisely at the given time tag via some alternative verification system – say, via optical or laser position telemetry – the necessary corrections may be made to this line and Line 3.

n_{px} is the number of pixels in the final image. In order for complete data to be gathered for a line impulse, the minimum travel distance is $2w_d + p$, that is, there must be transit across the width of both rows of detectors and the space corresponding to the lateral pitch between them. Accordingly, any object of non-infinitesimal length must transit at least the difference of this distance and its own extent in the direction of translation in order to be reconstructed. If it is assumed that the entire object is scanned in a time t_x, then the field of view of the system for that scan time is given by $t_x \cdot v - (2w_d + p)$.

$E_{bounds,c}$ is the set of ADC bounds corresponding to each detector. B_c and t_B represent the ADC-thresholded background and time of acquisition of that background, for all channels c, respectively. These data are necessary to ensure the image is quantitatively normalized correctly.

CHAPTER 4

IMAGING PERFORMANCE

The primary tests used for system quality characterization are based on those outlined in the ANSI standard N42.46-2008 [12], which outlines standard tests for penetration, spatial resolution, contrast sensitivity, and wire detection.

4.1 Wire detection

The wire detection test object was constructed from seven different diameters of bare copper wire, from American wire gauge (AWG) ranging from 10 to 24. Corresponding diameters and maximum attenuation through a distance equal to the diameter are shown in Table 4.1. Images of the constructed test object are shown in Figure 4.1.

Table 4.1: Diameters of wires used in American National Standards Institute (ANSI) wire detection test

AWG	diameter (mm)	max attenuation (I/I_0)
10	2.588	0.9071
12	2.053	0.9256
14	1.628	0.9405
16	1.291	0.9525
18	1.024	0.9622
20	0.812	0.9699
24	0.511	0.9809

Image sensitivity results for the largest three wire sizes are shown in Figure 4.2.

In the wire sensitivity test, it is evident that the 10 gauge wire is present in the image. There are slight truncation errors in the end pixels, which are readily visible in the 10 gauge image. The 12 gauge wire is more difficult to detect, at less than half the diameter of the 10 gauge wire, but the sinusoidal profile can still be made out, even through the dark banding in the LYSO profiles. The dark streaks in the lowest profiles are due to

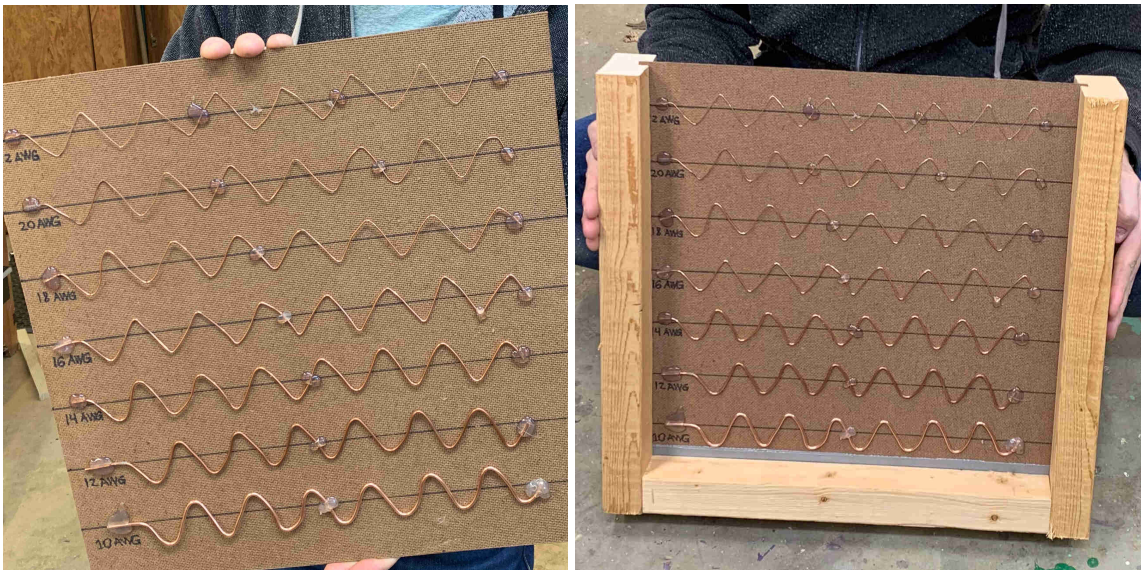

(a) Wire detection test object. (b) Wire detection test object in imaging frame.

Figure 4.1: Images of wire detection test object, consisting of bare copper wire of varying gauge. Note: 24 gauge wire is mislabeled in images as 22 gauge.

the method in which calibration was performed: material blocks were placed directly on the translation stage, and so the bottom few channel image levels before calibration were artificially low. Underestimation of the transmission ratio naturally follows in the post-calibrated images. For the 14 gauge wire object, the profile is probably not discernible for any viewing window. It should be noted here that the intensity ratio clearly drops regardless of object presence from right to left (or, as acquisition time increased). A time-dependent brightfield could be measured provided that precise timing information from the linac was available, say, from machine log files, but in this work the effect is left uncorrected.

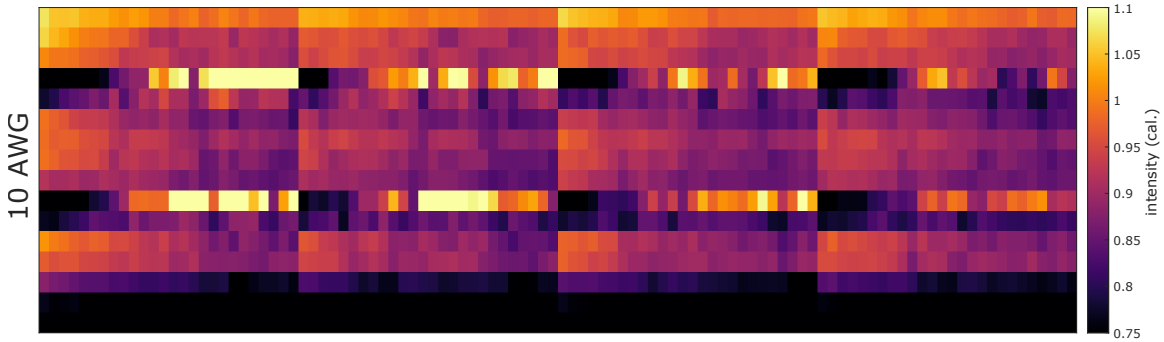

(a) Wire sensitivity test, 10 AWG wire.

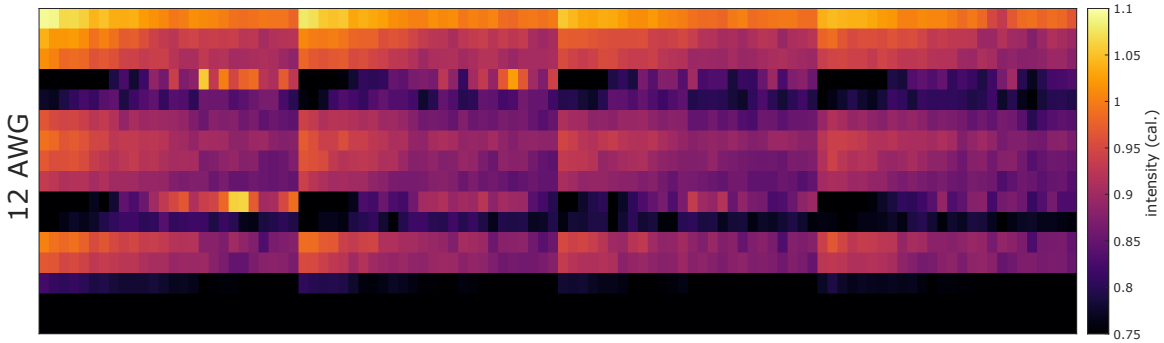

(b) Wire sensitivity test, 12 AWG wire.

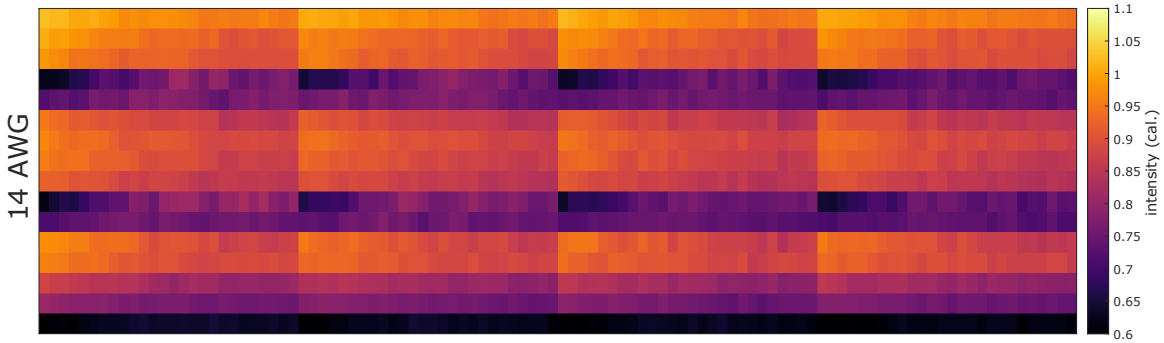

(c) Wire sensitivity test, 14 AWG wire.

Figure 4.2: ANSI N42.46-2008 wire sensitivity test results, for three thickest wires in object. All images are calibrated using the method described above. Bright patches in LYSO channels are due to large differential in calibrated image level with respect to microcell response (see Figure 3.13). Images are rewindowed to facilitate ease of reading, see color bars at right.

4.2 Spatial resolution

ANSI N42.46-2008 specifies the spatial resolution test object as follows: “The spatial resolution test object is a steel line-pair gauge; either one with three slots in a steel plate... or one with three square steel rods on a base. In each test object, the three features (slots or rods) are of width “d”, are separated by the same distance “d” and are 10 cm long; the thickness of each gauge also is “d.” The line-pair gauges shall be constructed of carbon steel...” [12]. For ease of construction and material access, several line-pair gauges were instead constructed of smooth-shank common or finishing nails, mounted in cardboard bases.

Table 4.2 details characteristics of objects used in this section. A visual image of the objects with bases is shown in Figure 4.3. All reconstructed images in this section use a horizontal pixel dimension of 0.5 mm at the image plane, and nominal vertical pixel dimension, 2.4 mm, determined by backprojection of the detector limiting space and corrections as described in section 3.4.

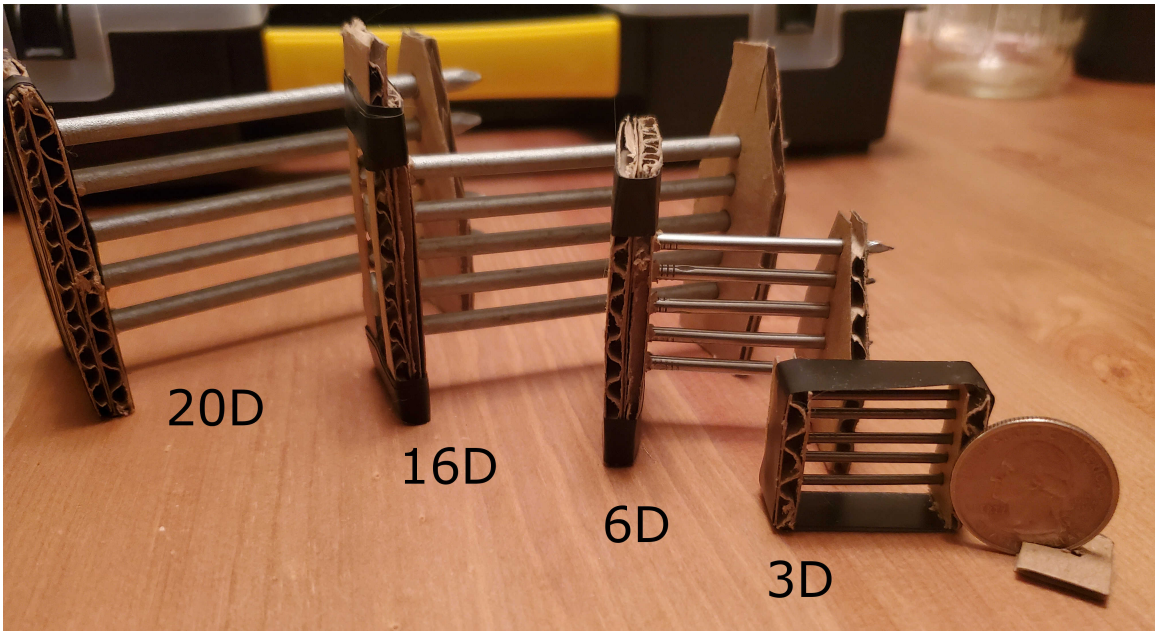

Figure 4.3: Spatial resolution objects produced for ANSI-like imaging test.

A particular image processing issue is mentioned for the case of the vertical spatial resolution test. In several images presented to this point (for example, Figure 3.16), there is

Table 4.2: Diameters of objects used in spatial resolution test

nail size	length (cm)	diameter (mm)	max attenuation (I/I_0)	finish
3D	3.18	1.87	0.9391	bright
6D	5.08	2.90	0.9072	bright
16D	8.89	4.14	0.8702	galvanized
20D	10.2	4.97	0.8463	galvanized

a horizontal image striping effect present, which arises due to a combination of two factors. First, the linear accelerator at turn-on apparently has a higher output power spectrum, which degrades very slightly during acquisition – this effect is independent of stage motion. Second, because of the spatial adjustment of detected counts into the pixel bins, the first several horizontal pixels in each acquisition associated with detectors in the second of the vertical rows are assigned zero counts. Thus, the maximum brightfield intensity which occurs due to power degradation at the lateral image edge is displaced by a distance equivalent to the backprojection of the lateral detector pitch at the image plane. This is illustrated in Figure 4.4.

To mitigate the time-dependent energy degradation effect, the ideal method would be to obtain accurate time-dependent bright-field intensity for each detector and apply a time-dependent normalization in Equation 3.6. This approach was not implemented in this work due to the complex acquisition schema, wherein ideally the linac, translation system, and DAQ are all initiated concurrently. However, triggering the DAQ on the basis of linac pulse and simultaneously beginning motion is a multi-framework software problem which is not discussed in detail here. Further, the effect is small in almost all other cases, and as such image corrections are only applied for the vertical spatial resolution test.

The correction applied in an ad hoc manner for the vertical spatial resolution images is as follows:

$$f_{i,:} \Leftarrow f_{i,:} \cdot \left(\frac{\text{mean}\left[\text{mean}\left[f_{i-1,:}\right] + \text{mean}\left[f_{i+1,:}\right]\right]}{\text{mean}\left[f_{i,:}\right]} \right) \forall \,\text{even}\; i\,, \tag{4.1}$$

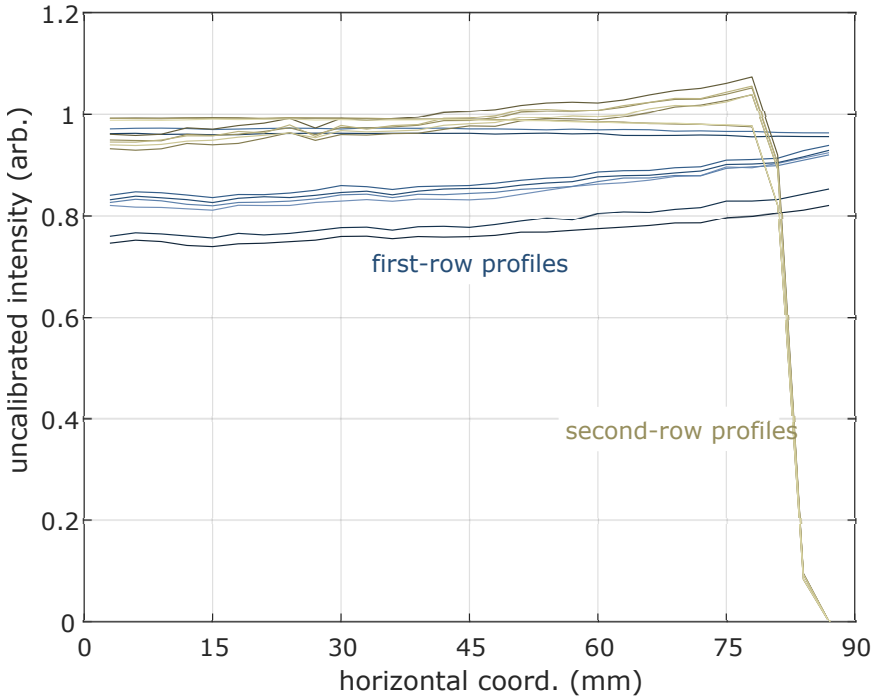

Figure 4.4: Time-dependent bright-field profiles, with no object present. Profiles are uncalibrated, and degradation of intensity over the course of the 100-second acquisition is clearly visible.

where mean$[\cdot]$ is the average of all elements in the vector argument. This correction corrects the means of the even rows to a linear interpolation on the adjacent row means, which should approximately match the intensity profiles. It is applied *after* clipping the lateral image end containing the zero- and near-zero-intensity pixels. Even applying this correction, however, the horizontal striping is present (see Figure 4.5).

Vertical profiles through a column near the center of the images are shown in Figure 4.6.

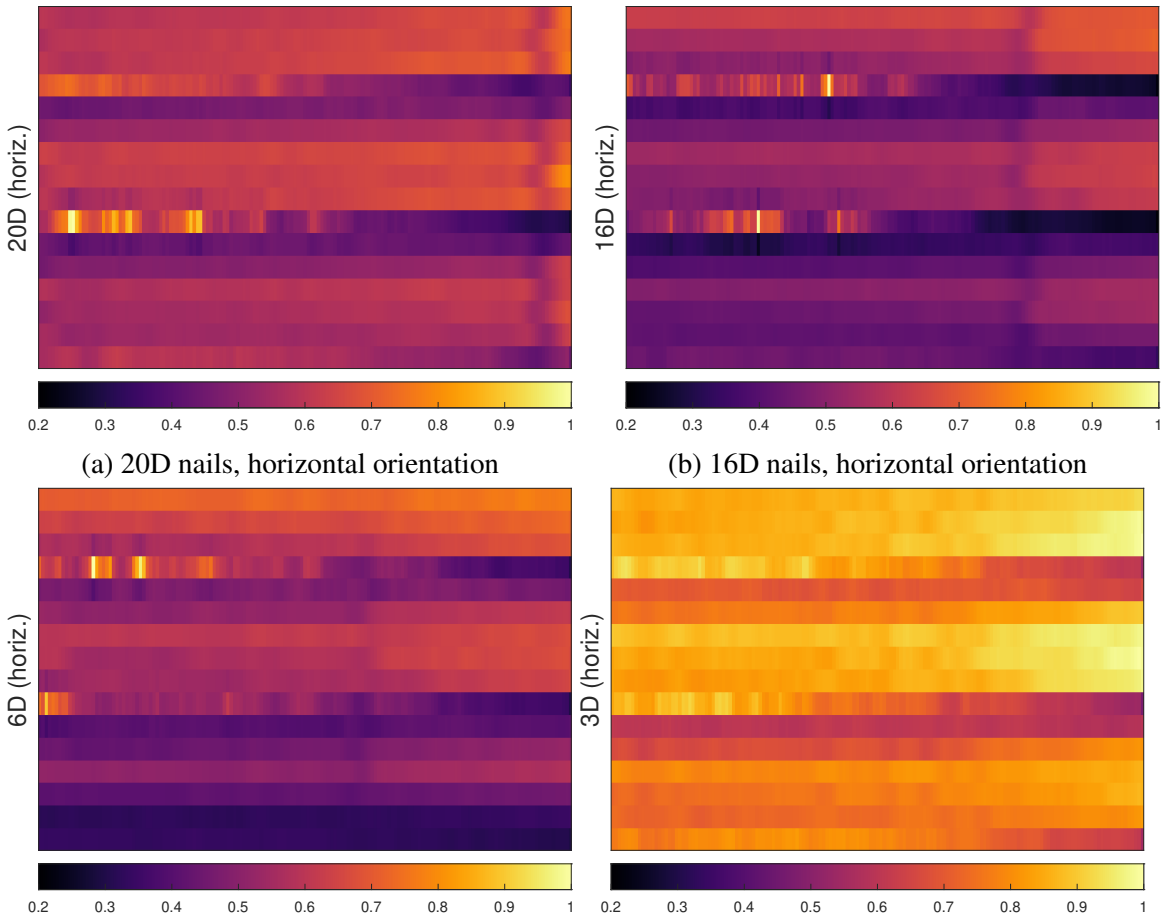

(a) 20D nails, horizontal orientation

(b) 16D nails, horizontal orientation

(c) 6D nails, horizontal orientation

(d) 3D nails, horizontal orientation

Figure 4.5: Vertical spatial resolution test result images. Locations of the heads of the nails are evident, but the vertical spatial resolution is obscured by the striping still present even after interpolated-mean averaging.

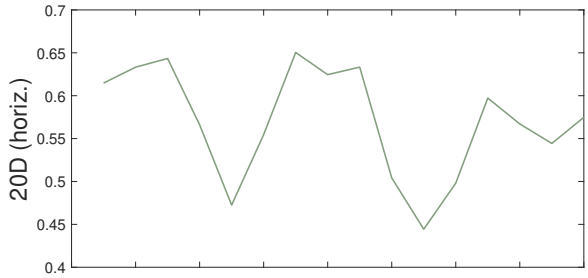

(a) 20D nails, vertical spatial profiles

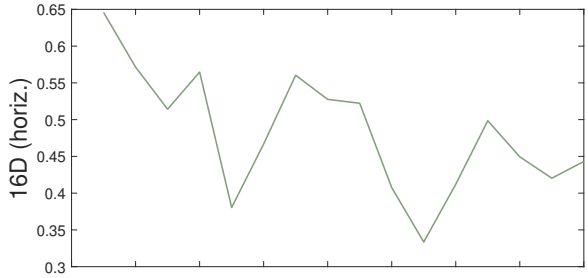

(b) 16D nails, vertical spatial profiles

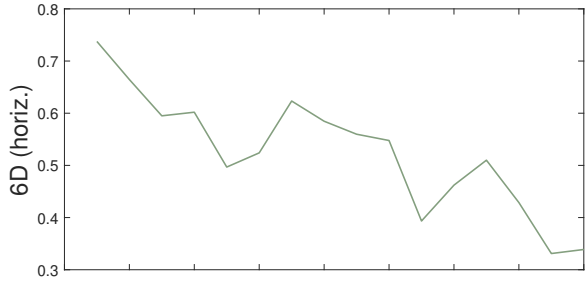

(c) 6D nails, vertical spatial profiles

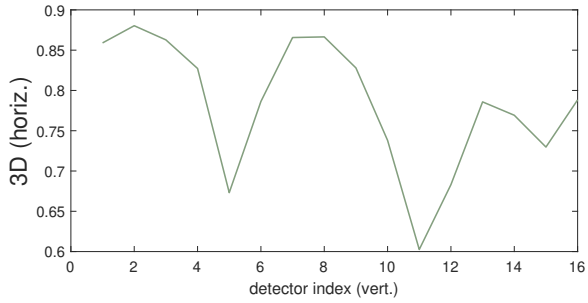

(d) 3D nails, vertical spatial profiles

Figure 4.6: Vertical spatial resolution image profiles, corresponding to images in Figure 4.5, through the centers of those images. Correspondence to test objects is indiscernible.

In the case of the horizontal spatial resolution test, no such ersatz correction method is applied, yet the imaged objects are much easier to discern. Results are shown in Figure 4.7 and Figure 4.8.

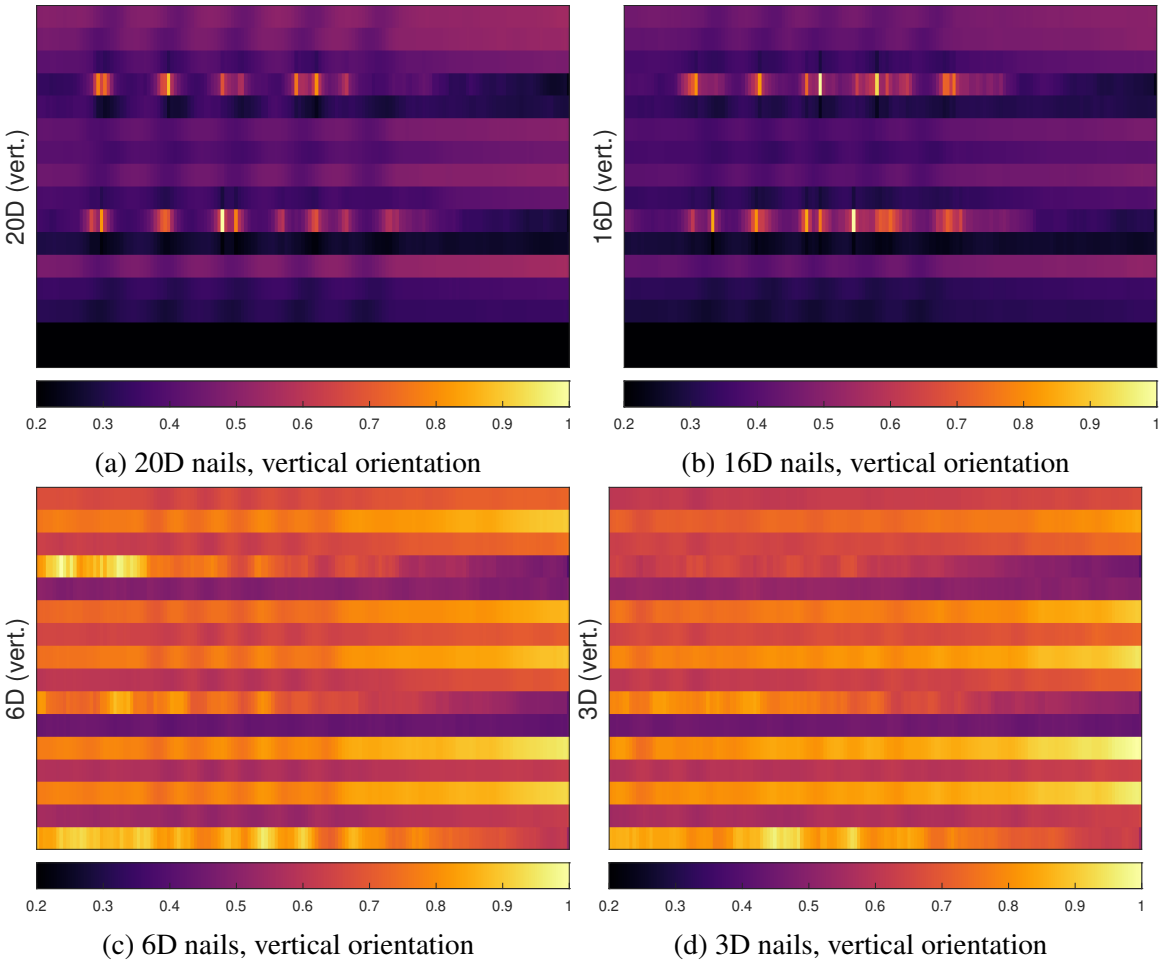

(a) 20D nails, vertical orientation

(b) 16D nails, vertical orientation

(c) 6D nails, vertical orientation

(d) 3D nails, vertical orientation

Figure 4.7: Horizontal spatial resolution test result images. The line pair gauges are easy to discern for the thicker gauges, and are only not detectable for the smallest test objects imaged.

The horizontal spatial resolution test results show very good capability for distinguishing line pairs. The gauges may be easily visually separated for the two largest diameters, and may even be selected out by a careful observer in the case of the 6D test object. Examination of the line profiles through a single quartz and LYSO element confirms these results – in the case of the 20D gauge, the quartz profile returns to baseline (though it is nonuniform) between pairs, as does the LYSO profile, or nearly so. For the 16D gauge,

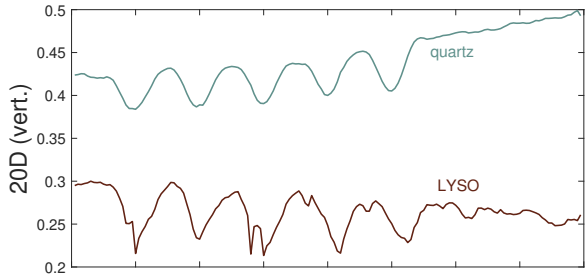

(a) 20D nails, horizontal spatial profiles

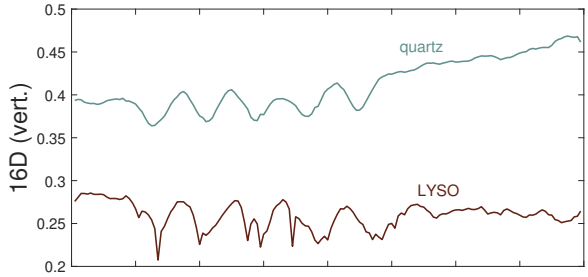

(b) 16D nails, horizontal spatial profiles

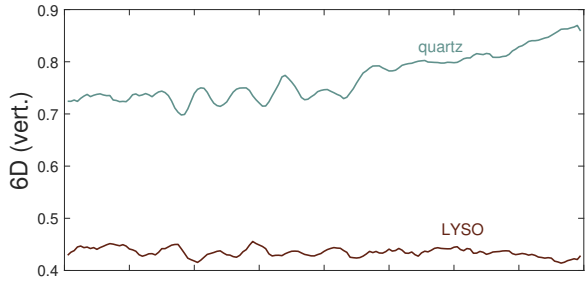

(c) 6D nails, horizontal spatial profiles

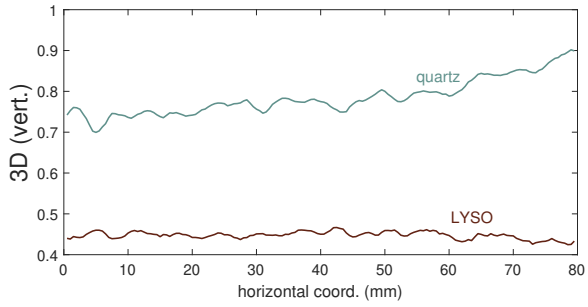

(d) 3D nails, horizontal spatial profiles

Figure 4.8: Horizontal spatial resolution image profiles, corresponding to images in Figure 4.7, in detector indices 6 (quartz) and 11 (LYSO). Effect of LYSO instability of calibration on noise is evident in those profiles.

all but one of the quartz peaks is at the baseline, whereas the noise amplification due to the steep calibration gradient for LYSO is evident and may obscure the line pairs. By the 6D profiles, the quartz still shows the line pairs, albeit with much less contrast, while the LYSO profile is almost indistinguishable from a noisy baseline measurement. The 3D profiles confirm visual analysis of the corresponding image in Figure 4.7: that the 2 mm line pairs are unrecognizable, and the limit of horizontal spatial resolution for the system is apparently close to 3 mm.

4.3 Penetration

In the ANSI penetration test, "[t]he test object is a steel arrowhead shape 30 cm long and 30 cm wide as shown in [dimensioning figure] with its thickness (x) approximately 20% of the expected measured penetration" [12]. Because the fabricated array is significantly smaller than the requisite dimensions for the described object, a scaled version was created. The scaled test object is a steel arrowhead shape 5.1 cm long and 5.1 cm wide. The contrast sensitivity/penetration tests designed closely follow the ANSI specification, though N42.46-2008 requires a steel mounting plate and blocking plates. In lieu of steel, blocking plates consisting of lead were used, and the mounting apparatus is composed of cardboard, in order to minimize transmission for "open-air" like measurements. The object is mounted to the stand with a magnet on the reverse side. Both the dimensions of the object and a visual image of its mounting are shown in Figure 4.9.

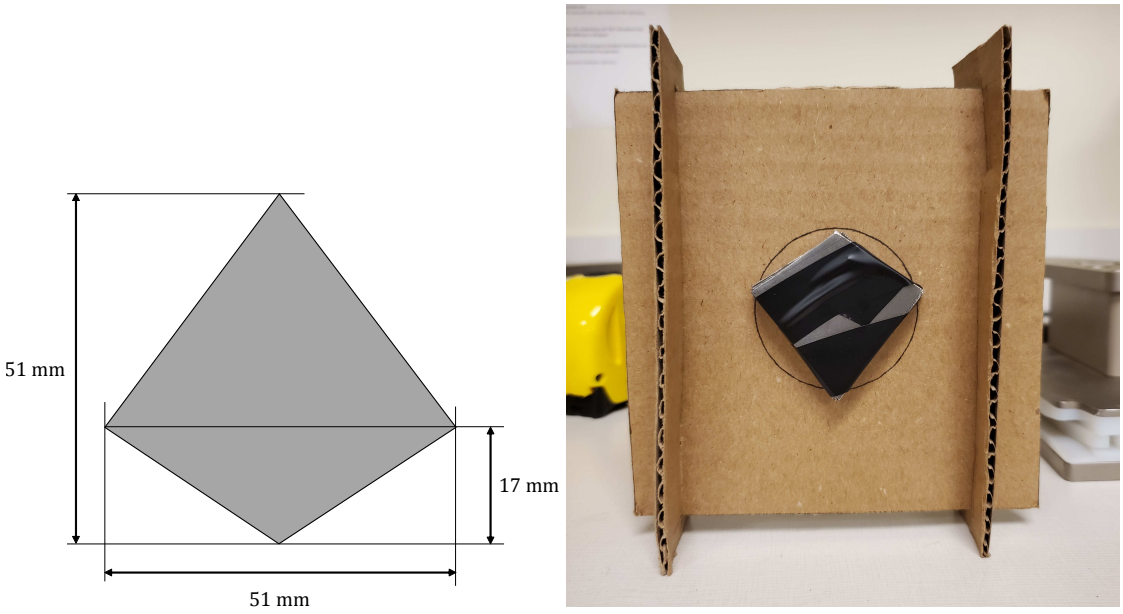

(a) Object dimensions (6.83 mm thick). (b) Object mounted to cardboard stand.

Figure 4.9: Contrast sensitivity and penetration object, a 1:6 scale representation of that used in the ANSI standard imaging test.

The arrow is composed of 22 gauge plain steel sheet metal shims held together by electrical tape. Rather than 20% of expected measured penetration as the thickness, the

object thickness is set to 20% absolute penetration – that is, object thickness t_{obj} satisfies $1 - 0.8 = e^{-\mu t_{obj}}$ at an effective beam energy of 2 MeV. The calculated value of 6.65 mm is roughly equivalent to the thickness of 9 of the 22 gauge shims, 6.83 mm, which is the thickness at which the object is used in the penetration test.

Blocking plates were composed of lead of varying thickness. As an analogue to contrast sensitivity testing through steel, approximately equivalent thicknesses of lead to 5 cm, 10 cm and 15 cm of steel were used. A list of blocking plate thicknesses is given in Table 4.3.

Table 4.3: Lead blocking plate steel-equivalent thicknesses for 2 MeV bremsstrahlung, and expected penetration through amount of lead used (not including the test object).

steel thickness	equivalent lead thickness (cm)	actual lead thickness used (cm)	expected lead penetration (I/I_0)
5	3.21	3.00	0.073
10	6.43	6.08	0.0054
15	9.64	10.16	4.0e-4

For the penetration images presented below, all rows are adjusted to have zero mean, so that striping is reduced – the striping seen here and in the previous section is almost certainly due to slight differences in experimental setup (placement of array, drift of supply voltage, temperature and humidity, and so on). This is a common image processing technique which in this case is used to facilitate ease of reading the arrow direction for the operator.

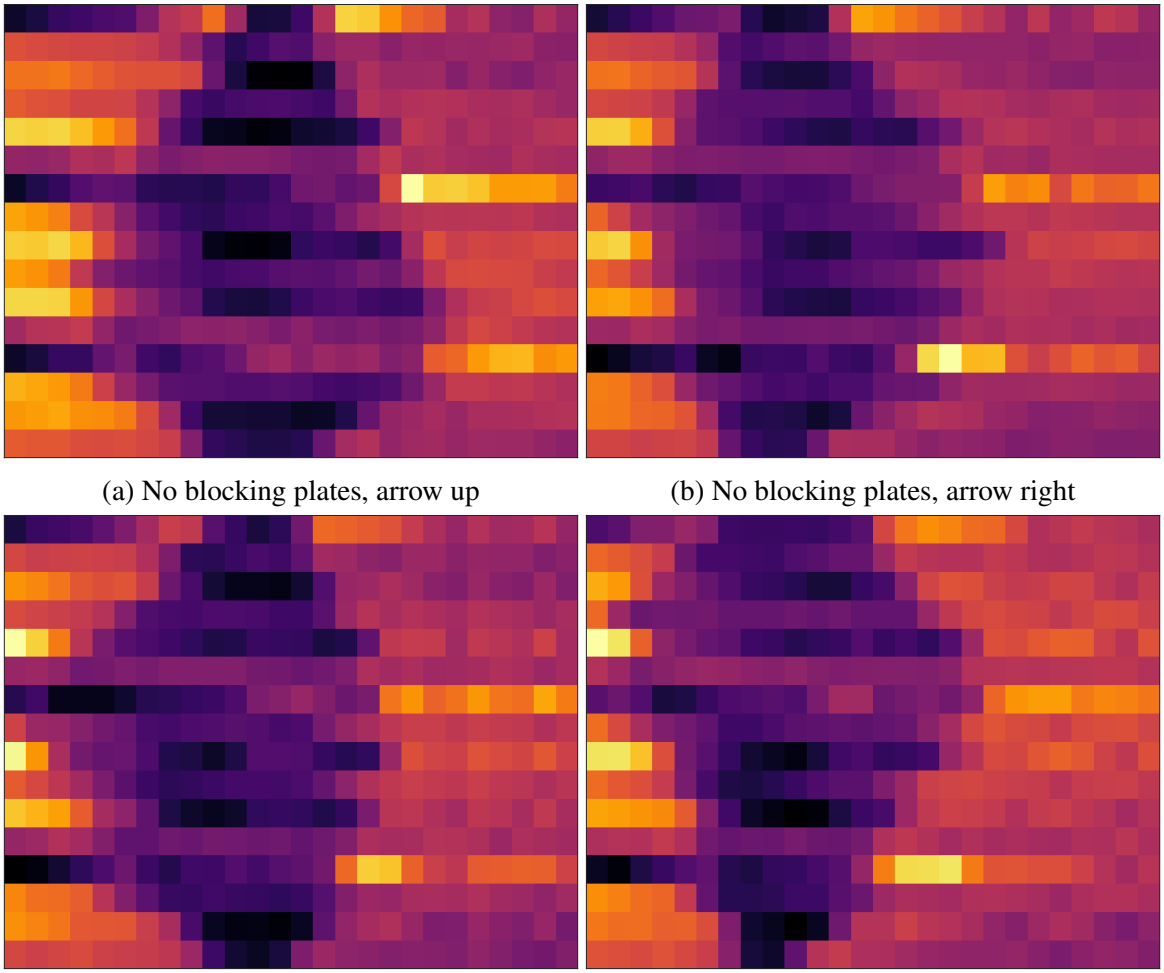

(a) No blocking plates, arrow up

(b) No blocking plates, arrow right

(c) No blocking plates, arrow left

(d) No blocking plates, arrow down

Figure 4.10: Unblocked images of the penetration/constrast sensitivity object. The object is distorted such that it is compressed in the lateral dimension, due to the pixel size of the image (2.4 mm $\times$ 3 mm).

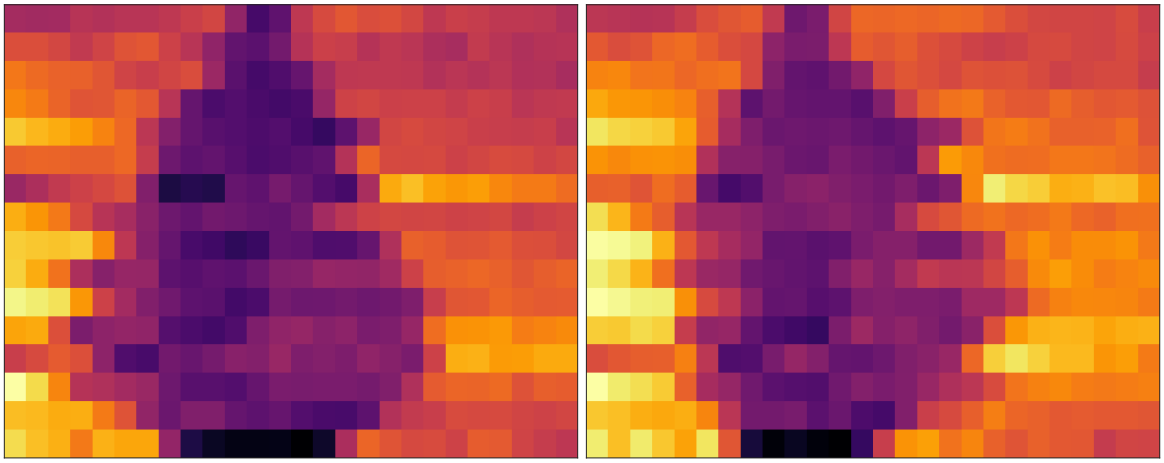

(a) 3 cm lead blocking, arrow up

(b) 3 cm lead blocking, arrow right

(c) 3 cm lead blocking, arrow left

(d) 3 cm lead blocking, arrow down

Figure 4.11: Test object blocked by 3 cm of lead. The object is distorted such that it is compressed in the lateral dimension, due to the pixel size of the image (2.4 mm $\times$ 3 mm).

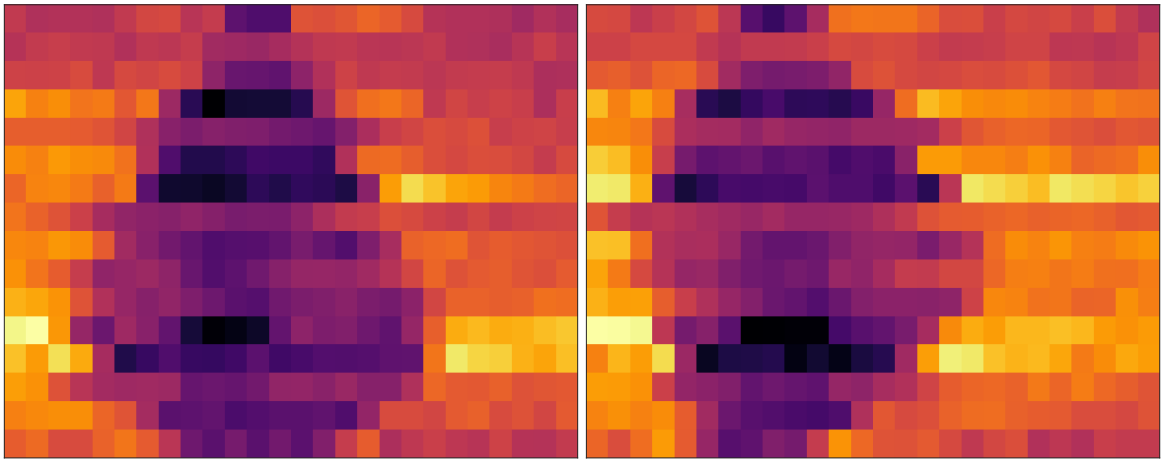

(a) 6.1 cm lead blocking, arrow up

(b) 6.1 cm lead blocking, arrow right

(c) 6.1 cm lead blocking, arrow left

(d) 6.1 cm lead blocking, arrow down

Figure 4.12: Test object blocked by 6.1 cm of lead. The object is distorted such that it is compressed in the lateral dimension, due to the pixel size of the image (2.4 mm $\times$ 3 mm).

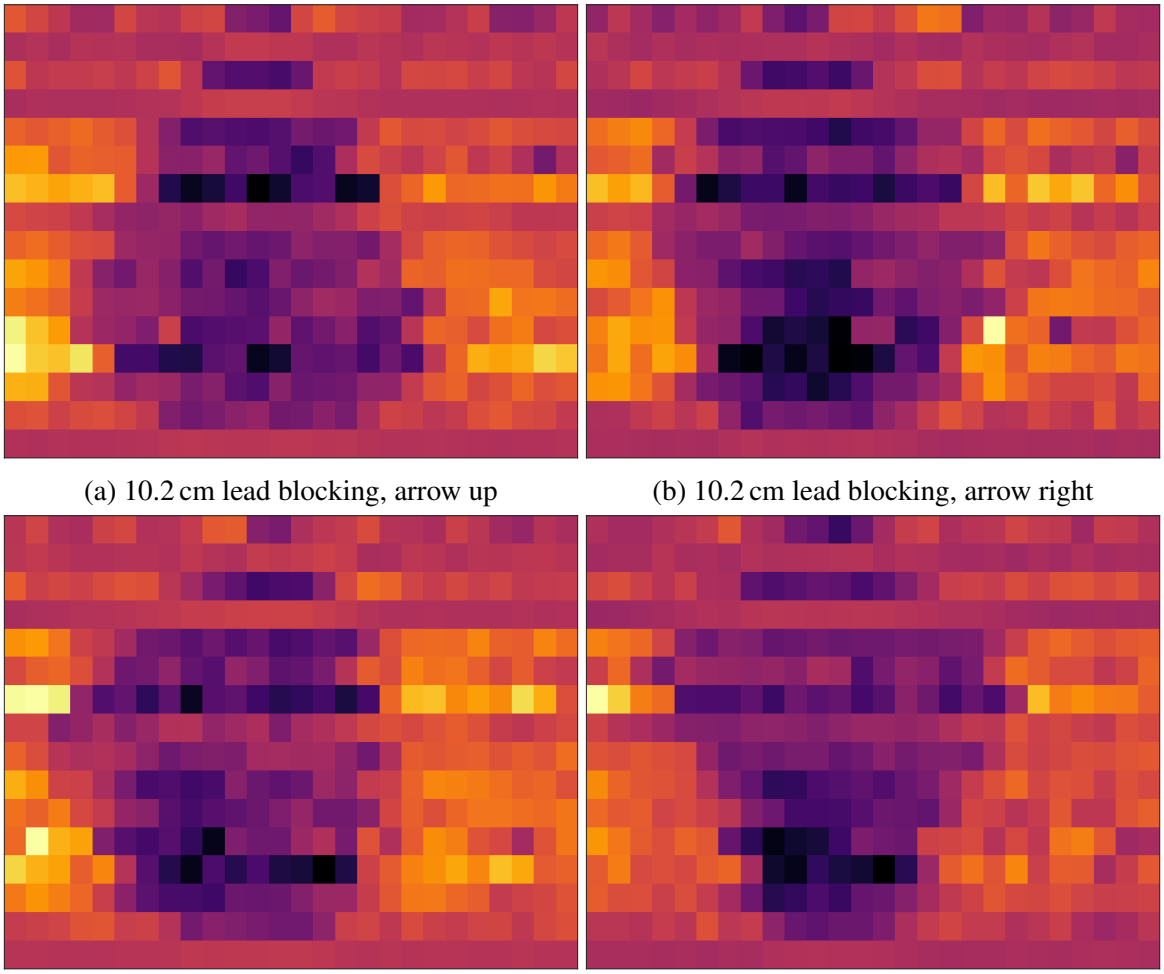

(a) 10.2 cm lead blocking, arrow up

(b) 10.2 cm lead blocking, arrow right

(c) 10.2 cm lead blocking, arrow left

(d) 10.2 cm lead blocking, arrow down

Figure 4.13: Test object blocked by 10.2 cm of lead. The object is distorted such that it is compressed in the lateral dimension, due to the pixel size of the image (2.4 mm $\times$ 3 mm).

4.4 Contrast sensitivity

In the ANSI standard imaging test, the contrast sensitivity test is designed to determine how well features (specifically, the arrow orientation) can be distinguished at fractions (10%, 50%, and 80%) of the system's measured penetration. At each thickness corresponding to a penetration fraction, the thickness of the object is successively decreased until the operator can no longer determine the orientation of the arrow. The contrast sensitivity at a given penetration percentage is given as

$$CS = \frac{t_{arrow}}{t_{plates}}, \tag{4.2}$$

with the thickness of the arrow object and blocking plates composed of the same material (steel). In this work, the arrow and blocking plates are composed of different material as outlined in section 4.3, where lead blocking thickness is given as steel-equivalent in Table 4.3.

For the contrast sensitivity test used in this work, the contrast sensitivity is evaluated in a similar quantitative manner for all penetration blocking thicknesses evaluated. Figure 4.14 and Figure 4.15 show the results of the contrast sensitivity test image reconstructions for an object 2/3 the original thickness (6.83 mm) and 1/3 the original thickness. As the test is operator-dependent, the test is *not objective*, and it is incumbent on the reader to determine the contrast sensitivity of the system, from the figures below. Contrast sensitivity percentage values for 1/3 and 2/3 thickness are given in Table 4.4, using steel-equivalent values for t_{plates}.

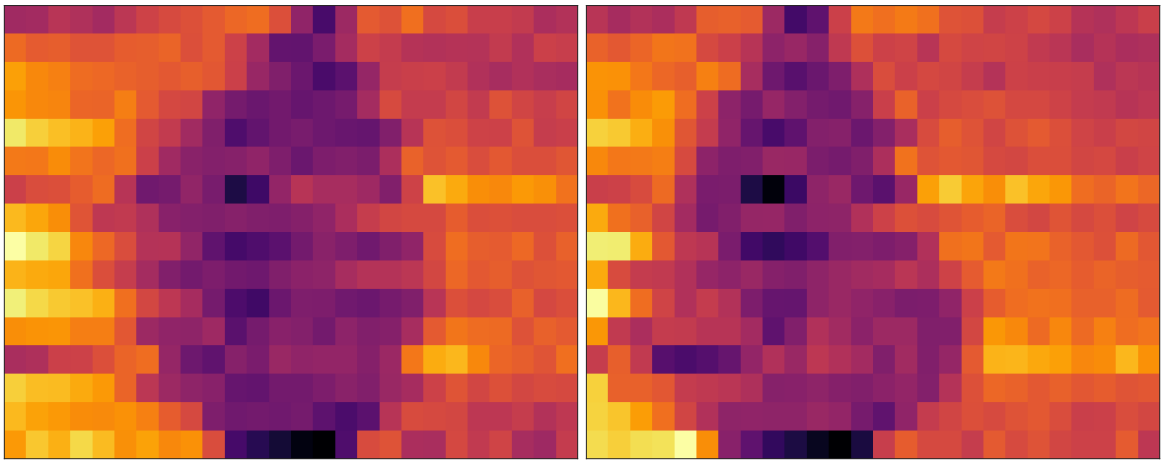

(a) 3 cm lead blocking, arrow left

(b) 3 cm lead blocking, arrow up

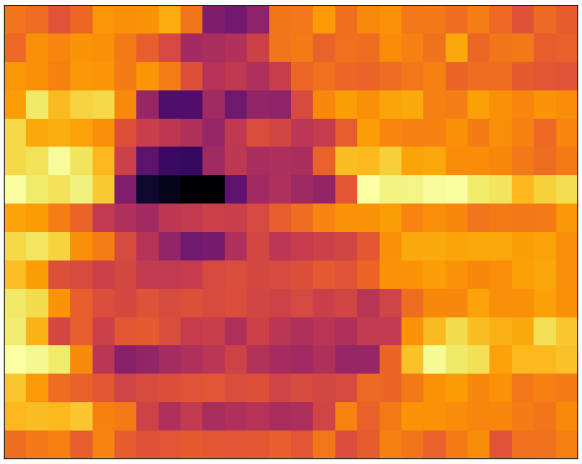

(c) 6.1 cm lead blocking, arrow up

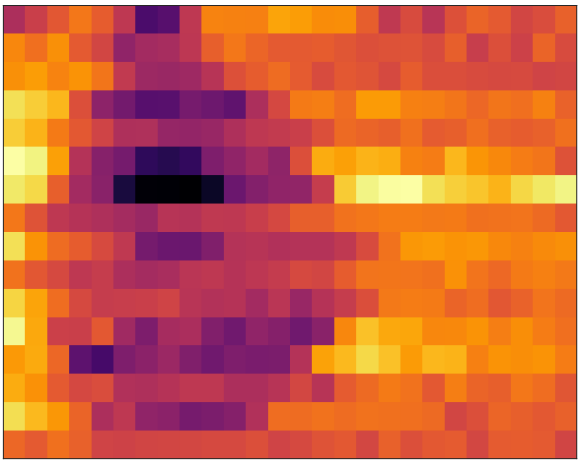

(d) 6.1 cm lead blocking, arrow right

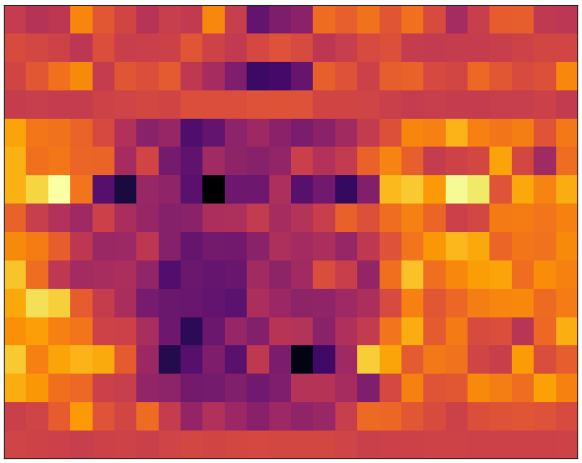

(e) 10.2 cm lead blocking, arrow left

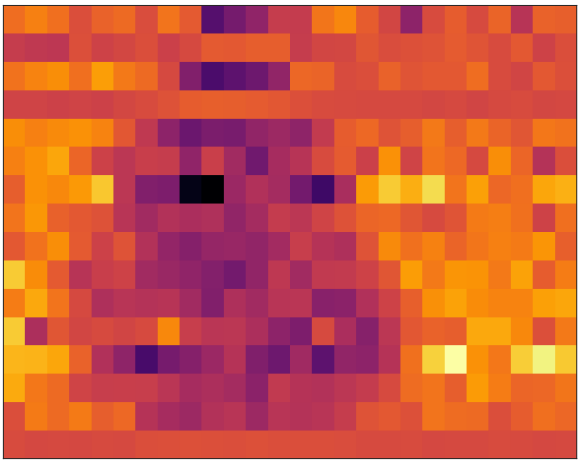

(f) 10.2 cm lead blocking, arrow up

Figure 4.14: Contrast sensitivity test at 2/3 thickness.

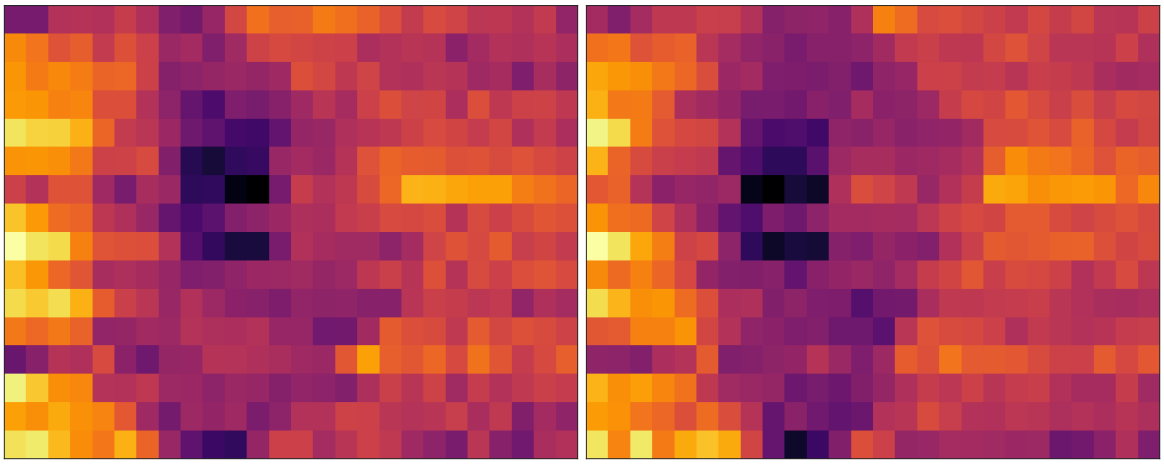

(a) 3 cm lead blocking, arrow right

(b) 3 cm lead blocking, arrow down

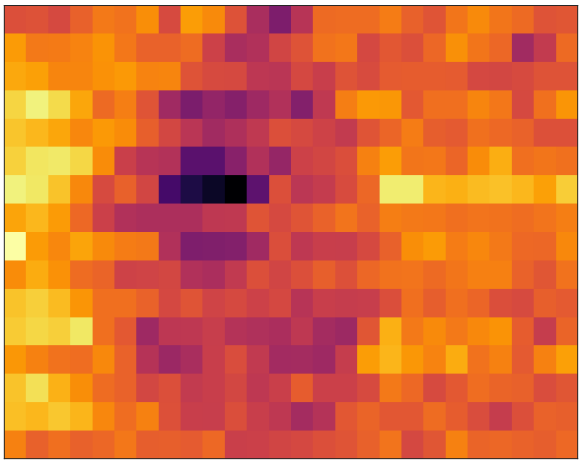

(c) 6.1 cm lead blocking, arrow left

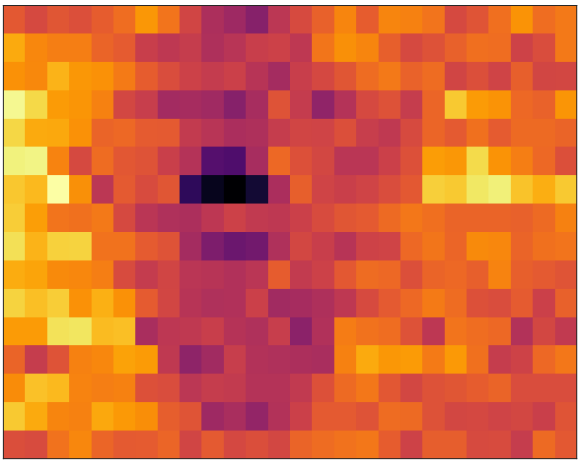

(d) 6.1 cm lead blocking, arrow down

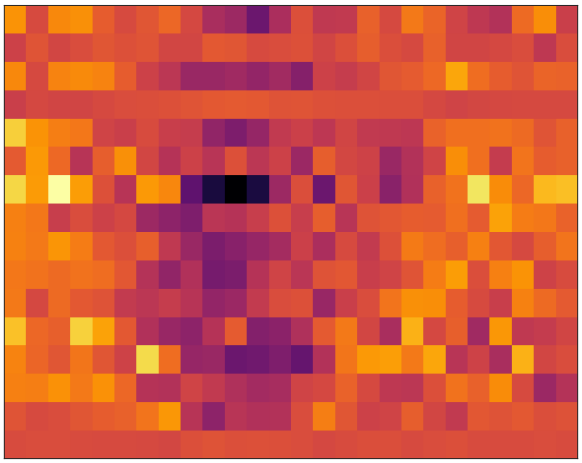

(e) 10.2 cm lead blocking, arrow down

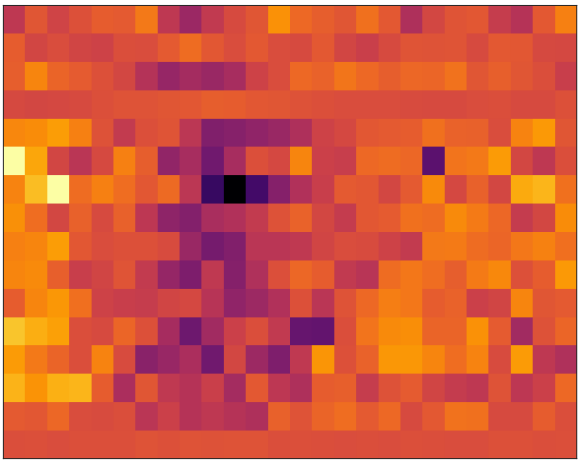

(f) 10.2 cm lead blocking, arrow right

Figure 4.15: Contrast sensitivity test at 1/3 thickness.

Table 4.4: Contrast sensitivity values for image evaluation, for use with Figure 4.14, Figure 4.15, and those in section 4.3

		blocking plate lead thickness		
		3 cm	6.1 cm	10.2 cm
object	1	13.6%	6.83%	4.55%
fractional	2/3	6.83%	3.41%	2.28%
thickness	1/3	4.55%	2.28%	1.52%

4.5 Material discrimination

The goal of material discrimination in imaging is to determine an effective atomic number, or Z_{eff}, map over the image space. In a cargo scanning sense, this allows the operator to quickly identify regions of the image where high-Z materials are present, potentially corresponding to special nuclear material.

The basis of material discriminating power is the difference in linear attenuation coefficient μ and the components which compose it: the cross-sections for photoelectric absorption, Compton scattering, and pair production. As shown in Figure 2.1a, each type of interaction dominates in a different energy regime. For a 6 MeV bremsstrahlung beam, the ratio of photons interacting via pair production to those interacting via Compton scatter will be significantly lower than for an 18 MeV beam. The variation in the cross-section components of μ is such that for a given material, its atomic number Z can be determined from the ratio of transmission of two distinct-energy gammas through the material:

$$R_M = \frac{\ln\left(T(E_H)\right)}{\ln\left(T(E_L)\right)} = \frac{\mu_H}{\mu_L}\,, \tag{4.3}$$

where $T(E)$ represents the transmission fraction at a certain energy E, from the 1D Beer-Lambert law (see Equation 3.7), and μ_H and μ_L represent the attenuation coefficients at the higher and lower of the selected energies respectively. This expression is valid provided that the two measurements are acquired in thin-beam geometry – that is, any photons interacting in the interrogated material are completely removed from the beam and have no probability of reaching the detectors. The geometry for high- and low-energy acquisitions must also include the same intervening path length x of material, such that the e^x terms in the Beer-Lambert equation are identical and their ratio is unity. R_M and Z form a bijective map (or almost-bijective) for some choices of E_H and E_L, though for lower energies R_M is nonunique (see Figure 4.16).

Material discrimination is performed for combined AmBe and cesium-137 spectra, due

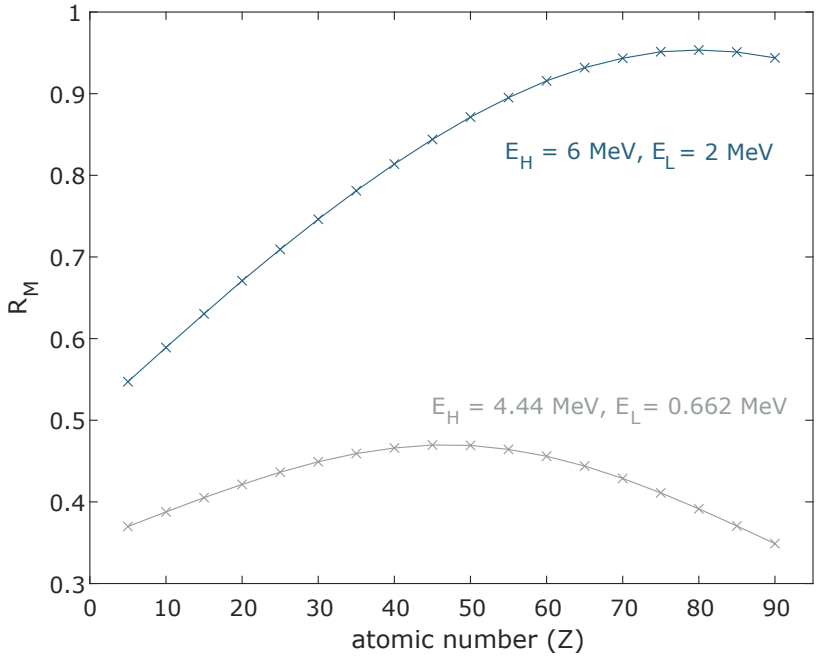

Figure 4.16: Theoretical values (from NIST) of R_M for a range of material atomic numbers, given a pair of choices for E_H and E_L. In the lower energy regime, the dependence of R_M on Z is not bijective, decreasing usefulness in an interrogation setting.

to the fact that the 6 MeV and 18 MeV bremsstrahlung beams available from the linac are polyenergetic, and although the analysis made be performed by the proxy of effective bremsstrahlung beam energy, further analysis would be necessary to determine an appropriate E_{eff} for material discrimination. Further, the gradient of the material-based calibration curve is so steep that uncertainty in transmission would be very high for the 18 MeV beam.

The material discrimination measurements were performed by placing 100 mCi AmBe and 0.1 mCi cesium-137 sources at a standoff distance of 30 cm from the detector faces, centered horizontally on the array and roughly centered vertically. Interrogated blocks (of dimensions 5.1 cm $\times$ 10.2 cm $\times$ 2.5 cm $w \times h \times l$) were placed between the sources and lightproof box containing the array, as close to the box as possible, so that the beam traversed through the 5.1 cm $\times$ 10.2 cm face of the block – because of the short distance from source to detector, path length was not necessarily 2.5 cm. However, the formula for R_M in Equation 4.3 is path length-independent.

The blocks used for material discrimination were the same as those used in imaging

calibration, namely Cu, Fe, Al, and low-density polyethylene (LDPE). Sample bare and blocked spectra are shown in Figure 4.17. The effective atomic number of polyethylene used is 2.65, as measured in this energy regime in [62].

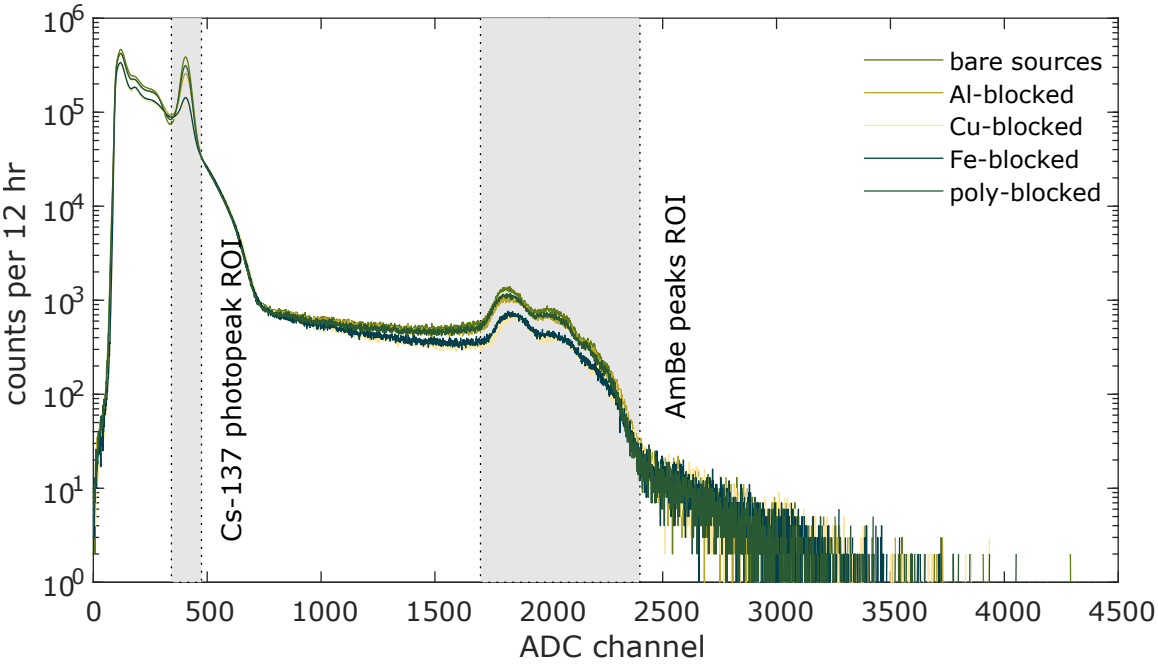

Figure 4.17: AmBe and Cs-137 spectra from a single LYSO detector, for material discrimination study. The integration regions for the cesium-137 and AmBe photo- and escape peaks are shaded.

Calculated values of R_M from all LYSO spectra are shown in Figure 4.18. The results from direct integration and division on the LYSO spectra universally overestimate the NIST-predicted values. The maximum error in the measurements is $+178.1\%$, for the LDPE, while the average error across all measurements is $+98.9\%$.

The poor agreement of the LYSO data to the expected values may be due to one or several factors. It is not due to background radiation - though in the approach used above the spectra are not background-corrected, the relative background is very low in relation to any superposed counts (specifically from the cesium gamma line). Indeed, background subtraction would actually worsen the agreement by decreasing the denominator in Equation 4.3. Buildup due to scatter is the most likely dominant factor, especially in causing the breakdown of the thin-beam approximation. Because the source-to-object and source-to-

detector distance is small, the solid angle subtended by a scattering particle is more likely to intersect a detector than for a large standoff, exacerbated by the fact that Compton scatter is the dominant mode of interaction for both 0.662 MeV and 4.44 MeV gamma rays for all interrogated materials. A small standoff was used to minimize the irradiation time required to achieve low count per bin uncertainty, but the distance could be increased to approximate a thin beam.

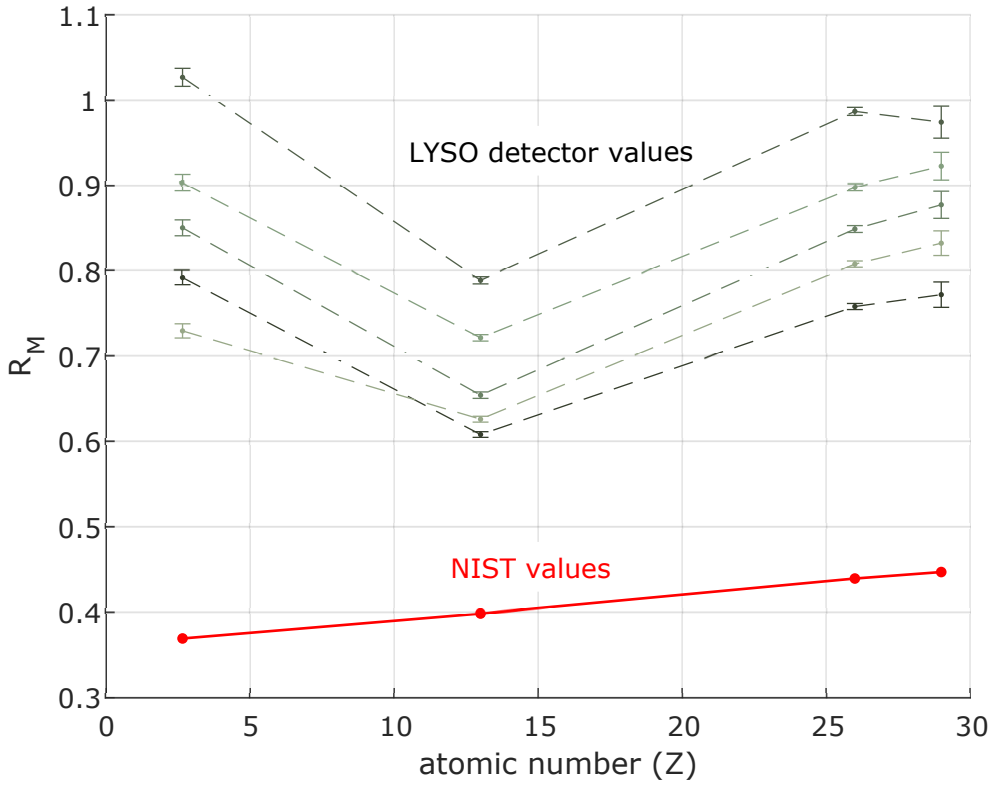

Figure 4.18: Calculated values of R_M for each of the LYSO detectors for the material blocks studied.

CHAPTER 5

CONCLUSIONS

It has been shown here and in previous work that Cerenkov detectors are well-suited to imaging applications, particularly under high-flux irradiation, such as is available from a linear accelerator. As the array evaluated here is intended to serve as a prototype and test model for a much larger imaging system capable of imaging entire cargoes, a cost estimate for the full-scale system of 360 channels (at a scale of 1.8 m) is included here.

5.1 System cost

LYSO, as a scintillator, is expensive, due to the growth and handling processes needed to manufacture it. The cost of 120 units (for a total array height of 180 cm) of the dimensions used here is about $31 200, or $260 per unit. Quartz rods, on the other hand, can be obtained for about $2.40 per foot, or about $0.40 per detector element for raw material. Using the 2:1 quartz:LYSO ratio, all of the quartz for the large-scale array can be obtained for under $100.

Even allowing a generous processing margin, the difference in price for these detector elements is dramatic, particularly considering the pulsed nature of the source in use – as the amplitude of individual detected events is determined by all photons produced during the pulse duration, the instability of calibration amplifies noise to the detriment of image readability, as shown previously. For the quartz radiators, the calibration curve is much nearer to linear, and with a lower gradient. Further, the near-instantaneous light emission from Cerenkov events allows easy thresholding of events on the basis of time between subsequent events, which would not be possible in LYSO due to the Poisson nature of excited state decay.

Pulse processing costs depend on the form factor of the devices used. The CAEN DT5730 digitizers used in this work cost about $16 500 per unit, or about $2050 per channel for pulse processing, and are of a form factor designed to be placed on a work desk, thus contain the necessary power supply and cooling for each unit. These units are daisy-chainable through an optical link protocol. These units are in the same product family as CAEN's V1730, which is a VME crate-mountable alternative near the $6000 price point, or $750 per channel.

As SiPMs are entering mainstream use, dedicated readout systems for use with them are also available. CAEN in particular offers the DT5702, an application-specific integrated circuit (ASIC)-based frontend readout board with 12-bit ADC digitization which handles up to 32 channel inputs simultaneously, for a cost of about $3250, or just over $100 per channel. The DT5702 is also daisy-chainable without the need for a VME crate.

The listed unit price from Digikey for the J-Series 60035 SiPM as of the time of this writing is $108.22. However, a quote obtained for full-service (turnkey) board assembly of 45 PCB units (including all 360 detector channels) had an aggregate cost of $33 552, or $93.20 per channel for all backend electronic components, including PCB assembly but not including cabling connecting the array to associated frontend readout systems.

A summary of cost estimates is shown in Table 5.1. The readout system dominates the cost, provided that conventional flash ADCs are used. Using the newer ASIC-based device, the system component cost is roughly one-third due to PCB components (which itself is dominated by SiPM cost), one-third due to LYSO crystals, and one-third due to frontend readout, while the quartz Cerenkov radiators represent less than 0.1% of the system cost. The caveat to implementing a device like the DT5702 is that the software interfacing tools are not as well-developed as those for more mature digitizers.

Table 5.1: Cost estimates for full-scale system

component	per-channel cost (USD)	number of channels	total component cost (USD)	total system cost (USD)
LYSO crystals	260	120	31200	
quartz radiators	0.40	240	96	
PCBs	93.20	360	33552	
DT5730 (desktop)	2050	360	738000	802848
DT1730 (VME)	750	360	270225	335073
DT5702 (ASIC)	102	360	36720	101568

5.2 Future work

The most immediate concern for future work on this imaging system, and which would be a simple way to improve image quality, would be to resolve the issue of non-synchronicity between acquisition systems. This can be accomplished via simultaneous development of software and a triggering schema for data collection. As it stands, three separate software interfaces are required to be started by the operator: Kinesis (the Thorlabs motor controller software), the linear accelerator console (a proprietary Varian system, but which does provide system logging), and CoMPASS (which already provides data in list mode, and may be triggered externally via the digitizer). This would enable collection of time-dependent background data and permit understanding of the degradation of linac output described previously. Images can then be corrected on a pixelwise basis, rather than by rows, and vertical spatial resolution may approach the limit of detection.

Material discrimination performance can also probably be improved by a wide margin. The results reported here do not include material-discriminating imaging using the linear accelerator source – though both 6 MeV and 18 MeV sources are available, a wider range of materials will be necessary in order to properly formulate the calibration datasets which would enable Z_{eff} imaging.

Cost reduction is possible and would be expedited by development of an integrated software for the DT5702 readout board. Currently, the only software written for this device is a ROOT-based GUI, though CAEN does provide with it library commands for user program development.

The pixel weighting schema should also be updated, both to include intertime thresholding data and to remove the need for the matrix resampling least-squares approach to vertical debloom correction. The former can be done for Cerenkov detector channels, but ostensibly not for LYSO channels, which have Poisson-distributed events in both the upper and lower bands. The spatial pixel weighting will require a sophisticated (but tedious) planar geometric approach, wherein the entire pixel image (rather than individual rows) may be represented parametrically. The spatial coordinates of the detector at each time tag may then be used to determine overlaps for linear count weighting over the entire image – however, this approach is likely to cost many more CPU cycles, and may decrease performance for negligible improvement to image quality.

5.3 Recommendations and concluding remarks

This work has shown that a combination Cerenkov-LYSO imaging array is well-suited to active interrogation applications where fine spatial resolution is required. The horizontal spatial resolution was shown to be at most 4 mm, while the vertical spatial resolution will require additional updates to the system, as described above. The contrast sensitivity of the system is on the order of a few percent, even when the test object is shielded by 15 cm steel-equivalent blocking plates. Further, the system's sensitivity to sinusoid wire impulses is at least enough for 12 AWG detection.

It has also been shown that Cerenkov detectors have at least one unique advantage over traditional scintillators in pulsed-source irradiation: temporal event separation is much better in a Cerenkov radiator. Using an ADC-based thresholding approach, images may be readily reconstructed from either detector type – however, due to the way that SiPMs

pulses are generated, the calibration to realistic object profiles is much more stable for quartz than for LYSO. A combination of the two thresholding schema, and further analysis on waveform data, would improve these results further.

Cerenkov radiators should be considered by the detection community at large as a viable alternative to scintillators when the application allows for it. In cargo scanning, Cerenkov detectors may find a particular niche, as the United States Congress has mandated a 100% interrogation rate for cargo entering the country, and throughput is of utmost concern. The number of cargo scanners which could be deployed can be increased if the cost is fractionated, which is possible through the use of the unconventional photoconverter in quartz as well as decreasing costs of digitization.

REFERENCES

- Those sources with URLs which are followed by an "Archived" date have snapshots of the page on that date available at https://web.archive.org.
- Digital object identifier (DOI) names of sources, where available, are resolvable at https://doi.org/, and are hyperlinked there in the PDF version of this document.

---

[1] *World container fleet overview*, http://www.csiu.co/resources-and-links/world-container-fleet, Archived: 2015-07-18.

[2] *About the industry: Trade statistics*, http://www.worldshipping.org/about-the-industry/global-trade/trade-statistics, Archived: 2019-10-21.

[3] 110th Congress, *Implementing Recommendations of the 9/11 Commission Act of 2007*, H.R.1, Thompson, Bennie G., Sponsor. https://www.congress.gov/110/plaws/publ53/PLAW-110publ53.pdf, Aug. 3, 2007.

[4] *Container shipping*, http://www.damovers.com/container-shipping/, Archived: 2008-03-27.

[5] *About the industry: Top 50 world container ports*, http://www.worldshipping.org/about-the-industry/global-trade/top-50-world-container-ports/, Archived: 2019-11-08.

[6] R. C. Lanza, R. Accorsi, and F. Gasparini, *Coded aperture imaging*, US Patent 6,737,652, May 2004.

[7] J. Armitage, D. Bryman, T. Cousins, G. Gallant, A. Jason, G. Jonkmans, S. Noël, G. Oakham, T. J. Stocki, and D. Waller, "Cosmic ray inspection and passive tomography for snm detection," in *AIP Conference Proceedings*, American Institute of Physics, vol. 1194, 2009, pp. 24–35.

[8] *Scanning and imaging shipping containers overseas: Costs and alternatives*, https://www.cbo.gov/publication/51478, Archived: 2019-10-13.

[9] P. B. Rose and A. S. Erickson, "Cherenkov detectors for spatial imaging applications using discrete-energy photons," *Journal of Applied Physics*, vol. 120, no. 6, p. 064 903, 2016, doi:10.1063/1.4960778.

[10] P. Rose and A. Erickson, "Calibration of Cherenkov detectors for monoenergetic photon imaging in active interrogation applications," *Nuclear Instruments and Methods in Physics Research Section A: Accelerators, Spectrometers, Detectors and Associated Equipment*, vol. 799, pp. 99–104, 2015, doi:10.1016/j.nima.2015.07.065.

[11] J. Harms, "Modeling and characterization of a monoenergetic gamma-ray imaging system for active interrogation applications," PhD thesis, Georgia Institute of Technology, 2018.

[12] "American national standard for determination of the imaging performance of x-ray and gamma-ray systems for cargo and vehicle security screening," *ANSI N42.46-2008*, pp. 1–35, Aug. 2008, doi:10.1109/ANSI.2008.4606807.

[13] G. Knoll, *Radiation Detection and Measurement*. Wiley, 2010, ISBN: 978-0-470-13148-0.

[14] *NaI(Tl) and Polyscin® NaI(Tl) sodium iodide scintillation material*, https://www.crystals.saint-gobain.com/sites/imdf.crystals.com/files/documents/sodium-iodide-material-data-sheet_0.pdf, Archived: 2020-02-08.

[15] *LYSO scintillation material*, https://www.crystals.saint-gobain.com/sites/imdf.crystals.com/files/documents/lyso-material-data-sheet.pdf, Archived: 2019-11-14.

[16] *$CdWO_4$ cadmium tungstate scintillation material*, https://www.crystals.saint-gobain.com/sites/imdf.crystals.com/files/documents/cadmium-tungstate-material-data-sheet.pdf, Archived: 2019-10-21.

[17] *BGO bismuth germanate scintillation material*, https://www.crystals.saint-gobain.com/sites/imdf.crystals.com/files/documents/bgo-material-data-sheet.pdf, Archived: 2020-02-10.

[18] R. Mao, L. Zhang, and R.-Y. Zhu, "Optical and scintillation properties of inorganic scintillators in high energy physics," *IEEE Transactions on Nuclear Science*, vol. 55, no. 4, pp. 2425–2431, 2008, doi:10.1109/TNS.2008.2000776.

[19] *GSO / GSO(Ce) gadolinium orthosilicate*, https://www.advatech-uk.co.uk/gso_ce.html, Archived: 2020-03-26.

[20] K. Takagi and T. Fukazawa, "Cerium-activated Gd_2Sio_5 single crystal scintillator," *Applied Physics Letters*, vol. 42, no. 1, pp. 43–45, 1983, doi:10.1063/1.93760.

[21] M. Moszyński, M. Kapusta, D. Wolski, W. Klamra, and B. Cederwall, "Properties of the YAP:Ce scintillator," *Nuclear Inst. and Methods in Physics Research, A*, vol. 404, no. 1, pp. 157–165, 1998, doi:10.1016/S0168-9002(97)01115-7.

[22] *YAP(Ce) - yttrium aluminium perovskite*, https://www.advatech-uk.co.uk/yap_ce.html, Archived: 2020-03-26.

[23] *Lanthanum bromide and enhanced lanthanum bromide*, https://www.crystals.saint-gobain.com/sites/imdf.crystals.com/files/documents/lanthanum-material-data-sheet.pdf, Archived: 2020-02-15.

[24] J. Zhao, H. Chen, Q. Han, Z. Huang, L. Chen, Y. Li, B. Meng, H. Sun, J. Luo, Y. Wang, *et al.*, *Container inspection system using cobalt-60 gamma-ray source and cesium iodide or cadmium tungstate array detector*, US Patent 7,082,186, Jul. 2006.

[25] J. Stevenson, T. Gozani, M. Elsalim, C. Condron, and C. Brown, "Linac based photofission inspection system employing novel detection concepts," *Nuclear Instruments and Methods in Physics Research Section A: Accelerators, Spectrometers, Detectors and Associated Equipment*, vol. 652, no. 1, pp. 124–128, 2011, doi:10.1016/j.nima.2010.08.047.

[26] N. Carron, *An Introduction to the Passage of Energetic Particles through Matter*. CRC Press, 2006, ISBN: 978-1-420-01237-8.

[27] W. S. Rodney and R. J. Spindler, "Index of refraction of fused quartz glass for ultraviolet, visible, and infrared wavelengths," *JOSA*, vol. 44, no. 9, pp. 677–679, 1954, doi:10.1364/JOSA.44.000677.

[28] M. Berger, J. Hubbell, S. Seltzer, J. Chang, J. Coursey, R. Sukumar, D. Zucker, and K. Olsen, "XCOM: Photon cross section database (version 1.5)," *National Institute of Standards and Technology, Gaithersburg, MD.*, 2010, Available: http://physics.nist.gov/xcom [2020, March 13].

[29] I. H. Malitson, "Interspecimen comparison of the refractive index of fused silica," *J. Opt. Soc. Am.*, vol. 55, no. 10, pp. 1205–1209, 1965, doi:10.1364/JOSA.55.001205.

[30] C. Tan, "Determination of refractive index of silica glass for infrared wavelengths by IR spectroscopy," *Journal of Non-Crystalline Solids*, vol. 223, no. 1, pp. 158–163, 1998, doi:10.1016/S0022-3093(97)00438-9.

[31] M. Berger, J. Hubbell, S. Seltzer, and J. Chang, "ESTAR, PSTAR, and ASTAR: Computer programs for calculating stopping-power and range tables for electrons, protons, and helium ions (version 1.2.3)," *National Institute of Standards and Technology, Gaithersburg, MD.*, 2005, Available: http://physics.nist.gov/Star [2020, March 13].

[32] *RX-22P optical silicone coupling compound*, https://www.rexon.com/Scint[1].Catalog.pdf, Archived: 2016-09-09.

[33] S. Cova, M. Ghioni, A. Lacaita, C. Samori, and F. Zappa, "Avalanche photodiodes and quenching circuits for single-photon detection," *Appl. Opt.*, vol. 35, no. 12, pp. 1956–1976, Apr. 1996, doi:10.1364/AO.35.001956.

[34] D. Renker, "Geiger-mode avalanche photodiodes, history, properties and problems," *Nuclear Instruments and Methods in Physics Research Section A: Accelerators, Spectrometers, Detectors and Associated Equipment*, vol. 567, no. 1, pp. 48–56, 2006, doi:10.1016/j.nima.2006.05.060.

[35] S. Espana, G. Tapias, L. M. Fraile, J. L. Herraiz, E. Vicente, J. Udias, M. Desco, and J. J. Vaquero, "Performance evaluation of SiPM detectors for PET imaging in the presence of magnetic fields," in *2008 IEEE Nuclear Science Symposium Conference Record*, doi:10.1109/NSSMIC.2008.4774097, Oct. 2008, pp. 3591–3595.

[36] *J-Series SiPM sensors*, https://www.onsemi.com/pub/Collateral/MICROJ-SERIES-D.PDF, Archived: 2019-03-02.

[37] *C-Series SiPM sensors*, https://www.onsemi.com/pub/Collateral/MICROC-SERIES-D.PDF, Archived: 2019-03-02.

[38] *Product Data Sheet: Pm1125-wb-c0*, https://www.ketek.net/wp-content/uploads/KETEK-PM1125-WB-C0-Datasheet.pdf, Archived: 2020-04-23.

[39] *Product Data Sheet: Pm3315-wb-c0*, https://www.ketek.net/wp-content/uploads/KETEK-PM3315-WB-C0-Datasheet.pdf, Archived: 2020-04-23.

[40] *MPPC for detection of Cherenkov light: S14520 series*, Private communication, Archived: 2020-04-23.

[41] *Low breakdown voltage, wide dynamic range type MPPC with small pixels*, https://www.hamamatsu.com/resources/pdf/ssd/s14160-1310ps_etc_kapd1070e.pdf, Archived: 2020-04-23.

[42] *S13360 series: MPPCs for precision measurement*, https://www.hamamatsu.com/resources/pdf/ssd/s13360_series_kapd1052e.pdf, Archived: 2020-02-08.

[43] *S14420 series: Visible/near infrared MPPC*, https://www.hamamatsu.com/resources/pdf/ssd/s14420_series_kapd1061e.pdf, Archived: 2020-04-23.

[44] *Red, Green, Blue (RGB) SiPMs*, https://www.first-sensor.com/cms/upload/datasheets/SiPM-RGB_5000080-5000083.pdf, Archived: 2020-04-23.

[45] *Near Utraviolet (NUV) SiPMs*, https://www.first-sensor.com/cms/upload/datasheets/SiPM-NUV_5000076-5000079.pdf, Archived: 2020-04-23.

[46] J. Harms, P. B. Rose, and A. Erickson, "Characterization of gamma-ray cross talk in Cherenkov-based detectors for active interrogation imaging applications," *IEEE Sensors Journal*, vol. 17, no. 20, pp. 6707–6715, Oct. 2017, doi:10.1109/JSEN.2017.2745711.

[47] *Dt5730 8 channel 14 bit 500 MS/s digitizer*, https://www.caen.it/products/dt5730/, Archive: 2020-06-23.

[48] Nuclear Data Sheets 107, 791 (2006).

[49] F. M. Khan, "Clinical radiation generators," in *The Physics of Radiation Therapy*. Lippincott Williams & Wilkins, 2003, ch. 4, pp. 38–58.

[50] "X-ray production and quality," in *Introduction to Radiological Physics and Radiation Dosimetry*. John Wiley & Sons, Ltd, 2007, ch. 9, pp. 203–230, doi:10.1002/9783527617135.ch9 ISBN: 9783527617135. eprint: https://onlinelibrary.wiley.com/doi/pdf/10.1002/9783527617135.ch9.

[51] L. J. Maloney, "Design of an x-ray ct system with implementation of sparse-data reconstruction," Master's thesis, Georgia Institute of Technology, 2017.

[52] R. L. Siddon, "Fast calculation of the exact radiological path for a three-dimensional ct array," *Medical Physics*, vol. 12, no. 2, pp. 252–255, 1985, doi:10.1118/1.595715. eprint: https://aapm.onlinelibrary.wiley.com/doi/pdf/10.1118/1.595715.

[53] F. Acerbi and S. Gundacker, "Understanding and simulating SiPMs," *Nuclear Instruments and Methods in Physics Research Section A: Accelerators, Spectrometers, Detectors and Associated Equipment*, vol. 926, pp. 16–35, 2019, doi:10.1016/j.nima.2018.11.118.

[54] C. Piemonte, A. Ferri, A. Gola, A. Picciotto, T. Pro, N. Serra, A. Tarolli, and N. Zorzi, "Development of an automatic procedure for the characterization of silicon photomultipliers," in *2012 IEEE Nuclear Science Symposium and Medical Imaging Conference Record (NSS/MIC)*, IEEE, 2012, pp. 428–432, ISBN: 9781467320283.

[55] A. J. Shepard, C. K. Matrosic, J. L. Radtke, S. A. Jupitz, W. S. Culberson, and B. P. Bednarz, "Technical Note: Characterization of clinical linear accelerator triggering latency for motion management system development," *Medical Physics*, vol. 45, no. 11, pp. 4816–4821, 2018, doi:10.1002/mp.13191. eprint: https://aapm.onlinelibrary.wiley.com/doi/pdf/10.1002/mp.13191.

[56] W. Feller, *An Introduction to Probability Theory and Its Applications*. Wiley, Jan. 1968, vol. 1, ISBN: 0471257087.

[57] V. Regazzoni, F. Acerbi, G. Cozzi, A. Ferri, C. Fiorini, G. Paternoster, C. Piemonte, D. Rucatti, G. Zappalà, N. Zorzi, and A. Gola, "Characterization of high density

SiPM non-linearity and energy resolution for prompt gamma imaging applications," *Journal of Instrumentation*, vol. 12, no. 07, P07001–P07001, Jul. 2017, doi:10.1088/1748-0221/12/07/p07001.

[58] V. Andreev, V. Balagura, B. Bobchenko, P. Buzhan, J. Cvach, M. Danilov, E. Devitsin, V. Dodonov, B. Dolgoshein, G. Eigen, L. Filatov, E. Garutti, M. Groll, R.-D. Heuer, A. Ilyin, M. Janata, I. Kacl, V. Kantserov, V. Kaplin, A. Karakash, S. Klemin, V. Korbel, V. Kozlov, H. Meyer, R. Mizuk, V. Morgunov, E. Novikov, S. Němeček, R. Pöschl, I. Polák, E. Popova, A. Raspereza, S. Reiche, V. Rusinov, F. Sefkow, P. Smirnov, S. Smirnov, Y. Soloviev, E. Tarkovsky, A. Terkulov, V. Tikhomirov, Š. Valkár, J. Weichert, and J. Zálešák, "A high-granularity scintillator calorimeter readout with silicon photomultipliers," *Nuclear Instruments and Methods in Physics Research Section A: Accelerators, Spectrometers, Detectors and Associated Equipment*, vol. 540, no. 2, pp. 368–380, 2005, doi:10.1016/j.nima.2004.12.002.

[59] D. Renker and E. Lorenz, "Advances in solid state photon detectors," *Journal of Instrumentation*, vol. 4, no. 04, P04004–P04004, Apr. 2009, doi:10.1088/1748-0221/4/04/P04004.

[60] L. Gruber, S. Brunner, J. Marton, and K. Suzuki, "Over saturation behavior of sipms at high photon exposure," *Nuclear Instruments and Methods in Physics Research Section A: Accelerators, Spectrometers, Detectors and Associated Equipment*, vol. 737, pp. 11–18, 2014, doi:10.1016/j.nima.2013.11.013.

[61] G. H. Golub and C. F. Van Loan, *Matrix Computations*, Third. The Johns Hopkins University Press, 1996.

[62] N. Kucuk, M. Cakir, and N. A. Isitman, "Mass attenuation coefficients, effective atomic numbers and effective electron densities for some polymers," *Radiation Protection Dosimetry*, vol. 153, no. 1, pp. 127–134, May 2012, doi:10.1093/rpd/ncs091.